Observationally Constrained Metal Signatures of Galaxy Evolution in the Stars and Gas of Cosmological Simulations

Lauren N. Corlies

Submitted in partial fulfillment of the
requirements for the degree
of Doctor of Philosophy
in the Graduate School of Arts and Sciences

COLUMBIA UNIVERSITY

2016

ABSTRACT

Observationally Constrained Metal Signatures of Galaxy Evolution in the Stars and Gas of Cosmological Simulations

Lauren Corlies

The halos of galaxies - consisting of gas, stars, and satellite galaxies - are formed and shaped by the most fundamental processes: hierarchical merging and the flow of gas into and out of galaxies. While these processes are hard to disentangle, metals are tied to the gas that fuels star formation and entrained in the wind that the deaths of these stars generate. As such, they can act as important indicators of the star formation, the chemical enrichment, and the outflow histories of galaxies. Thus, this thesis aims to take advantage of such metal signatures in the stars and gas to place observational constraints on current theories of galaxy evolution as implemented in cosmological simulations.

The first two chapters consider the metallicities of stars in the stellar halo of the Milky Way and its surviving satellite dwarf galaxies. Chapter 2 pairs an N-body simulation with a semi-analytic model for supernova-driven winds to examine the early environment of a Milky Way-like galaxy. At $z = 10$, progenitors of surviving $z = 0$ satellite galaxies are found to sit preferentially on the outskirts of progenitor halos of the eventual main halo. The consequence of these positions is that main halo progenitors are found to more effectively cross-pollute each other than satellite progenitors. Thus, inhomogeneous cross-pollution as a result of different high-z spatial locations of different progenitors can help to explain observed differences in abundance patterns measured today. Chapter 3 expands this work into the

analysis of a cosmological, hydrodynamical simulation of dwarf galaxies in the early universe. We find that simple assumptions for modeling the extent of supernova-driven winds used in Chapter 2 agree well with the simulation whereas the presence of inhomogeneous mixing in the simulation has a large effect on the stellar metallicities. Furthermore, the star-forming halos show both bursty and continuous SFHs, two scenarios proposed by stellar metallicity data. However, the metallicity distribution functions of the simulated halos are both too metal rich and too peaked when compared to the data. This comparison reveals that a complex SFH and a broad metallicity distribution can develop rapidly in the early Universe.

The third chapter moves to the present day with a consideration of the circumgalactic medium (CGM) around nearby Milky Way-like galaxies. We compare a cosmological simulation of a Milky Way-like galaxy to recent absorption line data and find that a reduced extragalactic ultraviolet background brings the column density predictions into better agreement with the data. Similarly, when the observationally derived physical properties of the gas are compared to the simulation, we find that the simulation gas is always at temperatures approximately 0.5 dex higher. Thus, similar column densities can be produced from fundamentally different gas. Metal-line emission is then considered as a complementary approach to studying the CGM. From the simulations, we find that the brightest emission is less sensitive to the extragalactic background and that it closely follows the fundamental filamentary structure of the halo. This becomes increasingly true as the galaxy evolves from $z = 1$ to $z = 0$ and the majority of the gas transitions to a hotter, more diffuse phase. Finally, resolution is a limiting factor for the conclusions we can draw from emission observations but with moderate resolution and reasonable detection limits, upcoming instrumentation should place constraints on the physical properties of the CGM.

Future work advancing the techniques in this thesis remain promising for putting new observational constraints on our theories of galaxy evolution.

Contents

List of Figures

List of Tables

(This page left intentionally blank.)

Acknowledgements

I would like to take a moment to stop and realize that while the thesis is a hugely personal endeavor, I could not have been successful without the support of many wonderful people.

First and foremost, I would like to thank my thesis advisors, David Schiminovich and Kathryn Johnston, whose guidance has made me the researcher I am today. David, your patience and calmness have grounded me throughout this entire process. I always looked forward to our meetings knowing that you would guide me towards interesting questions and over the years you taught me how to find them myself. And from now on, whenever i write something, I'll hear your voice in my head asking me if that's really what I meant. Kathryn, your positive energy has helped me continue to be passionate about my research even when the difficulties were leading to great frustration. Thank you for positive words and steadfast encouragement. After our first meeting my first year, you gave me an intro text book on galaxies to read and now I'm here. You're a large part in how I've come so far to this point. I have learned much from both of you that I will carry with me for the rest of my life.

Choosing Columbia for my PhD studies has been one of the best decisions of my life. The support of the entire department has made this a place where it was safe to learn, ask questions and grow. Thank you to everyone who I have encountered throughout my time as a graduate student but especially to my thesis committee - Greg Bryan, Zoltan Haiman, and Jacqueline van Gorkom - for your guidance and support throughout this process. To Munier, your unwavering support and tendency to push me into new things have helped define my time at Columbia. To Yuan, Emily, and Sarah - sharing an office with each of you has made going to work truly fun and led to close friendships that I will always value. To Ximena, Duane, Christine, Erika, David, Andrew, Jennifer, Adrian and all of the other graduate students at Columbia - thank you for making these six years memorable. To Summer for her general enthusiasm and for organizing the outreach events that remind me why I love

Astronomy in the first place. And finally, to Millie and Ayoune whose help and patience are the reason this thesis was approved by Columbia at all.

Yet without my experiences at the University of Pennsylvania I would never have pursued a PhD in Astronomy at all. In particular, I would like to thank Masao Sako for taking a chance on me and hiring an unknown sophomore with no experience and coaching me through my first research project and the rest of my undergraduate career. Those first steps are often the most important and for me they were a joy.

To my friends - Lindsay, Brian, Tammarah, Carolina, Maria - thank you for grounding me in the world outside of research. And to Amanda - thank you for being my emotional support as we transitioned together to a new city and to our new lives beyond undergrad. Having you as essentially my other half is how I've survived these past six years.

To Rachel, my oldest friend, knowing I always have you at my back makes moving forward so much easier. The number of times I called you to vent and share and gush means this is also your accomplishment in part too. After all, what's the brain without the brawn?

And finally, everything I do is with the support and love of my family. To my siblings, Deanne and Paul, I know I can always count on you to make me laugh, to knock me down a few pegs when necessary and to be there to help. Yous are the best.

And especially to my parents, Doreen and Paul. I don't know if you took me seriously when I said I wanted to work for NASA when I was nine but I'm here now because you've always told me that I could do anything I put my mind to and then supported me along whatever path I chose. I could not have done this without you.

2016, New York, NY

Chapter 1

Introduction

Do not look at stars as bright spots only. Try to take in the vastness of the universe.
– Maria Mitchell

The study of galaxies is, in the broadest terms, a study of how galaxies accrete gas, inefficiently form stars, and then energetically return the metals formed. Because they are not evolving in isolation, these processes are all affected by the galaxy's environment in the larger Universe such as cosmic filaments feeding the galaxies and mergers with other galaxies within the hierarchical structure formation paradigm of ΛCDM cosmology.

The goal of this thesis is to advance our understanding of galaxy evolution by constraining analytic models and hydrodynamical simulations with different observations of metals in both the gas and stars of nearby galaxies. In this initial section, we give an overview of the basic processes involved in shaping both the gaseous and stellar halos of Milky Way-like halos. We then present a more focused summary of the two primary observational considerations of this thesis - the Local Group Dwarf galaxies and the circumgalactic medium.

1.1 Overview of Galaxy Formation and Evolution

Galaxies are perhaps the most striking and complicated celestial bodies in the Universe. Once discovered to be not merely nebulae within our own Galaxy but distinct and distant objects in their own right, the question that naturally arises is how do these bodies form? This is shortly followed by: how quickly do they evolve?

Two opposing theories emerged to address these questions. Eggen et al. (1962) proposed that a galaxy was formed from a monolithic collapse of gas with the earliest stars forming on elliptical orbits in the halo and the later generations of more metal-rich stars forming into a disk as energy was dissipated and angular momentum conserved. In contrast, Searle & Zinn (1978) put forth the idea that parcels of gas could fragment and collapse at a range of times beyond the initial collapse of the central regions, better explaining the age and metallicity range of globular clusters in the stellar halo.

Remarkably, these two theories still have relevance within the modern framework of galaxy formation and evolution. Gas is expected to fall in from the virial radius of galaxies and feed and form the galactic disk as in Eggen et al. (1962), just over a much longer timeframe (e.g. Kereš et al. 2005; Joung et al. 2012; Nelson et al. 2015a). Furthermore, hierarchical structure formation reminiscent of Searle & Zinn (1978) is currently accepted as the basis of galaxy formation in ΛCDM cosmology. With a Universe dominated by dark matter, halos collapse into a range of masses depending on the initial density perturbation (Press & Schechter 1974). Smaller objects then continuously merge to form bigger halos such as the Milky Way. In addition to being the mergers of dark matter halos, these events also bring with them stars, creating both the diffuse stellar halo and the substructure within as observed in the halo of our own galaxy (Bullock & Johnston 2005) as posited by Searle & Zinn (1978). These mergers can also bring in gas, as clearly demonstrated by the in-falling

Large and Small Magellanic clouds (LMC and SMC) of the Milky Way (e.g. Putman et al. 1998; Brüns et al. 2005; Nidever et al. 2010) but also in the interaction of other nearby galaxies (Sancisi et al. 2008; Pearson et al. 2016).

In the remainder of this section, we present a short discussion of the properties and formation mechanisms of the stellar halo - the main component of stellar accretion in the Galaxy. This is followed by an overview of the primary processes of the gaseous halo - accretion and outflow - and their connection to the multiphase gas seen in the halo of the Milky Way and similar galaxies.

1.1.1 Stellar Accretion: the Stellar Halo and Satellite Galaxies

Surrounding the disk of the Milky Way is the stellar halo, a roughly spherical distribution of stars extending far beyond the disk, and the remaining satellite galaxies (see Helmi 2008, for an in-depth review). The stellar halo is kinematically distinct from the thick and thin disk components of the Galaxy (Majewski et al. 1996; Helmi 2008). The low metallicities of halo stars suggest that they are largely an accreted population which has been confirmed by many theoretical studies (e.g. Bullock & Johnston 2005; Bell et al. 2008). Relics of these accretion events are seen as substructure in the halo, most dramatically in the Sagittarius dwarf stream (e.g. Ibata et al. 1994; Majewski et al. 2003) but in a series of other streams as well (Belokurov et al. 2006). A smaller portion of the halo is also attributed to stars that have been kicked out of the stellar disk, though they can be identified by their kinematics and metallicities (Sheffield et al. 2012).

While the stellar halo represents the relics of the past merger history of the Milky Way, a population of surviving satellite galaxies has been observed and their numbers are growing. Stellar abundances of stars in these galaxies suggest that there are intrinsic differences between these surviving halos and their disrupted counterparts (Frebel et al. 2010; Kirby

et al. 2008; Lee et al. 2013) The properties of the current Local Group dwarf galaxies are discussed in Section 1.2.1 and the implications of their differences from the stellar halo are investigated in Chapter 2.

1.1.2 Gas Accretion and the Multiphase Halo

The form and rate of gas accretion onto galaxies from the intergalactic medium (IGM) is an ongoing area of active research. Following the theory of monolithic collapse, galaxies have long been thought to possess a diffuse hot halo of gas that has been shock-heated at the virial radius as it is accreted onto the galaxy (White & Rees 1978; Fukugita & Peebles 2006; Crain et al. 2010). Direct observational evidence for this hot halo comes from X-ray emission within a few kpc of the disk (Fang et al. 2006; Tyler et al. 2004). Indirect evidence for this "hot-mode" accretion suggests that the hot halo extends as far as 30 kpc to explain the head-tail structure of high velocity clouds (Westmeier et al. 2005) and even beyond to drive the ram-pressure stripping of dwarf galaxies within the Milky Way's virial radius (Grcevich & Putman 2009).

However, in recent years, with the advancement of cosmological simulations, the picture has become more complicated. In a ΛCDM universe, gas and galaxies are known to follow a filamentary structure, providing preferential directions for gas to flow into galaxies (Joung et al. 2012). Smoothed particle hydrodynamics (SPH) simulations have found that accretion of gas onto low mass and Milky Way-like galaxies before $z = 2$ was dominated by gas that was never shock-heated, remaining at $T \approx 10^4$ K and penetrating to the galactic disk (Kereš et al. 2005, 2009; Brooks et al. 2009; Stewart et al. 2011). HI observations of High Velocity Clouds (HVCs) in the Milky Way can tentatively be attributed as evidence for this "cold-mode" accretion (Wakker et al. 2001; Putman et al. 2002; Saul et al. 2012) but the rate of this accretion suggests that there is not enough mass in such clouds to completely fuel the

Milky Way's star formation (Putman et al. 2012). On the contrary, indirect absorption line studies of external galaxies suggests that there may be significant amounts of HI extending far from the centers of both active and passive galaxies but it is unclear if and how this gas will ever reach the disk for future star formation (Tumlinson et al. 2013a).

More recent adaptive mesh refinement (AMR) simulations (Joung et al. 2012) and moving-mesh simulations (Nelson et al. 2013, 2015a) of gas accretion suggest that the gas does not necessarily stay this cold. Instead, the majority of the gas of a Milky Way-like object at low-redshifts is neither hot nor cold when accreted but warm ($10^5 < T < 10^6$ K) though still flowing along filaments. This is supported by the high covering fraction of Lyman α absorbers seen around nearby galaxies (Bowen et al. 2002; Prochaska et al. 2011; Tumlinson et al. 2013a). Absorption studies also suggest that a more significant fraction of gas may lay within this temperature range than previously thought (Tumlinson et al. 2011; Werk et al. 2014).

Thus, the halo of a Milky Way-like galaxy is observed to have three distinct phases - cold, warm, and hot. Externally, absorption line studies of low-z galaxies show spatial and kinematic agreement between the cold/warm gas but a broadening of lines associated with warm/hot gas (Werk et al. 2013). However, the amounts and geometries of these different phases remain uncertain and any model of galaxy formation has to account for both their existence and their interplay.

1.1.3 Outflows and Feedback

Equally under debate is the form and significance of various forms of feedback in shaping the gaseous halos of galaxies. In the simulations, multiple forms of feedback are implemented to keep gas from over-cooling in the centers of galaxies and forming objects that are too bulge-dominated (e.g. Agertz et al. 2011; Brook et al. 2011; Piontek & Steinmetz 2011; Hummels

& Bryan 2012). The goal of the feedback is to efficiently remove gas to better match the stellar mass distribution function (Davé et al. 2011; Schaye et al. 2010; Nelson et al. 2015b) as well as to enrich the halo to the non-pristine levels that are observed (Scannapieco et al. 2006; Oppenheimer & Davé 2008; Wiersma et al. 2010; Ford et al. 2015).

The dominant feedback is generally agreed to be that of Type II supernovae (SNe) (Aguirre et al. 2001). These objects promptly explode after they have been formed and their efficiency can be tuned to reproduce global observed properties of galactic stellar disks (Governato et al. 2007). They are also a dominant source of metals, whose presence drives cooling and future star formation in the simulations (Scannapieco et al. 2005; Choi & Nagamine 2009; Hirschmann et al. 2013). However, other forms of feedback are known to exist and their strengths and effects are being steadily incorporated into different hydrodynamical simulations such as: cosmic rays (Brook et al. 2011; Salem & Bryan 2014; Salem et al. 2014), AGN (Sijacki et al. 2007; Booth & Schaye 2009) and radiation pressure (Hopkins et al. 2012; Agertz et al. 2013; Ceverino et al. 2014; Trujillo-Gomez et al. 2015). The interplay among these different physical processes has implications for the density, temperature, and metallicity structure of the gaseous halos of galaxies that are now beginning to be tested by observations (Hummels et al. 2013; Ford et al. 2015; Liang et al. 2015; Salem et al. 2015; Suresh et al. 2015b). Working towards better agreement between simulations and observations in this way is a fundamental step in advancing our theories on the evolution of gas in galaxies.

1.1.4 Summary

In summary, the evolution of galaxies is linked directly to the histories of their stellar halos, which hold keys to its dark matter merger history, and its gaseous halos, wherein gas accretion provides fuel for star formation and feedback removes gas and metals from the

galaxy center. While the methods may remain roughly the same over time - minor satellite mergers, filamentary flows, and star formation-driven feedback - these processes are expected to proceed differently for different mass halos (Scannapieco et al. 2006; Kereš et al. 2009; Nelson et al. 2013). However, it is small galaxies in the early universe that were the progenitors of the massive galaxies observed today. For a complete picture of galaxy evolution, it is necessary to understand how these early galaxies formed as well as how these massive galaxies are evolving currently.

To this end, this thesis examines simulated galaxies at two extremes: low-mass galaxies at high-redshift and high-mass galaxies at low redshift to better understand the metal signatures of stars and gas in cosmological simulations and in the context of a series of observations. The following sections provide an introduction to the main observational data used to constrain our current theories.

1.2 Observational Considerations I: Near-Field Cosmology and the Local Group Dwarf Galaxies

Unraveling the complicated history of galaxies like the Milky Way at low-redshift requires an understanding of the progenitor halos that formed it. Yet detecting these galaxies at the highest redshift is challenging and will remain so even with the advent of the James Webb Space Telescope (Okrochkov & Tumlinson 2010; Boylan-Kolchin et al. 2016). However, it is these smallest halos that are the most abundant at high redshifts and that drive both the inhomogeneous reionization (Bullock et al. 2000; Benson et al. 2002; Busha et al. 2010a) and chemical enrichment (Scannapieco et al. 2002; Salvadori et al. 2014) of the early Universe.

Instead of relying on direct observations, the field of near-field cosmology has developed to probe these early phenomena using the Local Group dwarf galaxies (for a recent review

see Frebel & Norris 2015). As relics of the early universe, their closeness allows for a detailed study of their structure and metallicities not available with direct searches. These metallicity measurements will provide the observational constraints for work in Chapters 2 and 3.

1.2.1 Properties of the Local Group Dwarf Galaxies

The number of observed satellite galaxies surrounding the Milky Way and Andromeda has rapidly expanded in the past 20 years thanks to the Sloan Digital Sky Survey (see Koposov et al. 2008, and the references therein), the Pan-Andromeda Archaeological Survey (McConnachie et al. 2009) and now the Dark Energy Survey (Drlica-Wagner et al. 2015). (McConnachie (2012) presents a full census.) These galaxies typically are broken into two groups: the "classical dwarfs" with $-17 \leq M_V \leq -8$ and the "ultrafaint dwarfs" (UFDs) with magnitudes fainter than this. They fall on the scaling relations defined by more massive galaxies, suggesting that they are a low-mass extension of the main galaxy formation process and not a special, distinct population (Tolstoy et al. 2009).

Similarly, the dwarf galaxies fall tightly onto a well-defined mass-metallicity relation (Kirby et al. 2013). In general, the smaller masses of the dwarf galaxies corresponds to lower average metallicities for the stars in each galaxy. This in turn implies a short, simpler star formation history (SFH) for these smaller objects in order to keep the amount of self-enrichment low. Color-magnitude diagrams of these objects suggest that they are comprised of ancient stellar populations, forming the majority of their stars before reionization (e.g. de Jong et al. 2008; Brown et al. 2014; VandenBerg et al. 2015). Furthermore, with the measured SFH, an expected number of SNe can be calculated and the amount of metals they should have produced estimated. By comparing the measured metallicities to the expected values if all of the metals were retained implies that some of these galaxies have lost as much as 99% of the metals they have produced (Kirby et al. 2011c), with some fraction likely enriching

the surrounding IGM.

Finally, all of the dwarf satellite galaxies (except the LMC and SMC) within the Milky Way are observed to be quenched (Grcevich & Putman 2009). Similarly, dwarf galaxies close to a more massive halo are preferentially devoid of gas when compared to field dwarfs (Geha et al. 2012). These results suggest that environmental factors can play a role in the evolution of these galaxies. In addition to quenching as they currently fall into a larger halo, these remaining dwarf satellites can be found on the outskirts of the main halo progenitors at early redshifts ($z = 10$), with implications for how cross enrichment might have proceeded (Corlies et al. 2013). However, at earlier redshifts, the volume occupied by the Milky Way was more representative of the universe as a whole, such that the sample may not be as biased as was first assumed (Boylan-Kolchin et al. 2016).

1.2.2 Stellar Abundances as SFH Indicators

Beyond their photometry, chemical abundance measurements of stars within these galaxies can better illuminate the metallicity and gas evolution at early times. Metals are produced by stars in their late-stage evolution: in AGB winds, in planetary nebulae, in Type II SNe and in Type Ia SNe. The supernovae are particularly important because the energy associated with the explosions is capable of spreading the metals to large distances and potentially even out of the galaxy, enriching both the IGM and neighboring galaxies (Wise et al. 2012b; Smith et al. 2011) However, the time scales and metals produced in these events varies, revealing details of the SFHs.

The most common diagnostic is the [α/Fe] vs [Fe/H] plane. Type II SNe result from stars with $11 \leq M_*/M_\odot \leq 40$, exploding roughly 10 Myr after being formed and producing most of the α elements (e.g. Ca, Ti, Mg) in the Universe (Woosley & Weaver 1995). As star formation proceeds initially, the assumed fixed yields of the SNe mean that the stellar

metallicities evolve as a straight line in this plane due to prompt Type II SNe enrichment. Once lower mass stars have had time to evolve into compact objects, Type Ia SNe can begin to explode. These SNe preferentially produce Fe which in turn increases the metallicity more rapidly than the α abundance (Binney & Merrifield 1998). This results in a "knee" in the [α/Fe] vs. [Fe/H] plane.

As the galaxy forms stars, tracks in this plane are generated by this continuous self-enrichment of the gas. The more massive halos form stars more rapidly such that the halos enrich to high metallicity before the start of Type Ia SNe, shifting the knee to high metallicities. The converse is true for the lowest mass galaxies where it is possible to observe no knee at all, just a steady decline. These general trends are confirmed by observations of stars in three different halo mass ranges (Robertson et al. 2005a).

In this way, any observation of lower [α/Fe] values at higher metallicities implies some form of extended star formation within the galaxy (Webster et al. 2015). Such stars have been observed even in the UFDs, which are thought to have some of the shortest SFHs (Vargas et al. 2013). Studies are also now expanding to include observations of neutron-capture elements (e.g. Ba, Sr) although the formation and yields of these elements are less certain, making their signatures harder to interpret (Roederer et al. 2010; Lee et al. 2013)

Historically, cosmological simulations only track a global metallicity field, such that any predictions for abundances must rely on ionization modeling and assumptions about the abundance ratios of elements (typically assumed to be the same as the solar abundances). Recently, a set of simulations has differentiated between metals generated by the first metal-free stars (Population III) and the metal-enriched stars that follow (Population II) (Wise et al. 2012b). Zolotov et al. (2010) explicitly followed metals in a Milky Way-like cosmological simulation but at lower resolution than what is necessary to trace the small halos corresponding to the dwarf satellites today. In general, the computational cost of running a

full cosmological simulation tracking these abundances is still prohibitive, although idealized models may make progress in the interim.

1.3 Observational Considerations II: Circumgalactic Medium

While the Local Group dwarf galaxies provide an excellent test bed of early galaxy formation and evolution, they ultimately represent only a piece of the total lifetime of a Milky Way-like galaxy. A complete picture of galaxy formation requires a deeper understanding of the flow of gas into and out of massive galaxies in the local Universe.

The multiphase structure of the gaseous halos of galaxies like the Milky Way is discussed in detail above. These gaseous halos are commonly referred to as the "circumgalactic medium" (CGM), gas beyond the main star-forming or stellar component of the galaxy but still within the virial radius. The CGM connects the star-forming centers of galaxies to their larger environment in the IGM. In general, the gas can be detected with two methods: indirectly though absorption lines found in the spectra of background quasars or directly through emission from the gas itself. However, the expected low densities and high temperatures of this gas make it particularly difficult to detect.

Typically, the absorption due to a given ion is strongest at temperatures close to the ionization energy of the given ion. Similarly, metal line emission from a given ion is strongest for the temperature at the peak of the cooling curve for the given ion. Bertone et al. (2013) quantifies the contribution of a large number of ions to the cooling of the diffuse Universe across a range of redshifts. For a Milky Way-like galaxy, the lines of Lyα, SiIII, CIII, CIV, and OVI are expected to be the dominant cooling lines (Furlanetto et al. 2004; Bertone et al. 2013; van de Voort & Schaye 2013). These lines are all located in the ultraviolet, making observations difficult unless they are done at higher redshifts where the lines have shifted

into the optical.

Measuring column densities and emission for a variety of metal lines can place better constraints on the physical properties of the gas being measured (Werk et al. 2014). However, modeling of both the data and the simulations typically makes a number of simplifying assumptions when utilizing the photoionization code, CLOUDY (Ferland et al. 1998). An observed absorber component or simulated gas cell is assumed to be of constant density, temperature, and metallicity as well as having a uniform extragalactic UV background (EUVB) as the source of photoionization (Haardt & Madau 1996, 2001, 2012). CLOUDY then calculates the ion fractions and and emissivities desired assuming ionization equilibrium.

Variations of the EUVB may not have an effect on the column density measurements at higher redshift ($z \approx 3$) (Sravan et al. 2015) but seem to produce large differences at low redshifts ($z \approx 0.2$) (see Chapter 4). The EUVB itself is also highly uncertain, with simulations of the Lyman α forest requiring a factor of 2-5 increase in the photoionization rate in the latest form of the EUVB (Kollmeier et al. 2014; Shull et al. 2015). Furthermore, simulations are also beginning to relax the ionization equilibrium assumption with potentially important consequences (Oppenheimer & Schaye 2013), though not as important as the temperature of the gas (Oppenheimer et al. 2016) and the computational cost of doing so remains high. Despite these uncertainties in the modeling, both absorption and emission studies have begun to illuminate the physical properties of the CGM and are the observational framework for the work described in Chapter 4.

1.3.1 Absorption Studies

At higher redshifts, Lyman α and the ultraviolet metal lines of interest have shifted into the optical, making observations easier and successful (Steidel et al. 2010; Simcoe et al. 2004). At low-redshift, several studies have begun pushing our knowledge of the more local CGM with

measurements of MgII (Chen et al. 2010) and OVI for a number of galaxies (Prochaska et al. 2011; Thom & Chen 2008). Recent surveys with Cosmic Origins Spectrograph have begun to characterize the CGM of Milky Way-like galaxies (COS-Halos: Tumlinson et al. 2011, 2013a; Werk et al. 2013), dwarf galaxies (COS-Dwarfs: Bordoloi et al. 2014) and massive galaxies with broad wavelength coverage (COS-GASS: Borthakur et al. 2015). As the data grow more numerous, they provide stronger constraints on the physical properties of the CGM that must be reproduced by cosmological simulations. Yet these observations are typically restricted to one sightline per galaxy, limiting our ability to place constraints on the distribution of the CGM of a single galaxy.

However, simulations have had difficulties reproducing these current observations of the CGM. Many seem to produce the correct amount of low ionization ions such as SiIII and CIII but simultaneously reproducing OVI has proved elusive (Hummels et al. 2013; Ford et al. 2015; Liang et al. 2015). Two exceptions include simulations with AGN feedback that is known to be too strong (Suresh et al. 2015b) and simulations including cosmic rays (Salem et al. 2015).

1.3.2 Emission Studies

Although more difficult because of the extremely low signal, emission observations have the added advantage of generating maps of the entire CGM of a single galaxy instead of probing a single line of sight to a background quasar. At high redshifts, surveys have found large amounts of Lyman α emitters (e.g. Bridge et al. 2013; Gawiser et al. 2007) and a growing number of the more extended Lyman α blobs/halos (e.g. Matsuda et al. 2011; Steidel et al. 2011, 2000), both of which are typically associated with highly star-forming galaxies. Metal-line emission, by nature much dimmer, has remained elusive (Arrigoni Battaia et al. 2015).

Recently, the development of new integral field units MUSE and KCWI has made it pos-

sible to generate entire maps of the CGM emission, complete with kinematics. Combining the extended spatial information with the kinematics of the gas has allowed for early observations of Lyman α emission to be linked to both global outflows (Swinbank et al. 2015) and filamentary inflows (Martin et al. 2014).

Because the observations are more limited, simulations examining emission are less numerous than their absorption counterparts. However, predictions indicate that the next generation of UV/optical instruments currently either in development or under discussion should be able to detect emission from the CGM of nearby galaxies (Furlanetto et al. 2004; Bertone & Schaye 2012; van de Voort & Schaye 2013; Sravan et al. 2015, and Chapter 4). The balloon-borne FIREBall-2 looks to build on its predecessor (Milliard et al. 2010) and its improved detectors (Hamden et al. 2012) could yield exciting new observations as early as next year. Further in the future, any proposed space-based UV/optical telescope will surely have the required resolution and sensitivity to provide emission maps of low-z galaxies.

1.4 Outline of Thesis

This thesis consists of three main chapters that aim to advance our understanding of galaxy evolution by using observed metal signatures of both gas and stars to constrain theoretical models. In particular, stellar abundances of Local Group Dwarf galaxies and column density measurements of the low-z CGM of Milky Way-like galaxies can be used to constrain the results of cosmological, hydrodynamical simulations.

Chapter 2 presents a study of the role of environment at high redshift on the chemical evolution of the surviving Local Group dwarf galaxies. In particular, we address the question of whether cross-pollution from the supernova-driven winds of nearby halos has a preferential non-effect on satellite galaxies in the early universe. We find that satellite galaxies progeni-

tors are preferentially located on the outskirts of the forming main halo and are more likely to be chemically isolated than their main halo counterparts. These differences can help explain discrepancies in measured stellar abundances between Milky Way halo stars and stars of the ultrafaint dwarf galaxies.

Chapter 3 expands on the previous chapter in examining the assumptions of the analytic models therein, specifically the extent of SN-driven winds and the inhomogeneous mixing of star-forming gas. It then provides an examination of the observable properties of the simulated galaxies. The galaxies can be classified into three different star formation history categories that are consistent with observations of the Local Group ultrafaint dwarf galaxies but the metallicity distribution functions of these simulated halos are typically too peaked and too metal rich. Still, the simulation does in fact generate complicated star formation histories and a spread in stellar metallicities all within a time period as short as 500 Myr.

Chapter 4 moves to the present day with the study of the CGM of a simulated Milky Way-like galaxy in the context of current absorption observations. The simulated column densities are found to be too low when compared to the data but a modification of the ionization assumptions, namely the strength of the extragalactic UV background, brings better agreement. The simulation is then used to predict direct emission signatures of multiple metal-lines for upcoming observations which in turn help to draw conclusions on the necessary surface brightness limits and required angular resolution for such detections. The evolution of the emission and its connection to the physical properties of the CGM is also explored.

Chapter 5 summarizes the main conclusions of this thesis and discusses potential directions for future work.

Chapter 2

Chemical Abundance Patterns and the Early Environment of Dwarf Galaxies

2.1 Introduction

For several decades now, hierarchical formation of dark matter halos, or small halos merging to form larger halos, has provided the framework for theories of galaxy formation. Within this paradigm, the stellar halo and substructures within it (such as satellites and stellar streams) can arise naturally from the accretion and subsequent disruption of dwarf galaxies (Bullock & Johnston 2005). A potentially serious challenge to this theory emerged when observations revealed systematic differences in abundances between stars in the classical dwarf spheroidals and those in the stellar halo: at [Fe/H]≈-2, halo stars were found to have higher [α/Fe] than those in the dwarf galaxies (see summary by Venn et al. 2004). If the

This chapter contains text from an article published in The Astrophysical Journal Letters, Volume 773, Issue 2, article id. 105, 8 pp. (2013).

stellar halo was built up from dwarf galaxies, how could these abundance differences exist? However, it was soon realized that the infalling objects that build the bulk of the stellar halo would have been accreted predominately at early times before the explosion of Type Ia supernovae, when only high-α stars would have had time to form. In contrast, the current dwarf spheroidal satellites would have typically been accreted at later times, allowing for some low-α stars to form from gas which had been polluted by Type Ia supernovae, which could account for the abundances differences (Robertson et al. 2005b; Font et al. 2006a).

More recently, further paradoxes in abundance patterns have emerged when examining lower-metallicity stars ([Fe/H] $\approx$ -3): neutron capture elements such as Barium and Strontium were found to have systematically lower abundances in the Ultrafaint dwarf satellite galaxies (UFDs) than in the Milky Way stellar halo (see compilation by Frebel 2010); and α-element abundances appeared to be higher in the classical dwarf satellites as opposed to the stellar halo (Kirby et al. 2011a). If we assume that the *progenitors* of the disrupted and surviving satellite galaxies are the same except for their accretion times, then we might expect the low-metallicity stars in both systems to have the same abundance patterns and any differences again seem to challenge the hierarchical structure formation paradigm. Alternatively, the disparity could be used to inform one about the nature of the progenitors. The dwarfs that form the satellite system of the Milky Way are potentially different from those that formed the stellar halo by virtue of the fact that they were accreted later and survived. The disparity in accretion times in turn suggest other possible differences between satellite and halo progenitors in the early Universe, in particular between their spatial locations and hence environment. Indeed, the nature of star formation in the first galaxies is expected to be heavily influenced by patchy re-ionization, inhomogeneous chemical enrichment from Population III stars and cross-pollution from neighboring systems. Thus, these abundance pattern differences can potentially serve as a unique window on these early times and speak

to the very way in which the Galaxy formed within the hierarchical model.

Abundance patterns are dictated by several factors. For example, larger systems are typically influenced by pollution from a more fully sampled stellar initial mass function (IMF). Thus, the effective yield from a combination of many different mass supernovae produces an averaged abundance pattern in the stars with small dispersion. Conversely, lower mass galaxies may be polluted by a more incompletely sampled stellar IMF and can be influenced by stochastic effects. In particular, Lee et al. (2013) showed the skew of the distribution of neutron capture elements in the UFDs relative to the distribution seen in the stellar halo could arise from the stars in the smaller objects being polluted by the highly-mass dependent yields of a small number of supernovae. Note, however, that this picture is only strictly true for galaxies evolving in isolation. If low mass galaxies happen to experience high levels of cross-pollution from their neighbors, the abundance patterns would then reflect the effective yield of many supernovae, leading to the same average value we would expect for more massive galaxies. Hence, it is the combination of galaxy mass and environment that determine the abundance patterns.

With this understanding, the measured abundance differences between halo stars and the UFDs can naturally be explained if one of these classes of objects is preferentially:

polluted — if the first stars have unique yields as is currently assumed, differences in the amount of pollution from these stars could be driving the abundance differences

isolated — if the dwarf galaxy progenitors are chemically isolated, their abundance patterns would reflect stochastic pollution, while the cross-polluting main halo progenitors would converge to an average

Both of these explanations require differences among the level of cross-pollution (and similarly isolation) experienced by these two classes of objects. This naturally leads to the main

questions that are the focus of this work: what is the role of cross-pollution and does it affect the progenitors differently? To what extent are the progenitors of the different classes of objects (i.e. satellites vs. the main halo) isolated at high z?

The most obvious way to address these questions is using detailed, cosmological, hydrodynamical simulations of the early formation and environment of a massive galaxy and its satellites. Such a simulation would need to track individual sub-galaxies forming in a Milky Way-like main halo at high redshift to the present day with high enough resolution to accurately follow inhomogeneous pollution from these halos and the effects on subsequent star formation (e.g. work by Simpson et al. 2013, suggests a resolution of better than 10 pc is needed to follow outflows from low-mass dwarf galaxies). State-of-the-art simulations are not yet able to meet these combined criteria. For example, Wise et al. (2010) followed the cross-pollution of dwarf galaxies in both dense environments and voids with a maximal resolution of 1 pc comoving using Enzo (Bryan et al. 2014). However, to meet these specifications, the simulation was only run to $z = 7$ instead of to $z = 0$ in a 1 Mpc box, which is too small to encompass the progenitors of a Milky Way-like halo. In comparison, Zolotov et al. (2010) is an example of cutting edge simulations of a Milky Way-sized halo run to $z = 0$ using GASOLINE (Wadsley et al. 2004). Their simulations included stellar feedback as well as metal enrichment, cooling and diffusion. However, computational cost dictated that these simulations were of lower resolution than those of Wise et al. (2010), which compromises their ability to accurately follow outflows and metal mixing on the small scales of interst here. These two works demonstrate the difficulties involved in tracing the effects of high-z environment and star formation until the present day in a single simulation for both Eulerian and Lagrangian codes. Moreover, neither type of code is yet able to follow all the relevant physics directly but rather rely on sub-grid models that are calibrated to observations.

Our own interest in examining how differences in high-z environment affect present day

abundance signatures in dwarf galaxies lies at the intersection of these two simulations. Higher resolution than Zolotov et al. (2010) is required to trace low-mass progenitors at early times and larger volumes than Wise et al. (2010) run to present day are needed to examine a Milky Way-like galaxy. Thus, to motivate the intense computational costs of such a simulation, this paper takes a first look at how high-z cross-pollution varies within a Milky Way-like halo using more simplified techniques. In Section 2.2, we use an N-body simulation to trace where objects identified today came from in the early universe and whether these high-z spatial locations can vary systematically with progenitor type. In Section 2.3, we use an analytical model of supernova-driven winds to estimate if the importance of cross-pollution might differ across the progenitors of different objects. Finally, our conclusions are presented in Section 2.4.

2.2 Results I: Origin of Progenitors

To begin to address the role of early environment in shaping stellar populations, the basis is an N-body simulation, described below, where the origins of the progenitors of the current main halo and dwarf galaxies are first identified. In particular, we are interested in investigating if there are systematic differences in spatial location of those progenitors at *high-z* that reflect systematic differences in spatial location at *low-z* of the main halo and its satellites and if these differences have observable consequences.

This approach is inspired by Diemand et al. (2005a) who showed that early ($z \gtrsim 10$) high-σ peaks in density fluctuations influenced the present-day spatial distribution and kinematics of protogalactic systems. They found that material associated with these rarer peaks was more centrally concentrated in their present halos and moved with a lower velocity dispersion on more radial orbits. Here, a similar question is asked but in the reverse sense. Instead of

tracing structures forward in time, we ask: where do the structures seen today come from?; and is there a systematic difference in where objects such as dwarf galaxies form as opposed to where the main halo forms?

2.2.1 Method: N-Body Simulation

The N-body simulation that is the underpinning of this work is described by Tumlinson (2010a). A Milky Way-like halo was identified from within a full cosmological simulation of a periodic cubic box of comoving size $7.320h^{-1}$ Mpc in one dimension using Gadget2. (ver 2.0; Springel 2005) The main halo was found to have a virial mass of $M_{200} = 1.63 \times 10^{12} M_{\odot}$ and a virial radius of $R_{200} = 381$kpc. The Milky Way-like halo was then re-simulated with the central portion of the galaxy having a higher resolution (512^3) while the rest of the box was run at a lower resolution (256^3) to save time. At the 512^3 resolution, the dark matter particles had a mass of $M_p = 2.64 \times 10^5 M_{\odot}$. The gravitational smoothing length for all simulations was 100 pc in comoving coordinates. Subsequently, the six-dimensional friends-of-friends algorithm (Diemand et al. 2006) was implemented to identify all bound halos with a mass of at least 8×10^6 $M_{\odot}$ at each time step in the simulation. The algorithm identified the main halos as well as the small halos embedded within their larger potential well at later times. At $z = 0$, 11,698 halos were identified while the number decreases to 4,675 at $z = 10$.

Furthermore, a semi-analytic star formation history was prescribed for each halo, which was then used to identify luminous satellites at z=0. This star formation history included chemical and kinematic feedback as well as reionization. Details can be found in Tumlinson (2010a) Section 4. The prescription reasonably matched observed traits of the Milky Way and its satellite populations. For the simulation's main halos, both the overall stellar mass and the stellar mass density profiles were well reproduced, indicating that the chosen parameter values of the basic baryon assignment and star formation prescription were well

chosen. In addition, the prescription matched both the luminosity function and the metallicity distribution function of the Milky Way satellites, demonstrating that the implemented feedback was accurate down to the smallest mass scales of interest. For these reasons, this work assumes all the fiducial values of Tumlinson (2010a) in our own models with high confidence.

2.2.2 Main Halo and Dwarf Progenitor Clustering

We are interested in comparing the early environment of main halo progenitors with that of dwarf galaxy progenitors by analyzing two snapshots from the full simulation described above. Figure 2.1 shows the $z = 0$ snapshot. We identify particles within the inner 25 kpc of the main halo as "main halo particles" in blue. (Note that the cost of high-resolution spectroscopy means that abundance distributions for the stellar halo have typically been derived from even more local stars, so including halo particles at greater distance from the center would not fairly represent the observed samples — see, e.g., Venn et al. 2004). Dwarf galaxies are defined as surviving, non-dark subhalos at $z = 0$ (i.e. those that are assumed to contain stars using the semi-analytic prescriptions of Tumlinson 2010a). We identify 124 surrounding halos as dwarf galaxies from the previously constructed halo catalogues and tag these particles as "dwarf galaxy particles" in red.

Figure 2.1 shows two projections of the second snapshot at $z = 10$. Here we locate the same sets of particles identified at $z = 0$ (halo in red, satellites in blue) to examine their formation environment. This redshift is the redshift of reionization in the full model, at which point star formation is truncated in the dwarf galaxies and smaller main halo progenitors (see Tumlinson 2010a), making it a logical choice for studying the early environment. At such early times, more than 80% of eventual main halo and dwarf galaxy particles are still not bound to any progenitor halo. As an example, overplotted on the particles are all

bound halos that contain any of these particles with mass greater than $10^8 M_\odot$. Main halo progenitors are represented as squares and the dwarf galaxy progenitors are represented as stars in Figure 2.2. Visual inspection of these projections is enough to demonstrate that one cannot simply assume that the formation environments of dwarf galaxy progenitors and main halo progenitors are the same. Instead, dwarf galaxy progenitor particles appear to sit preferentially outside of the main halo progenitor particles, which are clustered in the center of the formation region. Expressed more quantitatively, 50% of the main halo particles can be enclosed in a physical radius of 60 kpc while a physical radius of 150 kpc is needed to enclose 50% of the dwarf galaxy particles. Making similar plots for three additional Milky Way-like galaxies displayed the same relations. Thus, we expect that all further calculations are not specific to the halo examined here but are a general result of hierarchical structure formation.

We conclude that the dwarf galaxy progenitors and main halo progenitors have distinctly different spatial locations at $z = 10$. However, the spatial isolation of the dwarf galaxy progenitors does not ensure their chemical isolation. To determine that these progenitors are also chemically isolated, we now examine pollution due to supernova-driven winds.

2.3 Results II: Cross-Pollution

Winds driven by Type II supernovae (SNe II) are considered to be one of the main mechanisms for enriching the intergalactic medium (IGM) with metals (Aguirre et al. 2001). It follows that inhomogeneous pollution from these winds, especially in the form of preferential cross-pollution of certain halos, could have large effects on the abundance patterns of stars forming in different regions of space. Given the differences in spatial locations of main halo and dwarf galaxy progenitor particles observed in our simulations, we could expect to see

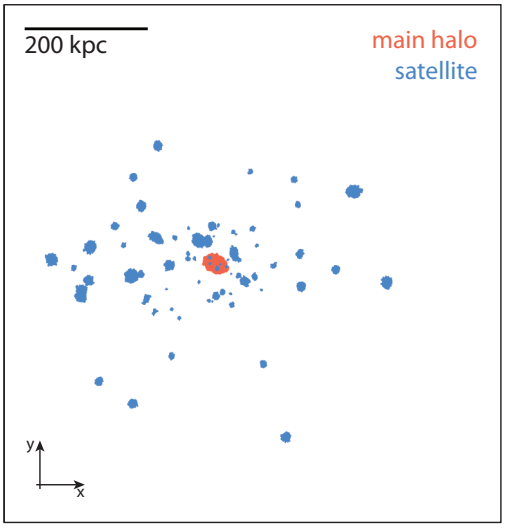

Figure 2.1: Plotted is x-y projection of the $z = 0$ snapshot of the simulation. The main halo sits in the center (red) and is surrounded by the dwarf galaxies (blue)

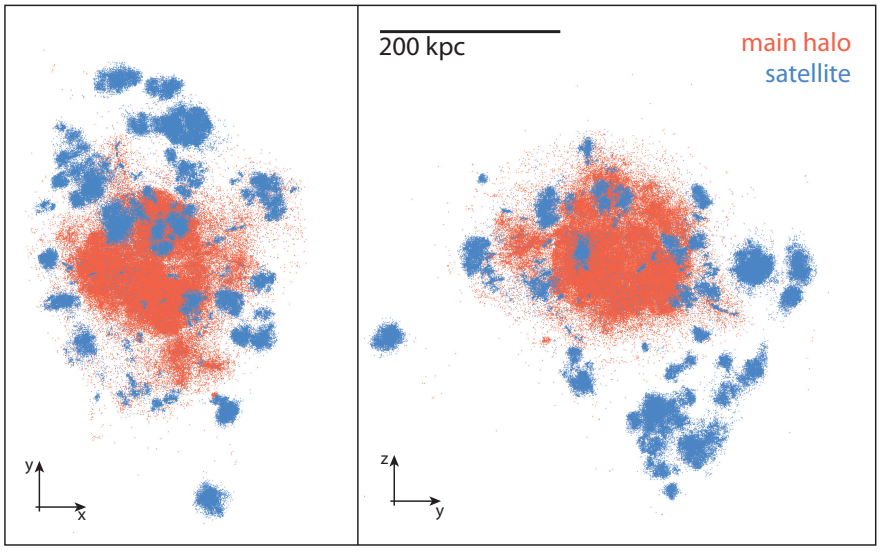

Figure 2.2: Plotted are x-y (left) and y-z (right) projections of the $z = 10$ positions of the particles that comprise the main halo (red) and dwarf galaxies (blue) at $z = 0$. Bound halos at $z = 10$ with mass greater than $10^8 M_\odot$ that contain any of these particles are overplotted as a square for main halo progenitors and as a star for dwarf galaxy progenitors.

differences in cross-pollution across these two classes of progenitors.

To follow cross-pollution, we build on previous work that semi-analytically calculated radii of SN-driven bubbles. Our predecessors were interested in examining these SNe as a way to drive reionization (Tegmark et al. 1993a) as well as looking at how they advanced metal enrichment to better understand metal absorption lines (Furlanetto & Loeb 2003) and the locations of the first stars (Scannapieco et al. 2003). These works were focused on global enrichment or reionization of the IGM by galaxy populations, and so averaged over many halos in large volumes and considered longer timescales.

While the scheme used here is similar to previous work, we have a significantly different motivation. Instead of examining more global processes, we are looking at a single forming galaxy for a short part of its early history. Furthermore, we have the advantage of using a full N-body simulation as the spatial basis. This allows us to look at how the winds are spatially distributed on these smaller scales as well as the level of cross-pollution among the halos.

In order to investigate cross-pollution, we implement a basic SN-driven wind model as in these previous works and apply it to individual halos from the N-body simulation. The method is described in the Section 2.3.1 while the results are presented in Section 2.3.3.

2.3.1 Bubble Evolution

The SN-driven winds are modeled analytically as spherically symmetric, thin shells in an expanding universe (with density parameters for dark energy, dark matter and baryons of $\Omega_\Lambda = 0.762, \Omega_M = 0.238, \Omega_b = 0.0416$ respectively and Hubble constant, $H_0 = 73.2$ km s^{-1} Mpc^{-1}) of zero pressure and constant IGM density, $\bar{\rho}$. The shell is assumed to sweep up almost all of the baryonic IGM that it encounters. With these assumptions, the evolution

of the shell radius, R_s, is given by:

$$\ddot{R}_s = \frac{3P_b}{\bar{\rho}R_s} - \frac{3}{R_s}(\dot{R}_s - HR_s)^2 - \Omega_m \frac{H^2 R_s}{2} \tag{2.1}$$

where the overdots represent time derivatives and the subscripts s and b indicate shell and bubble quantities respectively. The first term in Equation 2.1 describes how the interior pressure, P_b, drives the bubble expansion. The bubble is slowed by the fact that newly swept up mass must be accelerated from its Hubble flow velocity, HR_s, to $\dot{R}_s$ so that the second term in Equation 2.1 represents a net braking force. Finally, the third term represents the gravitational pull from the mass interior to the shell which again decelerates the shell.

The pressure, P_b, that drives the bubble is provided by the SNe, which have a net input of energy into the system with a rate equal to

$$\dot{E}_b = L(t) - 4\pi R_s^2 \dot{R}_s P_b. \tag{2.2}$$

Here, $L(t)$ is the luminosity of the SNe and the remaining term is the typical work done by the shell as it expands. Lastly, adiabatic expansion is assumed such that $P_b = E_b/2\pi R_s^3$.

The only unique function that can be specified in the above equations is the SNe luminosity as defined by the halo's star formation history and its mass accretion history. Prescriptions for both mass accretion and star formation are implemented and are described below.

2.3.2 Mass Accretion Histories

The mass accretion history of each halo is calculated using the formalism of Wechsler et al. (2002). After examining a large range of full mass assembly histories from high resolution

N-body simulations, they found that the following simple parameterization captured most crucial aspects of the growth in the mass of a halo, $M_{\rm halo}$, over time:

$$M_{\rm halo}(z) = M_0 \exp\left[\frac{-S}{1+z_c}\left(\frac{1+z}{1+z_0}-1\right)\right] \tag{2.3}$$

where S=2.0, z_0 was the observing redshift and M_0 was the observed mass at that redshift. The characteristic formation time, z_c was defined to be:

$$1+z_c = \frac{c_v}{c_1}(1+z_0) \tag{2.4}$$

where c_1=4.1 was the typical concentration of a halo forming at $z = 0$ and $c_{\rm vir}$ was the concentration of the halo in question.

Individual halos can deviate significantly from this simple form, especially around a major merger. However, using this type of smooth, continuous accretion history instead of the actual simulated histories is justified as there is not expected to be many major mergers at this early time or during such a short time period. Furthermore, this semi-analytic parameterization was chosen over the full merger history for each halo because it was straightforward to incorporate into the wind model without much loss of accuracy.

For this study, the N-body simulation is used to find the virial radius and half-mass radius of the subhalos identified by the group finder at $z = 10$ that contain eventual main halo and dwarf galaxy particles. We can then calculate the concentration of each halo for which we assign a mass accretion history.

2.3.2.1 Star Formation Histories and Supernovae Luminosity

The final step in defining the SN luminosity is prescribing a star formation history for each halo. We use a simplified version of the prescription applied in Tumlinson (2010a). Dark

matter halo masses, from Equation 2.3 are converted to baryonic gas masses with a fixed efficiency prior to reionization:

$$M_{\rm gas} = f_{\rm bary} \times M_{\rm halo} \tag{2.5}$$

where $f_{\rm bary} = 0.05$.

In any time interval, Δt, the mass of stars formed is:

$$M_{\rm star} = \frac{M_{\rm gas}\Delta t}{\tau_{\rm sf}} \tag{2.6}$$

where $\tau_{\rm sf} = 10$ Gyr.

Finally, following Tumlinson (2010a), we assume that 1 $M_\odot$ of star formation yields 0.01 SNe for a Kroupa (2001) IMF and that each supernova produces 10^{51} ergs of energy. This comes from integrating the IMF for the number of stars between 8-40 $M_\odot$ which yield such supernovae and normalizing to 1 $M_\odot$. Thus, the SNe luminosity can be defined as:

$$L = (0.01\ {\rm SNe/M_\odot})(10^{51}{\rm ergs/SNe})\ \frac{f_{\rm bary}M_{\rm halo}}{\tau_{\rm sf}} \tag{2.7}$$

This SNe luminosity differs significantly from the previous works cited above (Tegmark et al. 1993a; Scannapieco et al. 2003; Furlanetto & Loeb 2003). They chose to have a single starburst per galaxy while we allow for more realistic, continuous star formation. Furthermore, dissipation effects are not included, such as the ionization of the swept-up IGM or heating of the shell and interior plasma. Thus, these estimates give an upper limit for the wind radius and maximize the effects of cross-pollution. (In general, this choice is insignificant because of the short integration time, and the radius changes by at most 2% when dissipation is included.) Because the principle objective of this work is to explain abundance pattern differences in stars with [Fe/H] $\approx$ -3, we also do not model the prior

presence of Population III stars in the galaxies. These stars will simply provide the initial enrichment necessary for star formation at the metallicities considered here.

Finally, a treatment of reionization is not included because the process is still not well characterized on these small scales. In reality, each of the supernova-driven bubbles would have been preceded by a reionization front, potentially limiting further star formation in neighboring halos. However, the importance of inhomogeneous reionization *within* a Milky Way-like galaxy is only just being studied (e.g. Ocvirk & Aubert 2011), with most previous work concentrating on global (and typically external) influences on the entire satellite system (Busha et al. 2010b; Lunnan et al. 2012). Furthermore, any simple analytic treatment of reionization is dependent on the value of the escape fraction of the ionizing photons, which is currently not well known. Thus, rather than using a poorly constrained reionization model, we point out that including reionzation can only strengthen these results as reducing or even truncating star formation in neighboring systems can only lessen the bubble radii and overlap.

2.3.2.2 Integration Time

The final piece needed to compute the supernova-driven wind radii is the time over which to integrate the star formation histories. This time frame needs to result in stars with a metallicity consistent with those of the low-metallicity stars whose abundance patterns we seek to explain. In order to make an order-of-magnitude estimate of a halo's metallicity, we use a simple closed box model with all metals produced by the SNe remaining in the host halo (as described in Binney & Merrifield 1998). Although a mass accretion history is assumed (Section 2.3.2), this closed box assumption is valid because over the short time we consider, a typical 10^8 $M_\odot$ halo accretes less than 2% more dark matter and gas. Furthermore, it is assumed that all the metals ejected by the supernovae are evenly and instantaneously mixed

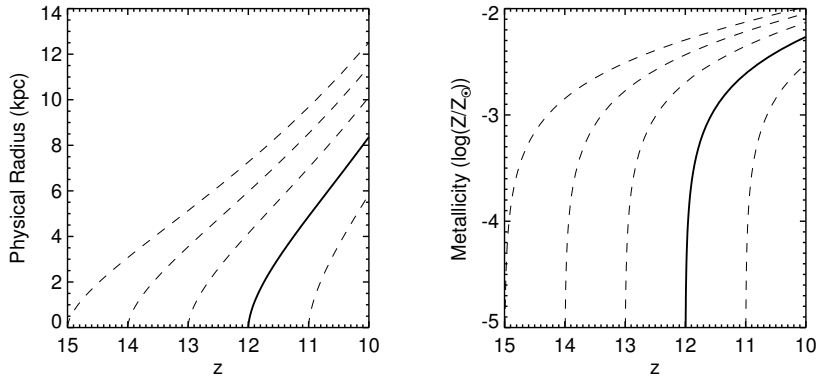

Figure 2.3: In the left-hand panel, the physical radius of the SNe-driven wind is shown as a function of redshift. In the right-hand panel, the metallicity is plotted as $\log(Z/Z_{\odot})$ for a 10^8 $M_{\odot}$ halo as a function of redshift. In the right, the mass in stars as a function of redshift is shown. The metallicity directly reflects the amount of gas that is being turned into stars. The final values of each quantity do not vary much as a function of the starting redshift. The solid lines indicate a starting redshift of $z = 12$ and are the values adopted henceforth.

throughout the entire bubble. Using the star formation history described in Section 2.3.2.1, it is then straightforward to show that the closed-box model becomes:

$$Z(t) = -p \ln \left[1 - \frac{t}{\tau_{\rm sf}} \right]. \tag{2.8}$$

Thus, because of the simplicity of this model, a star formation rate that is proportional to the dark matter mass and an identical start time for star formation all halos, the metallicity depends only on the time passed since the beginning of star formation. A single metallicity value for all of our halos is produced. The metallicity is plotted as $\log(Z/Z_{\odot})$ for a 10^8 $M_{\odot}$ halo in the right-hand panel of Figure 2.3 as a function of redshift for a variety of start times. Overall, the plot suggests that these halos should be forming stars at $z = 10$ with an approximate metallicity of $\log(Z/Z_{\odot})$= -2.25, regardless of when star formation begins. This simple estimate is consistent with time and mass dependent chemical evolution models from

Tumlinson (2010a), for these same simulated halos. This demonstrates that the metallicity of the stars at this time are expected to be in the range of the low metallicity stars with observed abundance differences.

2.3.3 Findings

Physical bubble radii for every progenitor halo are calculated by beginning star formation at $z = 12$ for all progenitor halos found at $z = 10$, with the results being fairly insensitive to this choice in starting redshift. In the left-hand panel of Figure 2.3, the radius is plotted as a function of z for an example halo taken from the simulation with a mass of 10^8 $M_\odot$ and a measured concentration of 6.57. This shows that the scale of the radii is roughly consistent with the work of Tegmark et al. (1993a), Scannapieco et al. (2003), and Furlanetto & Loeb (2003) with the differences arising from the differences in our luminosity function, described above.

For completeness, the radius evolution is also shown for a number of starting redshifts extending to $z = 15$. We find that while the choice in starting redshift does have an effect on the final radius at $z = 10$, the change in radius is small enough that it does not affect our conclusions concerning cross-pollution.

The order of magnitude of the bubble radii also demonstrates that the halos have the ability to pollute a large surrounding volume, even at this early time. For a sense of scale, Figure 2.4, where we plotted main halo (red) and dwarf galaxy (blue) progenitor particles, is shown again with the bubble radius overplotted for each halo. To most clearly demonstrate the result, only bound halos with mass greater than $10^8 M_\odot$ are included again. This projection indicates that the bubbles of main halo progenitors overlap more often than their dwarf counterparts. Thus, one might expect that because of their clustering in the center, main halo progenitors would have a higher level of cross-pollution while the dwarf galaxy

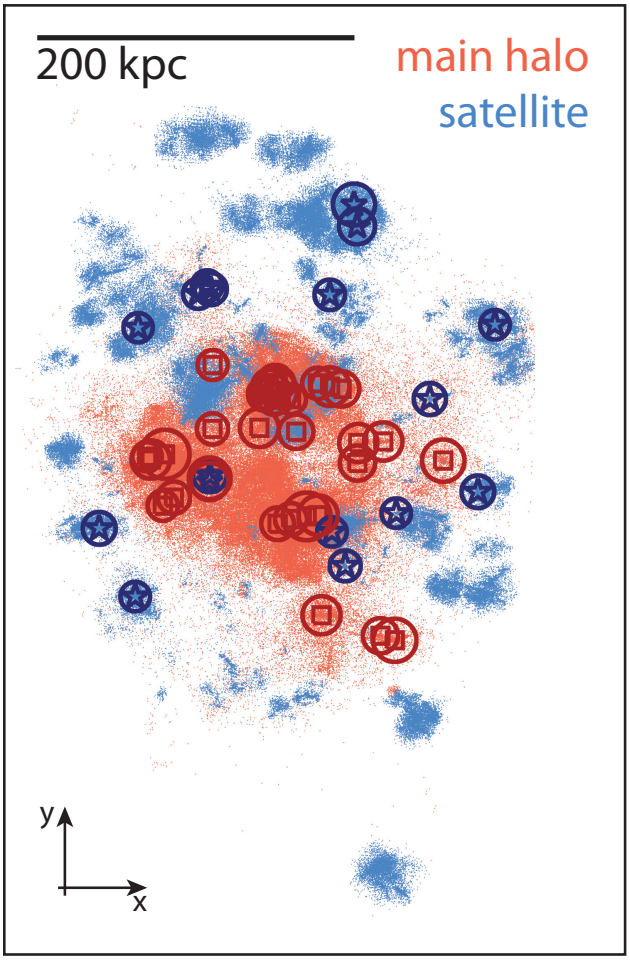

Figure 2.4: Figure 2.1 is again presented but now with the shells of the SN-driven winds overplotted with main halo progenitors in red and dwarf galaxy progenitors in blue. For simplicity, only those bound halos with mass greater than $10^8 M_\odot$ and their radii are shown. The main halo progenitors (squares) are more centrally located with an apparently higher cross-pollution rate while the dwarf galaxy progenitors (stars) remain more isolated on the outskirts.

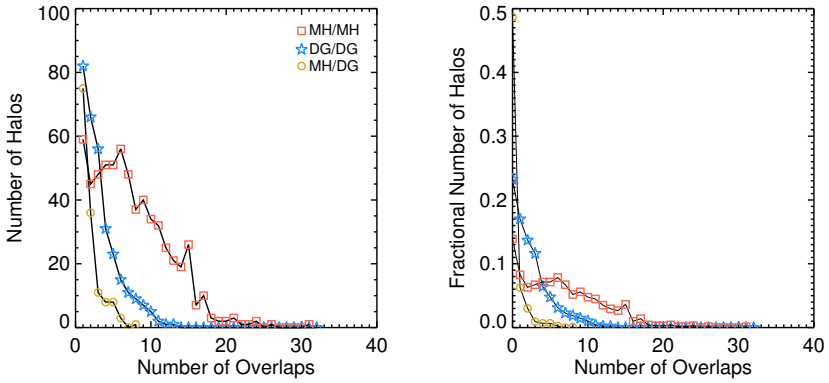

Figure 2.5: The left panel demonstrates that the bubbles of main halo progenitors (squares) overlap more often than those of their dwarf galaxy counterparts (stars). Cross-pollution among main halo and dwarf galaxy progenitors (circles) is rarer and typically only involves one crossing. The right panel, plotting the fraction of halos per crossing, shows that this trend is not simply due to the larger number of main halo progenitors.

progenitors would remain more isolated. This type of non-uniform pollution is easily seen in Wise et al. (2010) (Figure 2.1). Closely clustered halos are much more capable of spreading their metals amongst themselves and this pollution is seen to affect how star formation proceeds in such instances. Because of computational limitations, these halos are unable to be identified as either main halo progenitors or dwarf galaxy progenitors in the manner described here.

The left panel of Figure 2.5 illustrates the significance of cross-pollution and this potential pollution bias by showing the number of times the bubbles of the different classes of progenitors cross. The bubbles were defined as crossing if the distance between the centers of the two halos was less than the sum of their radii. It shows that main halo progenitors tend to cross-pollute other main halo progenitors (squares) much more often than dwarf galaxy progenitors cross-pollute other dwarf galaxy progenitors (stars). Moreover, main halo and dwarf galaxy progenitors (circles) rarely cross-pollute each other. In the right panel, we plot the fraction of each halo crossing category as a function of the number of crosses,

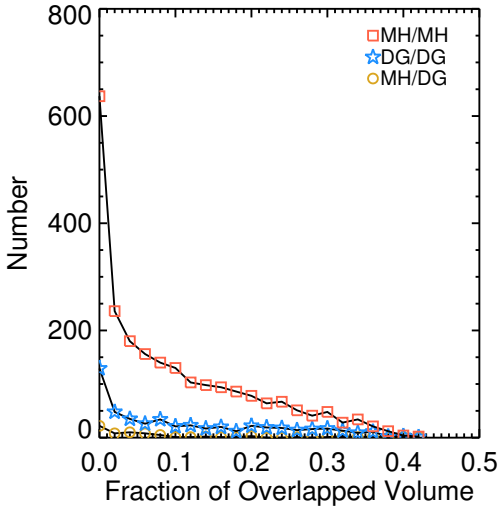

Figure 2.6: The fraction of volume overlap for each pair of bubbles is illustrated. Not only do main halo progenitors (squares) cross-pollute each other more often but the generally higher volume overlap indicates that they also do so more effectively.

thus demonstrating that the effect is not simply due to the fact that there are a larger number of main halo progenitors. Most importantly, we find that approximately 10% of all main halo progenitors and approximately 25% of dwarf galaxy progenitors experience no cross-pollution of any kind. Thus, a significant fraction of dwarf galaxy progenitors remain chemically isolated as late as $z = 10$.

Because it is not expected that actual pollution to be exactly spherical, simply examining whether bubbles cross or not might not represent true cross-pollution. Thus, a more significant calculation is what fraction of the two bubbles' volumes overlap. This is defined as the volume of overlap divided by the sum of the two individual bubble volumes. Bubbles that have a large fractional volume of overlap have a much higher probability of cross-pollution regardless of potential asymmetries in the bubble structure. For simplicity, we calculate the fractional volume of each pairwise overlap without considering multiple bubble overlaps. While this some of the overlap volume is over counted, we are better mea-

suring the importance of each crossing individually. Figure 2.6 indicates that the fraction of overlapping volume ranges from a small fraction to as high as 40% for cross-pollution among main halo progenitors (red) and dwarf galaxy progenitors (blue). Thus, with similar volume distributions, the higher number of main halo crossings truly represents a higher level of cross-pollution. On the other hand, the majority of main halo - dwarf galaxy cross-pollution events involve less than 10% of the volume involved. Thus, the spread in the fractional volume overlap reinforces the significance of the spatial dependence of the cross-pollution.

However, because we examine such early times, many of the dwarf galaxy progenitors will merge to form larger dwarfs by $z = 0$. Thus, some of the dwarf galaxy progenitors that cross-pollute each other at early times could eventually merge to form a single, stellar population that are then observed in the present. These will then become one observable chemical system, which conceals the effects of the cross-pollution. Looking at $z = 0$ dwarf galaxy satellites with masses greater than 10^8 $M_\odot$, we find that approximately 60% of these halos are composed of cross-polluting progenitors which have since merged into one halo. That is, only a minority of $z = 0$ dwarf galaxies would share a chemical evolution history.

In summary, we conclude that main halo progenitors cross-pollute each other more frequently and more completely in terms of volume whereas dwarf galaxy progenitors tend to be much more isolated objects, both from the main halo and from one another. Furthermore, the majority of dwarf progenitors that are cross-polluting each other at $z = 10$ eventually merge into a single halo at $z = 0$. The number and extent of different halo crossings is likely to vary with different numerical realizations (and hence between different galaxies in the real Universe.) However, the overall trends found concerning preferential isolation of dwarf galaxy progenitors is expected to be robust.

2.4 Conclusion

We set out to look at how the hierarchical nature of structure formation influences the histories of objects that survive today as satellites of a larger galaxy compared to those that are accreted and destroyed during the same galaxy's formation. In particular, we are interested in whether there could be any systematic differences in spatial location and environment between satellite and halo progenitors at early times, and what these differences might mean for low-metallicity stellar populations in these systems today.

In summary, we have found at $z = 10$ that:

- main halo progenitor particles lie clustered together while dwarf galaxy progenitor particles are found on the outskirts of this cluster.

- supernova-driven winds tend to cross-pollute main halo progenitors more than dwarf galaxy progenitors with a higher fraction of dwarf galaxy progenitors remaining chemically isolated than their main halo counterparts.

- a majority of dwarf galaxy progenitors that are cross-polluting at $z = 10$ eventually merge to form a single halo at $z = 0$.

Previous work predicting detailed abundance patterns which used semi-analytical and statistical techniques have typically assumed chemical isolation of their stellar populations (Karlsson 2005; Leaman 2012; Lee et al. 2013). Dwarf galaxies appear to satisfy this assumption due to their spatial separation from surrounding halos. However, higher levels of cross-pollution for main halo progenitors and thus stellar halo stars suggest that this external source of metallicity could affect the measured abundance patterns and should be included in these types of models.

These results also have important implications for future chemical abundance studies. For example, recently Brown et al. (2012) have shown that the UFDs contain what are effectively single age stellar populations that are at least as old as approximately 13.7 Gyr, the age of the ancient globular cluster M92. These primeval populations are likely good tracers of early chemical enrichment or even of a single early or primordial supernova. Moreover, if they are chemically isolated from one another as well as the main halo, they are each a unique laboratory for chemical evolution and SN yield tests. Thus, we can view the Local Group overall as having hundreds of such independent chemical histories, instead of one or two common enrichment histories dominated by the most massive halos. Furthermore, the independent nature of the early enrichment of different local systems suggests that each could potentially have distinct chemical signatures.

Overall, we conclude that the isolation of dwarf galaxy progenitors can be appealed to as an explanation for current observations of abundance distribution differences between low metallicity stars in satellite galaxies and in the halo. Conversely, as our data set become more extensive, we might hope to use abundance differences to tell us about the progress of metal enrichment on Local Group scale in the early Universe.

Acknowledgments

The authors gratefully acknowledge useful conversations with Zoltan Haiman. LC and KVJ were supported in part by NSF grants AST-0806558 and AST-1107373.

Chapter 3

Exploring Simulated Early Star Formation in the Context of the Ultrafaint Dwarf Galaxies

3.1 Introduction

Since their discovery, dwarf galaxies in the Local Group have been thought to probe both the early universe and to represent the early building blocks of the larger Milky Way galaxy (Dekel & Silk 1986; Diemand et al. 2005b; Font et al. 2006b; Frebel & Bromm 2012). In particular, the smallest of these, the ultrafaint dwarf galaxies (UFDs), were proposed to host simple stellar populations with star formation histories that were truncated by reionization (Bovill & Ricotti 2009; Salvadori & Ferrara 2009; Tolstoy et al. 2009, for a review). Their overabundance of α-elements relative to their metallicity is one signature of early and short star formation (Kirby et al. 2011b; Vargas et al. 2013).

This chapter contains text yet to be submitted for publication.

However, as observations continue to be made, the star formation histories (SFHs) of these small objects are revealed as being more complex than first thought. Deep color-magnitude diagrams (CMDs) of six UFDs as well as their spectroscopically derived spreads in metallicities suggest that while the stars are all consistent with ancient ages (that is forming more than 10.5 Gyr ago), the SFHs can be best fit with a two-burst model, although a single burst model cannot be ruled out and in some cases is in fact the best fit (Brown et al. 2014). Yet when the data are expanded and the [α/Fe]-[Fe/H] plane is considered, the data seem to prefer continuous star formation. That is, in order to reproduce the stars seen with lower [α/Fe] values at higher [Fe/H], time must be allowed for self-enrichment from Type Ia supernovae to be incorporated into the stellar metallicities (Webster et al. 2015). One exception is Segue 1, whose metallicity distribution function (MDF) has distinct peaks that can be described with discrete bursts of star formation (Webster et al. 2016). Thus, a more complete picture of the early star formation in these small galaxies can be better reconstructed by combing the CMDs, MDFs, and α-abundances.

Interpreting the metallicity and abundance data in such ways typically relies on an underlying chemical evolution model. Using simple yet powerful parameterizations, these models can trace the build up of iron and other elements as stars form within a galaxy of a given mass, creating tracks in abundance/metallicity space that recreate what is seen in studies of Milky Way halo stars (McWilliam 1997). Whether purely analytic (Robertson et al. 2005a; Andrews et al. 2016), coupled to an N-body simulation (Tumlinson 2010b; Romano & Starkenburg 2013; Crosby et al. 2016), or incorporating global, measured SFRs (Avila-Vergara et al. 2016; Lanfranchi et al. 2008), these models allow for quick variation of the parameters and for an assessment of the importance of a number of basic galaxy properties (inflows, outflows, SFH, etc.) in driving the chemical evolution of a given halo. However, an underlying assumption of all of these models is the complete mixing of metals within a halo

once returned from stars to the modeled ISM, whether instantaneously or within a parametric timescale. Furthermore, halos are typically considered to be chemically isolated as it evolves. Both of these assumptions limit any model's ability to match the full distribution of chemical elements rather than the average trends and also reproduce the *scatter* seen in the measured stellar abundances. One exception to this is the set of models where supernovae are considered to have individual mixing volumes which can then overlap as they expand (Oey 2003; Karlsson 2005; Leaman 2012; Gómez et al. 2012).

Thus, while these chemical evolution models are flexible and powerful, there are some inherent limitations. The natural solution is to turn to hydrodynamical simulations. Idealized simulations of an UFD-sized galaxy have been constructed to study the effects of radiative cooling, clumpy media and off-centered explosions, effects typically not included in analytic models (Bland-Hawthorn et al. 2015). Such simulations can also be used to test complex explosion scenarios to reproduce specific SFHs and MDFs (Webster et al. 2015, 2016). For cosmological simulations, it unfortunately remains computationally prohibitive to simulate the formation and evolution to $z = 0$ of a UFD around a Milky Way-like galaxy because of the necessarily high resolution. Instead, simulations have focused on isolated dwarf galaxies, finding supernova feedback and UV background radiation (Sawala et al. 2010) as well as the time of reionization (Simpson et al. 2013) are critical for reproducing galaxies with characteristics similar to the Local Group dwarf spheroidals. On the other hand, a larger galaxy population can be simulated at high resolution if only high redshifts are considered. Such work emphasizes the importance of supernova feedback providing turbulent-driven mixing (Ritter et al. 2015), external enrichment for nearby halos (Smith et al. 2015) and providing a metallicity floor for subsequent star formation (Wise et al. 2012b), all typically considered in the context of Population III star formation.

Now, the population of dwarf galaxies is again expanding as the Dark Energy Survey

begins its comprehensive search of the southern sky. Seventeen new ultrafaint dwarf galaxy candidates have been found in the survey's first two years (see Drlica-Wagner et al. 2015, and the references within for a summary of the observations). Since direct searches will remain difficult even with JWST (Okrochkov & Tumlinson 2010) and because the Local Group is thought to be a representative cosmic volume at early times (Boylan-Kolchin et al. 2016), Local Group UFDs will remain as the basis for near-field cosmology to answer fundamental questions about galaxy formation in the early Universe. Their numbers and star formation histories can already provide constraints on when and how reionization proceeded (Bullock et al. 2000; Benson et al. 2002; Busha et al. 2010a); suggest that they were primary sources of chemical enrichment for the intergalactic medium at high redshift (Scannapieco et al. 2002; Salvadori et al. 2014); and place constraints on the potential nature of warm dark matter (Chau et al. 2016). Furthering our understanding of these objects will build a more complete picture of how galaxies formed globally.

In summary, observations suggest that the UFDs have short but complex SFHs and that inhomogenous mixing may play a role in creating the spreads seen in abundance patterns. Some, but not all, of these processes can be captured by analytic chemical enrichment models alone. Thus, this paper examines a high resolution, cosmological simulation of the early Universe to see how star formation, enrichment, and mixing proceed in small dark matter halos at early times in order to inform the use of analytic models and to consider what the observable consequences might be. In Section 3.2, the simulation being analyzed is described in detail. In Section 3.3, we assess the validity of two common assumptions of analytic models using the simulation where they are relaxed. In Section 3.4, we present the star formation histories and metallicity distribution functions of the simulated halos for comparison with the UFDs. Finally, we discuss the implications of these results in the context of the current UFD observations in Section 3.5 and summarize our conclusions in Section 3.6.

3.2 Simulation Basics

3.2.1 Methods

We analyze the cosmological, hydrodynamical simulation of Wise et al. (2012a) (referred to as "RP" in the paper), performed with `enzo`, an Eulerian, adaptive mesh refinement, hydrodynamical code (Bryan et al. 2014). The simulation has a box size of 1 Mpc and a resolution of 256^3 leading to a dark matter particle with $m_{\rm DM} = 1840 M_\odot$. This mass resolution coupled with a maximal spatial resolution of 1 comoving pc enables detailed studies of the formation of the first generation of dwarf galaxies. The simulation was stopped at $z = 7$ to prevent any large-scale modes with $r \approx L_{\rm box}/2$ from entering the non-linear growth regime.

The simulation accounts for both the formation and metal yields of Population II and III (Pop II/III) stars separately. Pop II stars are formed if [Z/H] > -4 and Pop III are formed otherwise. Star particles are formed if the gas has an overdensity of $5 \times 10^5 (\approx 10^3 {\rm cm}^{-3}$ at $z = 10$) and has a converging flow. Pop III stars also have an additional formation requirement that the gas has a molecular hydrogen fraction such that $f_{\rm H_2} > 5 \times 10^{-4}$. Instead of forming star particles with a fixed stellar mass, Pop III particle masses are sampled from an IMF with a functional form of

$$f(\log M) dM = M^{-1.3} \exp\left[-\left(\frac{M_{\rm char}}{M} \right)^{1.6} \right] dM \tag{3.1}$$

where $M_{\rm char} = 100 M_\odot$. Above $M_{\rm char}$, it behaves as a Salpeter IMF but is exponentially cutoff below (Chabrier 2003; Clark et al. 2009).

The supernova feedback is included in the simulation as thermal feedback. The blast wave is modeled by injecting the explosion energy and ejecta mass into a sphere of 10

pc, smoothed at its surface to improve numerical stability (Smith et al. 2011). Because we resolve the blast wave relatively well with several cells across at its initialization, the thermal energy is converted into kinetic energy and agrees with the Sedov-Taylor solution (e.g., Greif et al. 2007). Population III can form two types of supernovae: normal Type II SNe ($11 \leq M_*/M_\odot \leq 20M_\odot$), hypernovae ($20 \leq M_*/M_\odot \leq 40M_\odot$) (Woosley & Weaver 1995), and pair-instability supernovae (PISNe, $140 <= M_*/M_\odot <= 260M_\odot$) (Heger & Woosley 2002). For Type II SNe, an explosion energy of 10^{51} erg is used and a linear fit to the metal ejecta mass calculated in Nomoto et al. (2006):

$$M_{\rm Z}/M_\odot = 0.1077 + 0.3383 \times (M_*/M_\odot - 11) \tag{3.2}$$

Hypernovae are an extension of the Nomoto et al. (2006) model, linearly interpolating results to M_*. For PISNe, the following function is fit to the models of Heger & Woosley (2002):

$$E_{\rm PISN} = 10^{51} \times [5.0 + 1.304(M_{\rm He}/M_\odot - 64)]{\rm erg} \tag{3.3}$$

where $M_{\rm He} = (13/24) \times (M_* - 20)M_\odot$ is the helium core (and equivalently the metal ejecta) mass and M_* is the stellar mass. If the star particle mass is outside of these ranges, then an inert, collissionless black hole particle is created.

Finally, Population II star particles generate 6.8×10^{48} erg s$^{-1} M_\odot^{-1}$ from SNe after living for 4 Myr. The ejected gas has solar metallicity, [Z /H] = 0.02, resulting in a total metal yield of $y = 0.005$.

In addition to this thermal feedback, a unique feature of the simulation is its inclusion of the energy coupling of the radiation field generated by these stars to the gas surrounding them. The radiation field is followed with adaptive ray tracing (Wise & Abel 2011) that is

based on the HEALPix framework (Górski et al. 2005) and is coupled self-consistently to the hydrodynamics. The radiation is modeled with an energy $E_{\rm ph}$ equaling the luminosity-weighted photon energy of the spectrum. Population III stars have a mass-dependent luminosity taken from Schaerer (2002), with $E_{\rm ph} = 29.6$ eV, appropriate for the near-constant 10^5 K surface temperatures of such stars. The number of photons then varies with the different SN types given the mass of the star particle as described above. For Pop II stars, 6000 photons per baryon with $E_{\rm ph} = 21.6$ eV are emitted, appropriate for stars with [Z/H] $= -1.3$.

For more details, we direct the reader to Section 2 of Wise et al. (2012b). The analysis and plots that follow were done with `yt` (Turk et al. 2011).

3.2.2 Dwarf Galaxy Population

Even in the early universe of the simulation, a number of halos form stars and represent a range of dark matter masses, stellar masses, and metallicities. The full population will be discussed throughout. Of the almost 2000 halos at $z = 7$ within the simulation with $\rm M_{halo} > 5 \times 10^5$ $\rm M_\odot$, 24 of them have formed stars by the final snapshot. Their distribution of halo masses, stellar masses, and average metallicities can be found in Figure 3.1. They range from 6.56×10^5 $\rm M_\odot$ - 6.34×10^8 $\rm M_\odot$ in halo mass, 7.47×10^2 $\rm M_\odot$ - 3.69×10^6 $\rm M_\odot$ in stellar mass, and $-2.6 <$ [Z/H] < 0.12 in average metallicity. Star formation proceeds in these halos for a period of roughly 500 Myr where it can no longer be followed as the simulation is terminated because of computational costs.

To place this dwarf population in the context of the observed dwarf galaxies, Figure 3.1 shows the mass-metallicity relation for the simulated halos as well as the observed relation of Kirby et al. (2013). Seven already have $\rm M_{star} > 10^4 M_\odot$, the standard cut off for an "ultrafaint" dwarf classification at lower redshift (Martin et al. 2008). However, when the entire mass range of the observed Local Group dwarfs is considered, the simulated dwarfs

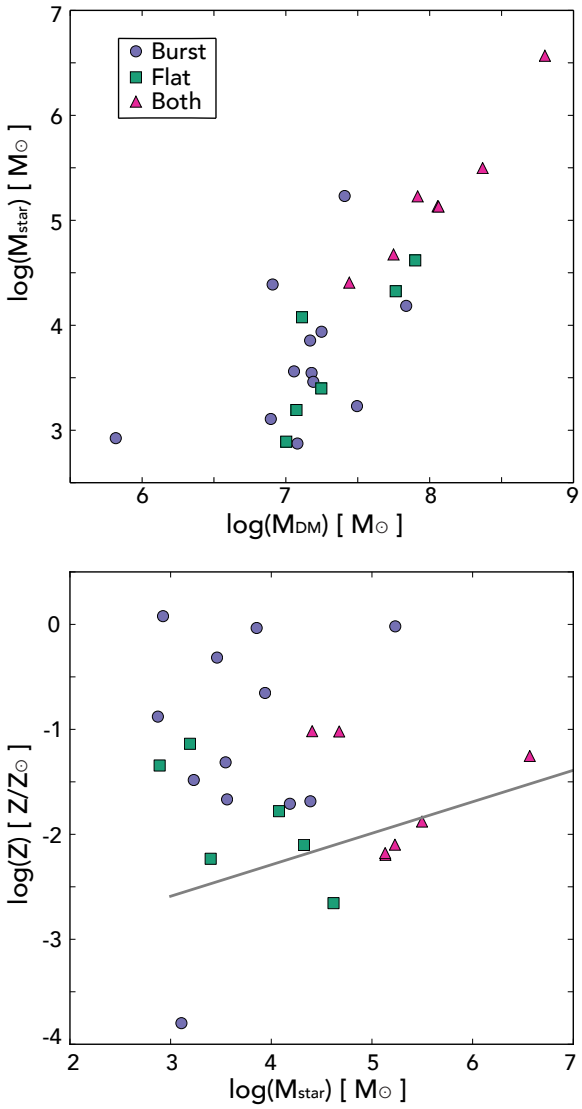

Figure 3.1: Upper panel: Stellar mass as a function of total dark matter halo mass showing the range of halos in the simulation. Lower panel: stellar mass versus average metallicity for the simulated star-forming halos. The labels correspond to SFH types. (see Section 3.4.1) The line corresponds to the observed relation for Local Group dwarf galaxies (Kirby et al. 2013). While the simulated galaxies have roughly the same massed as the observed dwarfs, they are generally too metal rich and there is a much higher scatter in their metallicities.

span roughly the same mass range. Yet the halos within the simulation typically have higher average metallicities than their low-z Local Group counterparts. We consider the implications of this in Section 3.5.

3.3 Physics Revealed by Analytic Model Approximations

Analytic models remain the most flexible and fastest way to evaluate the importance of different baryon processes in the smallest halos at $z = 0$. However, their parameterizations require a number of simplifying assumptions. In this section, we take advantage of the high resolution of the simulation to evaluate the validity of some of these assumptions for the evolution of dwarfs in the early universe.

First, we present a comparison of the simulation with the simplest analytic model, the closed box model, as a way to illustrate the limitations of its assumptions. Next, we look at a common parameterization for supernova wind models in approximating the extent of chemical enrichment and the isolation of star-forming halos in the early universe. Finally, we examine the most common underlying assumption of chemical evolution models, homogeneous mixing, by comparing metallicity trends in the gas and the stars.

3.3.1 Closed Box Model

The simplest model for tracing the metallicity of the gas and stars associated with a dark matter halo is the closed box model. It assumes that there is no flow of gas into or out of the halo and that the gas self-enriches with each star formation event. Furthermore, the amount of metals that is returned to the gas is determined by the assumed yield, the mass of metals formed by a given stellar mass, and the metals are assumed to mix completely and

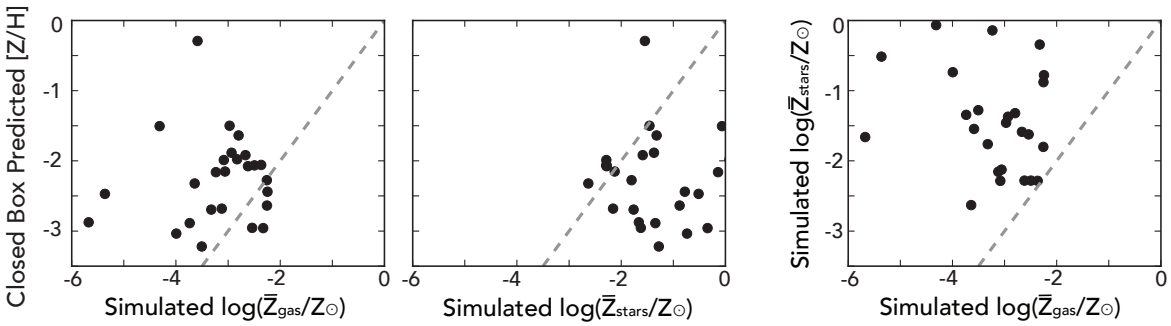

Figure 3.2: Closed box predicted metallicities compared to the average gas metallicities (left) and average stellar metallicities (center) in the simulation at $z = 7$. The dashed line shows where the two quantities would be equal. These plots highlight the discrepancies between the model and the simulation. The average gas metallicities are lower while the corresponding stellar metallicities are higher. Finally, the right panel highlights this mismatch by showing the relation between gas and stars in the simulation.

instantaneously. Within this simple framework, the metallicity is given analytically as:

$$\begin{aligned} Z(t) &= -p \ln\left(\frac{M_{\rm gas}(t)}{M_{\rm gas}(0)}\right) \\ &= -p \ln\left(\frac{M_{\rm gas}(t)}{M_{\rm gas}(t) + M_{\rm stars}(t)}\right) \end{aligned} \tag{3.4}$$

where p is the yield, $M_{\rm gas}(0)$ is the initial gas mass, and $M_{\rm gas}(t)$ and $M_{\rm gas}(t)$ are the current gas and stellar mass respectively.

Deviations from this model in the simulation can then be used to identify processes that are most likely responsible for these differences. In short, how straightforward is the chemical enrichment of dwarf galaxies at early times?

Figure 3.2 shows how the metallicities predicted by this model compare with those seen in the simulation. For each star-forming halo, the final gas and stellar masses at the end of the simulation ($z = 7$) are converted to a predicted metallicity using the above equation and the average gas and stellar metallicities are taken directly from the simulation. The

simulated values are averages of the gas and stars respectively found within the virial radius of each halo at $z = 7$. As seen in the left panel, the simulated gas metallicities are all lower than what is predicted by the model. Introducing a simple offset (for example by changing the yield) would not be enough to reproduce the large scatter seen in the halo metallicities. Furthermore, the closed box model assumes that the average gas and stellar metallicities should be the same but as shown in Figure 3.2, this is clearly not the case in the simulation. The stellar metallicities (center panel) are almost entirely *higher* metallicities than the closed box predictions, in contrast to the gas. The metallicity scatter amongst the halos is large for the stars as well; however, these values do tend to sit closer to the predicted values. Finally, the right panel emphasizes this mismatch between gas and stellar metallicities in the simulation. For a given average gas metallicity, a wide range of average stellar metallicities is seen in the halos. There is no simulated linear relation.

Figure 3.2 begins to emphasize the limitations of such a simplistic chemical evolution model. For example, halos with the lowest gas metallicities ($Z < -4$) have stellar metallicities that are quite high in the simulations. This complex relation between gas and star formation requires a more in-depth study. In the remainder of this section, we examine two key assumptions of the closed box model and evaluate their validity. First, we look at the extent of supernova-driven winds, the ejection of metals from star-forming halos and the chemical isolation of these halos. Then, we examine the role of inhomogeneous mixing in driving the spread in metallicities that are seen within halos themselves.

3.3.2 Supernovae-Driven Winds

Supernovae (SNe) are known to drive winds from galaxies that enrich their surroundings and other nearby halos (Wise et al. 2012b; Smith et al. 2015). This outflow process can be approximated as a pressure-driven spherical shell, expanding with the Hubble flow and into

an IGM with constant density ($\bar{\rho}$) of zero pressure (Tegmark et al. 1993b). In this simple configuration, the radius of the outflow becomes:

$$\ddot{R}_s = \frac{3P_b}{\bar{\rho}R_s} - \frac{3}{R_s}(\dot{R}_s - HR_s)^2 - \Omega_m\frac{H^2R_s}{2} \tag{3.5}$$

where the overdots represent time derivatives and the s and b subscripts indicate shell and bubble quantities respectively. The pressure, P_b, that drives the bubble is provided by the SNe, which have a net input of energy into the system with a rate equal to

$$\dot{E}_b = L(t) - 4\pi R_s^2\dot{R}_sP_b \tag{3.6}$$

Here, $L(t)$ is the luminosity of the SNe and the remaining term is the typical work done by the shell as it expands. Lastly, adiabatic expansion is assumed such that $P_b = E_b/2\pi R_s^3$.

Levels of complexity (such as different forms of cooling, a stochastic star formation rate, dissipative heating etc.) can be added as desired but there are almost always three underlying assumptions to the model: 1) spherical shells; 2) isolation of the given halo; 3) expansion into a constant density IGM. Understanding that many of these assumptions are violated in a cosmological, hierarchical setting, we measure the extent of the metal-enrich material surrounding each of the star-forming halos in the simulation. Using `yt`'s clump-finding algorithm, a metal-rich bubble can be identified by setting a metallicity boundary and a search volume without assuming anything about the shape of the bubble. For our search, we focus on Pop II-driven winds and set a boundary of [Z/H]$= -6$ in Pop II-generated metallicity, such that anything with a lower metallicity is considered un-enriched. The search volume is visually confirmed to be big enough to encompass the bubble associated with each halo. Once the metallicity surface has been identified, the center of the asymmetric contained volume is defined and the average distance of each cell within the volume to the

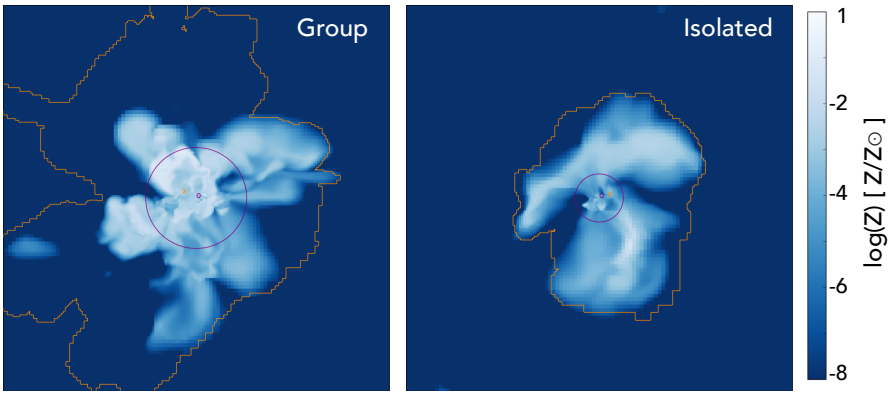

Figure 3.3: Slices through the center of each halo in metallicity with a width of 25 kpc for two different halos at $z = 7$ with the bubble contour identified by `yt` shown in orange. Purple circles represent the virial radii of the halos contained within the simulation slice. The left panel is centered on the most massive halo in the simulation, which is found in a dense, crowded environment. The enrichment bubble surrounding this group of halos is asymmetric and less massive than the semi-analytic model predicts. The right panel shows a more symmetrical bubble for another massive halo in the simulation that is isolated from surrounding halos.

center is computed and designated as the average radius of the clump.

Figure 3.3 shows examples of this bubble finding for two different halos - the most massive halo on the left and an isolated halo on the right. A majority of the star-forming halos in the simulation are in a state similar to the most massive halo; that is, most exist within bubble regions that are asymmetrical and encompass multiple halos. This also implies that most are within a close enough proximity to their neighbors such that the most massive halo in the region has the ability to cross-pollute those surrounding it. We consider these halos as "group" halos in the environment discussion of future sections. Such cross-enrichment both violates the assumptions of the simple analytic model as well as complicates the interpretation of stellar metallicities (discussed further in the following section). Yet there is a fraction of halos that appear to remain chemically isolated from their surroundings and where the analytic model described above should roughly follow the expansion of the model described

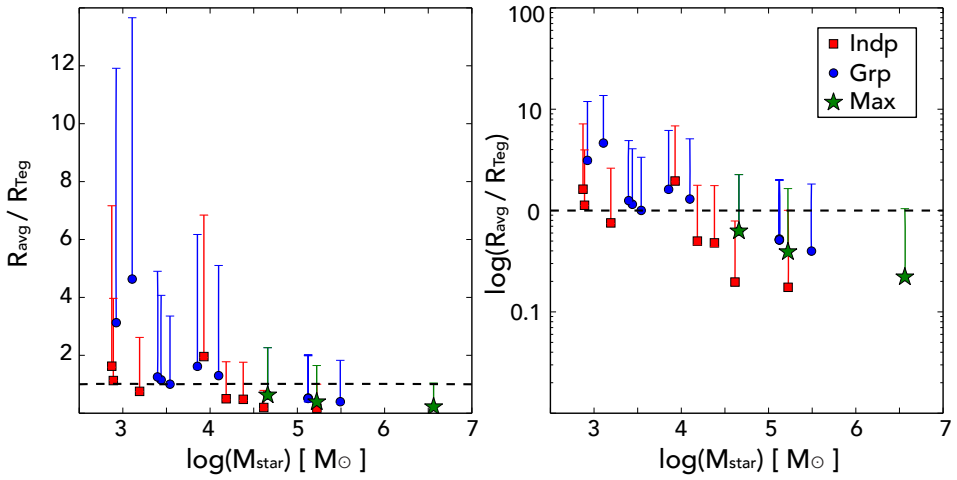

Figure 3.4: Bubble radii predicted by the SAM described in Section 3.3.2 are compared to those measured by the simulation and plotted as a function of halo mass. Because of their asymmetry, the average bubble radii are plotted as points and the error bar corresponds to the maximum bubble radii associated with each star-forming halo in the simulation. Isolated halos are plotted as red squares; those sharing enrichment bubbles are plotted as blue circles; and the most massive group member is in bubble is plotted as a green star. Above a stellar mass of 10^4 $M_\odot$, the model radius is within a factor of two of the simulated radius. At lower masses, there is a larger scatter in the ratio of the radii because the bubbles surrounding group members are dominated by their most massive member. Those halos that are isolated show good agreement between the model and the simulation.

above. This is exemplified in the right panel of Figure 3.3. This isolated halo has a more symmetrical outflow bubble as might be expected. Such halos are referred to as "isolated" in future sections.

To facilitate a comparison of the above model and the full hydrodynamical simulation, we calculate a model-predicted radius for the SN bubble of each halo using the final stellar mass at $z = 7$. The starting time for the bubble integration was chosen to be the time the first star particle of the halo was created.

Figure 3.4 shows how the average bubble radius compares to that predicted by the model as a function of stellar mass. Because the bubbles identified by `yt` are asymmetrical, they have an average radius, plotted as points, and a maximum radius displayed as upper error

bar. In general, as the stellar mass decreases, the ratio of simulated to modeled bubble radius decreases. However, the quantities never differ by more than by a factor of five with the large majority (those with $M_{\rm star} > 10^4 M_{\odot}$) differing by less than a factor of two. This indicates that despite its simplifying assumptions, the analytic model does a remarkably good job at illustrating what the extent of enrichment seen in the simulation.

However, as noted above, the majority of the halos are in groups, violating the isolation assumption of the SAM. To examine the possible consequences, the halos are separated into three categories. Those residing alone in their own enrichment bubble are called "isolated". Those halos that are found in sharing enrichment bubbles are identified as either a group member ("groups") or as the most massive group member ("max").

The most massive halo is expected to drive the strongest wind according to the SAM so for those halos in groups, the most massive should perhaps correspond mostly closely to the model value. Figure 3.4 shows that the best match is indeed for the most massive halos which dominate their local group. Less massive halos sharing a SN bubble with a more massive halo are thus always going to predict smaller radii than what is measured.

Similarly, we might expect better agreement for isolated halos where the isolation assumption holds. In general, the isolated halos show a smaller ratio of modeled and simulated bubble radii than halos of the same mass within groups. This is especially true at the smallest stellar masses where the halos in groups reside in much larger enrichment bubbles than would be expected from their mass alone because of the presence of a nearby, more massive galaxy. Furthermore, as the stellar mass of the halo increases, the ratio of the average simulated bubble radius to the model-predicted radius decreases as the halo driving the enrichment bubble also corresponds to the mass driving the outflows in the model.

Most surprising is the fact that the simple star formation histories at the heart of the analytic wind model reproduce this physical extent of the chemical enrichment bubbles. The

model assumes that a constant fraction of the gas mass is turned into stars which then generate a specific amount of SN energy continuously. Some simulated halos, on the other hand, have huge bursts of star formation which provide a large amount of SNe energy shortly thereafter, unlike the model. The rough agreement in enrichment extent suggests that the details of these SFHs may be less important than the total amount of energy deposited by the SNe. However, these details again become important when considering the metallicity of the gas remaining in the halo and the metallicity of the stars that are then formed.

3.3.3 Inhomogeneous Mixing

In addition to modeling the extent of the SN-driven outflows, chemical evolution models are capable of tracking stellar metallicities and abundances of the smallest halos at the earliest times. In general, however, the models assume homogeneous mixing of the generated metals throughout the halo such that the stars directly track the average metallicity of the gas. However, as Figure 3.3 shows, the gas within these bubbles and even within the virial radius of each halo is *not* homogeneously mixed.

The radiation pressure included in the simulation does drive more turbulent mixing within the interstellar medium of the halos when compared to those without it (Wise et al. 2012a). Yet, metallicity variations still exist in the gas throughout the halo which have consequences for the stars that subsequently form. The right panel of Figure 3.2 suggests that, in the simulation, there is a bias in where the stars are formed such that stars form preferentially in gas that is more metal rich. This is consistent with the picture of star formation occurring in the dense center of halos where a large reservoir of metals remains than in the diffuse, less metal-rich outer parts of the halo.

3.4 Observable Traits of the Simulated Halos

Ultimately what the analytic models above and others like them are trying to do is to reproduce different observable properties of dwarf galaxies in different contexts. The full cosmological, hydrodynamical simulation is a natural extension of these models. Thus, in this section, we study the characteristics of the simulated halos most easily derived from the primary observations - the star formation histories and the metallicity distribution functions - discussing their general trends and comparing them with the current observations.

3.4.1 Star Formation Histories

By nature of the cosmological simulation, every halo is fairly unique in terms of when and how the stars are formed. Within the simulation, there are 24 halos that have formed stars by the final redshift ($z = 7$), so a manual inspection of each is possible.

Figure 3.5 shows three representative SFHs. For each panel, the solid and dashed orange lines represent the average and median gas metallicity within the virial radius at that time step respectively with the shading indicating the range encompassed by the 25th and 75th percentiles. Overplotted are the individual star particles bound in the halo at the final time step. Purple points represent star particles that were created in-situ within the most massive progenitor while teal points represent star particles that were created within and subsequently accreted from a less-massive progenitor. The points are plotted at the particles' creation times and not when they were accreted into the most massive progenitor.

Clearly, different processes are dominant in these three halos. The left panel shows a halo that closely resembles the chemical history as represented by a typical analytic model described above and in most chemical evolution models that scale SF with halo mass. The halo experiences smooth and steady star formation, with all of its stars being formed inside

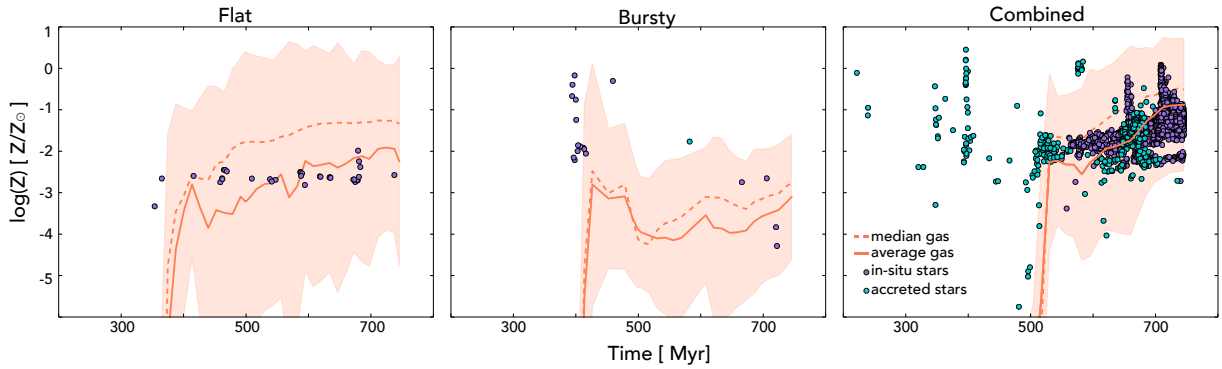

Figure 3.5: tar formation histories of three representative halos are shown. The solid and dashed orange lines represent the average and median gas metallicity within the virial radius at that time step respectively, with the shading indicating the range encompassed by the 25th and 75th percentiles. Overplotted are the individual star particles bound in the halo at the final time step. Purple points represent star particles that were created in-situ within the most massive progenitor while teal particles represent those star particles that were created within and subsequently accreted from a less-massive progenitor. All star-forming halos in the simulation can placed into one of the three categories: 1) Flat: a continuous SFH with flat chemical evolution; 2) Bursty: a single burst of SF with a large spread in metallicity dominates the SFH; 3) Combined: the SFH shows both continuous and bursty features.

the most massive progenitor. The stars all have roughly the same metallicity within 1 dex and similar metallicity to the median of the gas. Both the gas and stars show an increase in metallicity with time as the halo self-enriches. Furthermore, the gas possesses a wide range in metallicity but the stars are all formed with roughly the average metallicity of the gas, indicating that they are forming from gas that is well-mixed.

Conversely, the center panel shows a halo with an entirely different SFH. The halo experiences a strong, early burst of star formation with minimal star formation afterwards. The fact that the gas metallicity rises after a burst of high metallicity star formation is likely just an effect of the gas information being limited to specific time step outputs while the stars are tagged with their precise creation time in the simulation. The gas and stellar metallicities actually *decrease* with time as the halo accretes fresh gas from its surroundings. Assuming the same type of enrichment patterns for this halo as the one above is not physically

valid. With the stars forming in such a short period of time, inhomogeneous mixing must be responsible for the spread in stellar metallicities.

Finally, the right panel shows the most massive halo which has the most complex SFH. There is clearly a trend of self enrichment after a certain time with the stars generally following the average metallicity of the gas. However, even within this self-enrichment, the stars clearly form with an observable width of metallicity. In addition, there are significant bursts of star formation that happen at multiple points even in this short time span. Finally, this halo has a large number of accreted stars when compared to others in the simulation, but with a stellar mass of 3.69×10^6 $M_\odot$, this halo is already larger than the present-day UFD mass cut-off and with the simulation ending at $z = 7$, it is hard to know if it will remain a dwarf galaxy or merge into a larger system by $z = 0$.

Looking at the SFH of each individual halo, it is possible to place each halo into one of the three categories illustrated in Figure 3.5: "flat", "bursty", and "combined." At $z = 7$ within this simulation, there are 6 flat halos, 12 bursty halos, and 7 combined halos. The differences in both how the stars are formed and with what spread in metallicity are directly relevant to informing the underlying models of most chemical evolution calculations. Can we link these differences in SFH to processes or parameters that are typically included in such models? In what follows, we examine three of the most straightforward explanations - halo mass, mergers, and environment.

3.4.1.1 Halo Mass

One potential explanation for these differences in SFH would be their halo mass, their stellar mass or both. Lower mass halos may be more prone to bursting since a single outside event may have a larger impact on the halo as a whole, whether a strong accretion period, being overcome by an outside SN-driven wind, or a large merger event. Such a mass dependence

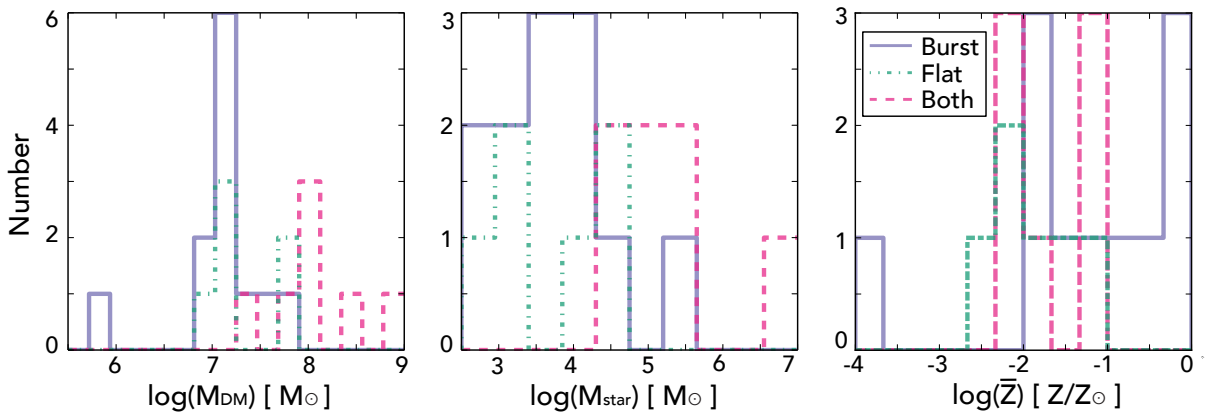

Figure 3.6: Halo mass, stellar mass, and average stellar metallicity distributions for the halos within each of the three SFH classifications. Those with combined SFHs are most likely to be found in the most massive halos. However, there is no way to predict whether a halo will be bursty or flat for the average and low mass halos or by looking at the average stellar metallicity.

would also be the easiest to include in future chemical evolution models so it's the first thing considered.

Figure 3.6 shows the distribution of halo masses, stellar masses, and average stellar metallicity for the halos within each of the three SFH classifications. Those halos with combined SFHs are typically the largest in both halo and stellar mass within the simulation. They do not, however, show any differences in average metallicity since the gradual self-enrichment and larger number of star particles deemphasizes the importance of single bursts of star formation.

Yet halos categorized as bursty or flat span the entire range of halo and stellar masses as well as the range of average stellar metallicities. It was only by including the time axis from the simulation that these two subsets are distinguishable and resolving the short time scale considered ($\approx$ 400 Myr) is not within range of recent or upcoming observations. Instead, we now consider how the chemical environments of these halos could affect their SFHs.

3.4.1.2 Mergers

Mergers have the ability to both trigger star formation and bring in gas and stellar populations that have evolved in a separate environment. In the context of these star formation histories, these outside halos can potentially increase the spread in metallicity for forming stars and make interpreting the spread in observed MDFs less straightforward.

In general, because of the short time period considered in the simulation, each halo has at most a few mergers such that the main halo and its infalling satellite have a mass ratio of $M_{sat}/M_{main} > 0.3$. Many happen early enough that they are potentially only bringing in gas and not stars. One exception to this is the most massive halo, show in the right pane of Figure 3.5. Clearly, mergers have brought in a large number of stars to the final halo. However, the spread in the metallicity distribution function has not been impacted. The accreted stars fall in the same metallicity range as the stars created in-situ. We conclude that mergers are unlikely to have a large effect on the MDF at this early time though they can have an impact on the shape of the SFHs.

3.4.1.3 Environment

Finally, we consider the chemical environment of each of these halos and how it potentially relates to their given SFH. As discussed in Section **??**, even within a box of length 1 Mpc, halos at this early time sit in different chemical environments. The majority of the halos are within enrichment bubbles containing more than one member and the groups are of different physical sizes and masses. Halos in such an enrichment bubble are referred to as "group" halos below, while the most massive group member is counted as a "max" halo. Meanwhile, there are also halos which are chemically isolated from their surrounding environment, referred to as "isolated" below.

Table 3.1: Distribution of Halos by SFH Type and Chemical Environment

	MAX	GROUP	ISOLATED
COMBINED	3	2	0
BURSTY	2	6	3
FLAT	0	3	2

Table 3.1 shows how the halos are distributed for a given SFH and chemical environment, in keeping with the nomenclature used above. As discussed, the most massive group members, typically the more massive halos in the simulation, typically have combined SFHs. As expected, these halos are also more often found in dense environments so none of the isolated halos fall into this SFH category.

For those halos in groups but not the most massive member, it is plausible that a SN-driven wind could come over the halo and trigger a burst of SF with a spread in metallicity. When these group halos are considered, they are two times more likely to be bursty than flat implying that the over-dense environment has a preference for one SFH over the other. However, of the few isolated cases that exist, they are equally likely to be either bursty or flat. Something more than just an individual, external event is triggering SF bursts in the simulation.

Thus, another physical process is needed to explain why star formation does not proceed similarly in these small halos at early times. It must happen in the early formation of these halos and on a short time scale to produce the differences in star formation that arise over ≈ 400 Myr. Perhaps the solution is colliding SN blast waves as suggested by Webster et al. (2016) or perhaps the stochastic nature of the mixing simply drives the form of the star formation. An exact solution to this issue is reserved for future work. For now, we point out that these two properties, mass and environment, would have been simple criteria for implementing different SFHs in chemical evolution models so perhaps a more complicated

method may need to be included in the future.

3.4.2 Metallicity Distribution Functions

One way to get a sense of how star formation proceeded throughout a given galaxy is to look at the metallicity distribution function. This is particularly true for dwarf galaxies that have low average metallicities, corresponding to short histories such that the metallicity spreads are created by at most a few episodes of star formation. In this section, we explore the characteristics and trends of the MDFs of the simulated halos and examine if they can be used to differentiate between different SFHs.

The MDFs of the star forming halos do show spreads in metallicities, as expected from observations of Local Group UFDs. However, the average and shape of these distributions can vary substantially so that discussing the mean and standard deviation of these distributions is not meaningful. Instead, we present the MDF of each halo, grouped by their SFH category and discuss the trends seen within. For some of the halos, their stellar masses are so low that they have only one or two star particles in total but these are easily identified by their peaked, abnormal distributions.

For Figures 3.7-3.9, the distribution of star particles' metallicities weighted by the mass of the star particles are shown for a given halo, grouped by their respective SFH type. The shaded regions correspond to the metallicity range of the MDFs shown in Figure 3 of Brown et al. (2014) of 6 UFDs.

The MDFs of the halos are diverse - wide and narrow distributions, skewed low and high. However, this diversity is the same across the three different SFH categories. That is, one characteristic cannot be linked to a specific SFH type. In this way, the MDFs cannot be used to distinguish SFH among the data or to link MDFs with SFHs in analytic models.

However, there are a few trends that highlight the chemical properties of the simulated

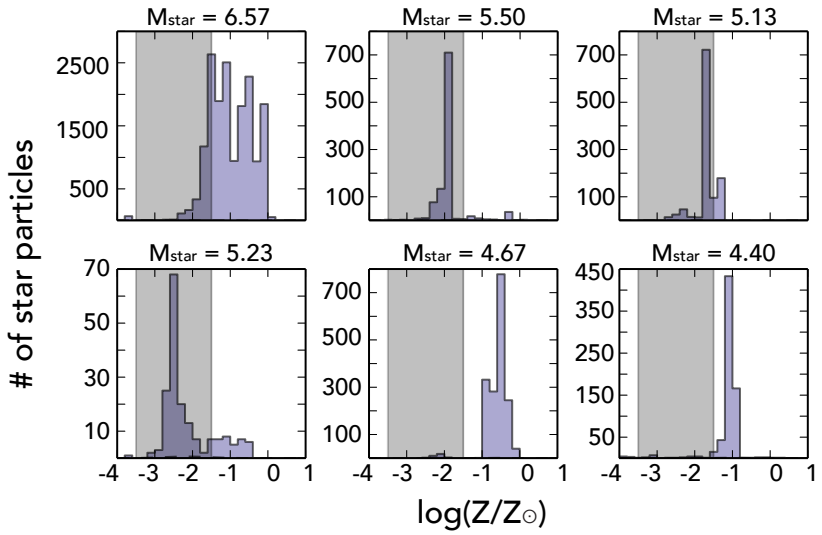

Figure 3.7: Distribution of star particles' metallicities weighted by the stellar mass of each particle for a given halo categorized as "combined." The shaded region indicates the range of data presented for 6 UFDs in Brown et al. (2014). The halos are organized left to right in order of increasing halo mass with the log of the stellar mass in units of solar masses printed.

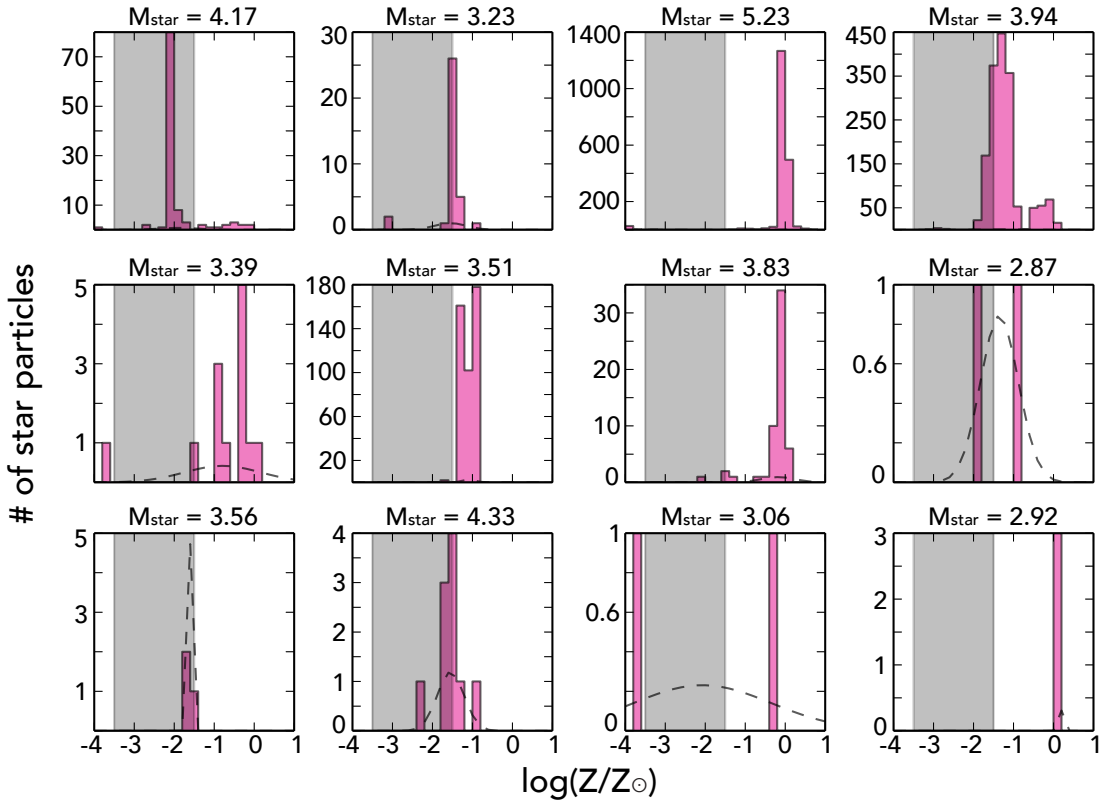

Figure 3.8: Same as Figure 3.7 except showing the MDFs of the "bursty" halos.

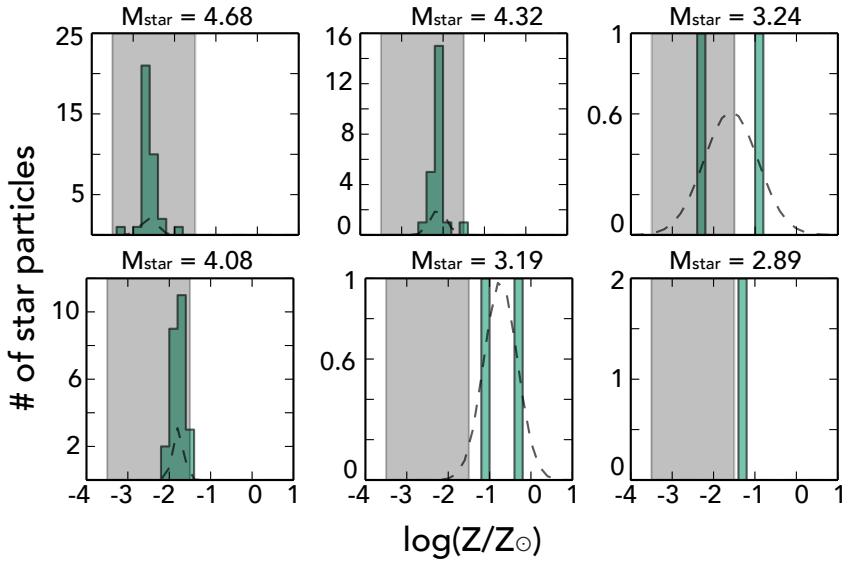

Figure 3.9: Same as Figure 3.7 except showing the MDFs of the "flat" halos.

halos. In general, the galaxies are metal-rich compared to the observed UFDs. For a majority of the halos, the bulk of the stars have metallicities that are above the range of observed UFD stars. As also displayed in Figure 3.6, the average metallicities of these halos are approximately [Z/H]$= -1$, with some stars reaching solar metallicities and above. These high metallicities are unrealistic; all of the halos sit above the defined mass-metallicity relationship at low redshift (Kirby et al. 2013) (see Figure 3.1).

In addition to high average metallicities, the simulated halos are also more strongly peaked than the observations. In the observed UFD MDFs, stars are spread over two dex with shallow peaks. In the simulation, the [Z/H] spreads are more typically 1 dex wide and the peaks are much higher. Despite multiple forms of SFHs, the MDFs still show a similar narrowness in their distributions.

3.5 Discussion of the Observational Context for the Simulated Halos

With the more observational properties of the simulated halos now presented, how do they actually compare to the observations despite their limitations?

As discussed in the introduction, CMD observations of UFDs can currently be interpreted as being created by either bursts of star formation (Brown et al. 2014) or through continuous star formation (Webster et al. 2015). In the simulation, we see both forms of star formation occur in a very short period of time. Currently, the resolution of CMD isochrone fitting for these ancient, low-metallicity populations is only accurate within 1 Gyr when age, metallicity and oxygen abundance are allowed to vary, making it impossible to distinguish these two scenarios with the observations(VandenBerg et al. 2015). Similarly, the three SFH categories do not show strong differences in their MDFs, similar to the observations.

The simulated MDFs, on the other hand, do not show obvious agreement with observed MDFs of the UFDs. In addition to being too metal rich and having distributions that are too peaked as discussed above, the halos in general do not have a spread in metallicities as wide as what is observed. In fact, 8 of the halos do not have stars with metallicities below -1.5, the upper limit of the observations in Brown et al. (2014).

Some of these discrepancies may arise because of the limitations of the simulation. Even with such high resolution, issues pertaining to the feedback can persist. In particular, this simulation with the radiation pressure from SNe included has been shown to eject metals further into the intergalactic medium, perhaps better enabling both cross-enrichment and the re-accretion of more highly-enriched material. However, the radiation pressure is also capable of self-regulating star formation and preventing overcooling from forming even more metal-rich stars in the simulation (Wise et al. 2012a). Furthermore, when used as a characteristic galaxy sample, the simulation can also reproduce reionization properties consistent with recent Planck and Lyman-α forest results (Wise et al. 2014a). These results all indicate that implementing feedback remains challenging for future and ongoing work.

In addition to the feedback, the mismatch between the simulations and that data may be also be a result of the fact that stars in the simulation are formed as single particles that represent entire stellar populations. Figure 3.10 shows how the fraction of star particles with [Fe/H] < -1.5 varies as a function of the number of star particles in each halo. Point shapes correspond to the enrichment environment of each halo (see Section 3.3.2) and colors correspond to the type of SFH (see Section 3.4.1). The low yet still limited mass resolution of the simulation means that some of the smallest halos have only 2 star particles within their virial radius. Such small numbers make it hard to produce an MDF with a reasonable width. However, as the stellar mass and number of star particles increase, the fraction of low-metallicity stars also increases. Once again, the most massive halo is an exception. It's

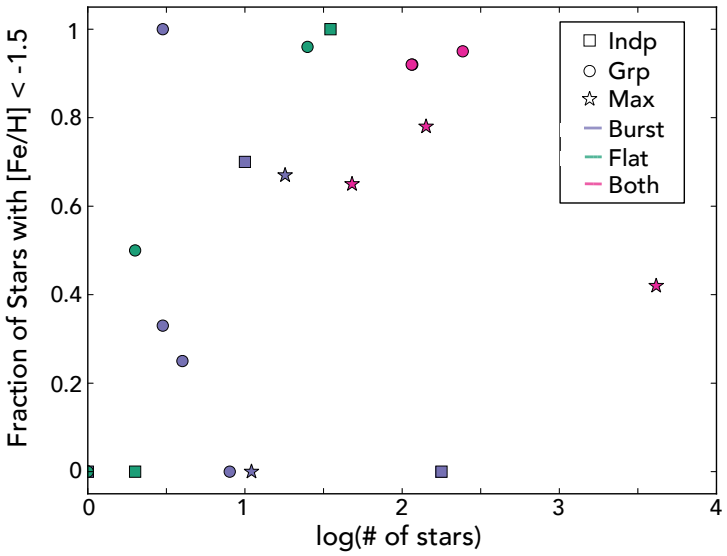

Figure 3.10: Fraction of stars with [Fe/H] < -1.5 as a function of the number of stars in each halo at $z = 7$. [Fe/H] $= -1.5$ was chosen because it is the upper limits of the data in Brown et al. (2014). Point shapes correspond to the enrichment environment of each halo (see Section 3.3.2) and colors correspond to the type of SFH (see Section 3.4.1). The lowest stellar mass halos in the simulation have the smallest number of star particles in the simulation, sometimes as few as 2 particles. These small numbers make it difficult to reproduce a true spread in a MDF. In general, as the halo mass increases, the population of low-metallicity stars also increases.

active SFH means that it has formed a population of high-metallicity stars that dominates in number over the lower-metallicity component.

Furthermore, these results suggest that UFDs may have formed in a more isolated environment than what is sampled here, where cross-enrichment sometimes triggers Pop II star formation without ever having formed Pop III stars (Wise et al. 2012b; Smith et al. 2015). Dark matter only simulations suggest that satellite progenitor halos will form on the outskirts of regions hosting an eventual Milky Way-like galaxy (Corlies et al. 2013). A series of simulations and continuing their run to the present day will allow us to better understand the importance of environment in the evolution of the dwarf satellite galaxy population.

What also remains unclear is how the inclusion of the α elements may help in distinguishing the SFHs as they have done with the observations (Webster et al. 2015). The time scales of the SF bursts could have potentially different signatures than a more slow, self-enriching process. Calculating the abundances can be done by either directly tracing them in the simulation or by linking the metallicity and SF information to a chemical evolution model but both strategies are the subject of future work.

3.6 Summary and Conclusions

The Local Group dwarf galaxies are thought to be the potential building blocks of galaxies like our own and objects that can be representative of the early universe for near-field cosmology. Understanding the formation and evolution of these objects will have implications for reionization, the early chemical enrichment of the intergalactic medium, the composition of the Milky Way's stellar halo, and dwarf galaxy formation in general. Advancements in both simulations and observations can now begin to work together to unlock the star formation histories and chemical environments of these galaxies.

In this paper, we set out to examine some of the basic assumptions of most chemical evolution models by comparing them to a state-of-the-art, high-resolution, cosmological, hydrodynamical simulation. We then in turn compare the early star formation in low-mass halos to the observational properties of Local Group ultrafaint dwarf galaxies.

Our main conclusions are as follows:

1. The semi-analytic model of supernova-driven winds considered here is in good agreement with the extent of chemical enrichment from galaxies in the simulation except at the lowest stellar masses.

2. Inhomogeneous mixing plays a large role in setting the spread in metallicity seen in the star particles. Assuming that the average gas metallicity and average stellar metallicities will be the same is not a good assumption for chemical evolution models.

3. The star formation histories of galaxies in the simulation agree with both models considered in previous data analysis; some are continuous while others are bursty. These histories are not driven by either the halo mass or chemical environment and appear to be a natural, stochastic consequence of the hydrodynamics.

4. In general, the metallicity distribution functions in the simulations are too metal-rich and too peaked such that no obvious direct match can be found in the UFDs. Abundance patterns may remain as a way to distinguish potential SFHs as seen in the simulation but elements are not yet traced in this simulation.

5. The simulation generically forms small galaxies that have both complex star formation histories and spreads in the metallicity distribution functions in a few Myrs in the early Universe. It also hints at the idea that the UFDs might have formed not just early on

but in a more isolated environment than simulated here to explain the spreads at low metallicities.

In the near future, the Dark Energy Survey will mostly likely continue to find new dwarf galaxies and spectroscopic follow-ups of these candidates will provide further constraints on metallicity distribution functions and chemical abundances. Complementarily, the James Webb Space Telescope is primed to directly detect a fraction of these small galaxies at high redshift. Yet reconstructing the star formation histories of these galaxies will remain difficult.

Simulations, on the other hand, can be improved in light of the observations and expanded to produce more observables. In particular, computing individual abundances instead of tracking a global metallicity field will allow us to expand our comparisons of the simulation to include α and neutron-capture elements. In the mean time, it remains possible to pair the star formation histories in the simulation to chemical evolution models to calculate the expected abundances. Such theoretical advancements will potentially enable us to better interpret the observations as they stand today.

Chapter 4

Empirically Constrained Predictions for Metal-Line Emission from the Circumgalactic Medium

4.1 Introduction

Perhaps the most basic process of galaxy formation, the flow of gas into and out of a galaxy, remains as one of the least understood. The key seems to lie in our lack of understanding of the circumgalactic medium (CGM). Roughly defined as the gas surrounding galaxies at 10 to 300 kpc, the CGM encompasses all gas in transition: gas falling onto the galaxy for the first time; gas that is being driven out by multiple feedback processes; gas that is being stripped from infalling satellite galaxies; and gas that is currently being recycled by the galaxy (see Putman et al. 2012, for review).

The structure of this gas halo depends on the mass and redshift of the galaxy in question.

This section contains text from an article accepted by the Astrophysical Journal with publication pending.

Currently, gas is thought to be accreted through two main modes - a "hot" mode where the gas is shock heated as it enters the halo and a "cold" mode where the gas remains in unshocked filamentary structures that can potentially penetrate all the way to the disk (Kereš et al. 2005; Fumagalli et al. 2011). Milky Way-like galaxies are thought to transition from the cold mode to the hot mode by the present day but the details of this transition are neither theoretically agreed upon nor well constrained observationally (Brooks et al. 2009; Joung et al. 2012; Nelson et al. 2015a).

In addition to these inflows, the outflow of gas from the galaxy is equally important in shaping the CGM (Nelson et al. 2015b; Marasco et al. 2015; Suresh et al. 2015a). Stellar feedback of some form is clearly needed to prevent the overcooling of gas and the formation of unrealistic stellar bulges in simulations (Agertz et al. 2011; Brook et al. 2011; Hummels & Bryan 2012). It is also the most effective way of enriching the IGM to the non-pristine levels that are observed (Oppenheimer & Davé 2008; Wiersma et al. 2010; Barai et al. 2013; Ford et al. 2013). While such outflows are regularly seen, the exact physical process driving them and the extent of their influence are uncertain (Turner et al. 2015). Multiple preferred forms of Type II supernova (SN) feedback are implemented and recent work has begun to implement more detailed processes such as radiation pressure from supernovae (Hopkins et al. 2012; Agertz et al. 2013; Ceverino et al. 2014; Trujillo-Gomez et al. 2015), cosmic rays (Booth et al. 2013; Salem & Bryan 2014; Salem et al. 2014), active galactic nuclei (AGN; Sijacki et al. 2007; Booth & Schaye 2009), and direct modeling of a kinetic energy component (Simpson et al. 2015) to name a few. In short, putting constraints on these various models is fundamental to furthering our understanding of galaxy formation.

In general, cosmological galaxy simulations are tuned to reproduce global and primarily *stellar* properties of galaxies such as the stellar mass function and the star formation rate (SFR) density function (Davé et al. 2011; Schaye et al. 2015; Nelson et al. 2015b). Another

benchmark is the creation of thin, extended stellar disks (Governato et al. 2007). The HI mass function is a constraining gas property but again looks at the total mass and not its distribution throughout the galaxy. (Davé et al. 2013) Recently, theoretical work has begun to compare the simulated CGM to column densities and equivalent width measurements as a function of impact parameter from the center of the galaxy (Hummels et al. 2013; Ford et al. 2015; Liang et al. 2015; Oppenheimer et al. 2016). The majority of the simulations have difficulty in matching the large amount and high covering fraction of OVI measurements, tracing the hottest gas phase (except recently for high-mass galaxies (Suresh et al. 2015b) and with cosmic ray feedback (Salem et al. 2015)). Their success varies when looking at cooler, less ionized lines (MgII, CIII, SiIV etc.) but in general, the data reveal large amounts of metal-enriched gas at large impact parameters that is hard to reproduce theoretically. In this way, measurements of the CGM can put strong restrictions on feedback models, independent of the global properties that are already used.

The most successful method of observing the CGM is in the absorption lines of quasar spectra. At higher redshifts, Lyman α and the ultraviolet metal lines of interest have shifted into the optical, making observations easier and successful (Steidel et al. 2010; Simcoe et al. 2004). At low redshift, several studies have begun pushing our knowledge of the more local CGM with measurements of MgII (Chen et al. 2010) and OVI for a number of galaxies (Prochaska et al. 2011; Thom & Chen 2008). The recent installation of the Cosmic Origins Spectrograph (COS) on HST has enabled a new survey of the CGM of low-redshift ($z \approx 0.2$), massive, isolated galaxies. The COS Halos survey has provided a large, uniformly measured sample of the HI column densities (Tumlinson et al. 2013b), metal-line absorption (Werk et al. 2013), and OVI column densities (Tumlinson et al. 2011). As accretion and outflows are expected to vary with redshift in addition to mass, low-redshift studies such as these are crucial as is the need to push to even lower redshifts.

A complementary approach is to observe the CGM *directly* in emission. Quasar spectra will always be limited by the small number of sightlines through each galaxy. An emission map has the potential to provide insight into the physical state of an entire galaxy halo. While promising, the low density of the gas has made this observation challenging. The most success has come from high-redshift surveys for Lyman α emitters (e.g. Bridge et al. 2013; Gawiser et al. 2007) and the more extended Lyman α blobs/halos (e.g. Matsuda et al. 2011; Steidel et al. 2011, 2000) but metal-line emission has remained elusive (Arrigoni Battaia et al. 2015). Recently, the development of new integral field units, MUSE and CWI (and its successor KCWI), now allows for a study of the kinematics of the gas. Early work has already suggested that the absorbers can be linked to global outflows (Swinbank et al. 2015) as well as filamentary inflows (Martin et al. 2014). At low redshift, the upcoming FIREBall-2 is building on its predecessor (Milliard et al. 2010) and pushing the boundaries of low surface brightness UV observations. This, in addition to any small or large near-future UV space telescope mean that direct UV observations of the CGM are closer than ever.

With these advancements in mind, this work looks to take advantage of new data while preparing for future observations. We take a high-resolution, cosmological, hydrodynamical simulation of a Milky Way-like galaxy and compare it to recent column density data. We then ask what emission we could presume to detect with upcoming facilities.

Previous studies of this same simulation provide a solid foundation for this work. Fernández et al. (2012) demonstrated that infalling satellites provide much of the cold, high-metallicity gas found in the halo at $z = 0$ whereas Joung et al. (2012) quantified how much gas of a given temperature is accreted at low z. This existing physical insight allows us to better understand the evolution of the CGM and the contribution of different accretion modes.

In this paper, we look to build on this work when interpreting our emission predictions. In Section 4.2, basics of the simulation used and the photoionization model are summarized.

In Section 4.3, the simulation is compared to column density observations to put empirical constraints on the interpretation of the simulation. In Section 4.4, the emission signatures of this gas and how they evolve are examined and its observational properties are explored. Finally, the broader context of the work is discussed in Section 4.5, and the results are summarized in Section 4.6. Appendix 4.A provides additional information about the EUVB in general and Appendix 4.B examines the effects of simulation resolution on our conclusions.

4.2 Methodology

4.2.1 Simulation Basics

We analyze the cosmological, hydrodynamical simulation of Joung et al. (2012) performed with `enzo`, an Eulerian, adaptive mesh refinement, hydrodynamical code (Bryan et al. 2014). A Milky Way-like halo was identified from within an initial low-resolution run with a periodic box of $L = 25\ h^{-1}$ Mpc comoving on a side with cosmological parameters consistent with WMAP5. This galaxy was centered in a box of length $\approx 5\ h^{-1}$ Mpc which was then resimulated with 10 levels of refinement. The selected galaxy has a final halo mass of $1.4 \times 10^{12} M_{\odot}$ and contains over 8.2 million dark matter particles within its virial radius, with $m_{\rm DM} = 1.7 \times 10^{5} M_{\odot}$. The final stellar mass is $1.9 \times 10^{11} M_{\odot}$, placing the halo above the $\mathrm{M}_{(star)}$-$\mathrm{M}_{(halo)}$ relation as is common with simulations of this type (Guo et al. 2010). The maximum spatial resolution stays at 136-272 pc comoving or better at all times.

The simulation includes metallicity-dependent cooling, a metagalactic UV background, shielding of UV radiation by neutral hydrogen, and a diffuse form of photoelectric heating. The code simultaneously solves a complex chemical network involving multiple species (e.g. HI, HII, H_2, HeI, HeII, HeIII, e^-) and metal densities explicitly.

Star formation and stellar feedback are included in the simulation. Star particles have

a minimum initial mass of $m_* = 1.0 \times 10^5 M_\odot$ and are created if $\rho > \rho_{\rm SF}$ and with a violation of the Truelove criterion. SN feedback is modeled following Cen et al. (2005), with the fraction of the stellar rest-mass energy returned to the gas as thermal energy, $e_{\rm SN} = 10^{-5}$, consistent with the Chabrier (2003) initial mass function. The metal yield from stars, assumed to be 0.025, represents metal production from supernovae of both Type Ia and Type II. This metallicity is traced as a single field and abundances are generated throughout the paper assuming the solar abundance. Feedback energy and ejected metals are distributed into 27 local cells centered at the star particle in question, weighted by the specific volume of the cell. The metals and thermal energy are released gradually, following the form $f(t, t_i, t_*) = (1/t_*)[(t - t_i)/t_*] \exp[-(t - t_i)/t_*]$, where t_i is the formation time of a given star particle, and $t_* = \max(t_{\rm dyn},\ 3 \times 10^6 {\rm yr})$ where $t_{\rm dyn} = \sqrt{3\pi/(32G\rho_{\rm tot})}$ is the dynamical time of the gas from which the star particle formed. The metal enrichment inside galaxies and in the IGM is followed self-consistently in a spatially resolved fashion. For details of these prescriptions, we direct the reader to Joung et al. (2012).

4.2.2 Ionization Modeling

To calculate the relevant ionization processes of interest, the simulation was post-processed with the photoionization code CLOUDY (version 10.0, last described in Ferland et al. 1998) in conjunction with the cooling map generation code ROCO (Smith et al. 2008) and the simulation analysis suite `yt` (Turk et al. 2011). For each model discussed in the upcoming sections, the following procedure was used to produce the column density and emission predictions.

First, CLOUDY look-up tables of ion fractions and emissivity were constructed for a given ionization background as a function of temperature ($10^3 < T < 10^8,\ \Delta \log_{10} T = 0.1$) and hydrogen number density ($10^{-6} < n_{\rm H} < 10^2,\ \Delta \log_{10} n_{\rm H} = 0.5$). Each table assumes

solar metallicity and abundances. The grid is then interpolated for every cell to the correct temperature and $n_{\rm H}$. Then, n_{Xi}, the number density of given ionization state of element X (CIII, SiIV, OVI, etc.) is calculated as:

$$n_{Xi} = n_{\rm H}(n_X/n_{\rm H})(n_{Xi}/n_X) \tag{4.1}$$

where $(n_X/n_{\rm H})$ is the elemental abundance relative to hydrogen and (n_{Xi}/n_X) is the ion fraction computed by CLOUDY. Here the elemental abundance is given as the solar abundance scaled by the metallicity reported in the simulation. The emissivity is more straightforward as CLOUDY directly reports the emissivity at a given temperature and density that is then again scaled by the metallicity.

With these number densities and emissivities, producing the corresponding column density and surface brightness values is done as projections through the simulation with `yt`. Throughout the paper, we assume a box that is 320 kpc across and 500 kpc deep, ensuring the selection of gas associated with the galaxy. Each projection and radial profile is made with a resolution of 1 physical kpc, unless otherwise stated.

Finally, throughout the paper, the assumed ionization field, the extragalactic ultraviolet background (EUVB), is varied to examine the agreement of the simulation predictions with the column density measurements. To this end, we take the 2005 updated version of the Haardt & Madau (2001) background of CLOUDY and split it into its two components - quasars and galaxies. Then, the intensity of each component can be varied and the changes in the predicted column densities studied. The quasar component dominates at short wavelengths and is responsible for the majority of the ionizing radiation in the calculations. In this way, varying the quasar component has more significant consequences than varying the galactic component. A more detailed discussion of the differences among these backgrounds is found

in Appendix 4.A.

Because this is a post-processing of the simulation, this technique is not fully self-consistent. It does not capture the underlying effects on the temperature and density that arise from changing the ionization background used in computing the cooling of the gas. However, the overall galaxy evolution and supernova feedback are thought to dominate the evolution of the gas density, temperature and metallicity more than the choice of EUVB and the ion fractions of interest here are less important in determining these large-scale properties. These limitations remain as part of the uncertainty in the following calculations but the overall conclusions should be robust.

However, the response of the simulation to the changes in the EUVB reflects the field's true influence on the ionization state of the simulated gas, assuming ionization equilibrium. The field is a fundamental property of the physics of the calculation used in calculating the ion fractions and emissivity in CLOUDY. The density and temperature of the gas are not expected to vary much with the choice of EUVB, as discussed in Appendix 4.A.

4.3 Absorption

In this section, we look to place the simulation in the context of a set of current absorption-line observations. First, column density maps of a series of ions are generated and the resulting CGM structure is analyzed. Next, the reliability of the simulation is tested by examining its agreement with available observations, specifically the COS Halos survey (Werk et al. 2013).

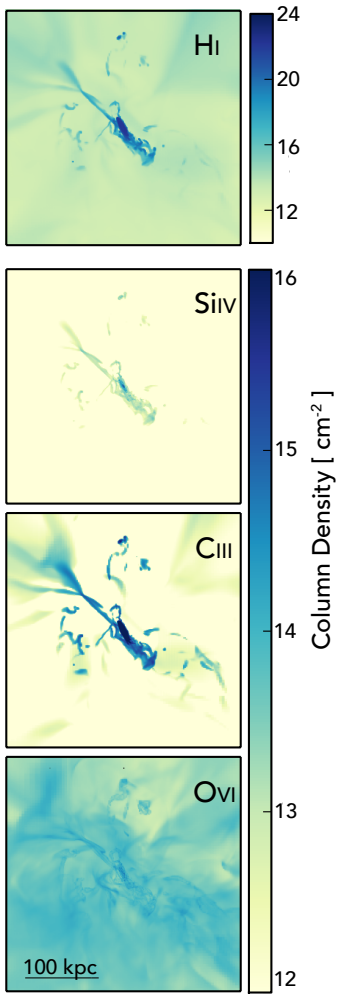

Figure 4.1: Column density maps of HI, SiIV, CIII, and OVI respectively at $z = 0.2$ with a resolution of 1 kpc. Note HI has a unique color bar. OVI has the largest covering factor with moderately high column densities extending uniformly over 100 kpc. CIII has a smaller covering factor but reaches higher densities in visible filaments and stripped satellite material. SiIV is the weakest as its peak ionization temperature is slightly below the typical temperature of the halo gas.

4.3.1 Column Density Maps

In order to better visualize the CGM column density distribution of the simulated galaxy, we first examine Figure 4.1, which shows column density maps for four ions at $z = 0.2$ with

a resolution of 1 kpc. This set of ions allows us to probe from the coldest gas (HI) to the hottest gas (OVI) and the warm gas in between (SiIV, CIII). What is first apparent is the intricate structures visible for all of these ions. The HI naturally has the largest column densities in the filaments that trace the high-density structures within the gas.

The distribution of SiIV and CIII closely follows that of the HI. The greater strength of CIII is related to the fact that it is approximately 10 times more abundant than SiIV for a given metallicity. These low-ionization ions are found mostly in the higher-density gas because the high average temperature of the CGM outside these regions prefers higher ionization states. These trends are also true of other low ions, such as SiII, which show similar features. Conversely, in this map, although the OVI does retain traces of the same underlying structures seen as slightly enhanced column density regions, its higher ionization energy allows it to exist in hotter gas. In this way, the OVI has the largest extent and obtains an appreciable column density value for almost the entire area of the map. This is consistent with Tumlinson et al. (2011) who found OVI in all of their star-forming galaxies, implying a high covering fraction as seen here.

4.3.2 Comparison to COS Halos Column Densities

With column density maps in hand, we now compare the simulation to the uniform, galaxy-selected, quasar sample of COS Halos data, which provide measurements of the column densities of multiple ions as a function of impact parameter to low sensitivities. The ions presented here (SiIII, SiIV, CIII, OVI) span a wide range in ionization energy while having a large number of observations in the COS Halos sample. CIV is excluded as observations are limited by the degraded sensitivity of COS for wavelengths $\lambda > 1500$ Å, necessary for this redshift sample (Werk et al. 2013). As we are considering a single galaxy, the simulation is not expected to reproduce every aspect of the larger population sampled by the survey.

Because of this fact, coupled with the large number of upper and lower limits in the data, the comparison made here between simulated and observed column densities is visual. Every pixel in the column density map is shown so that the validity of the conclusions drawn here is easily confirmed.

As a base case, we assume the standard HM05 background, labeled as g1q1 in figures. Using the method described in Section 4.2.2, the column densities are computed for each ion as a function of impact parameter from the galactic center at $z = 0.2$, the approximate redshift of the data. The center panels of Figure 4.2 show the resulting average radial profiles of three projection angles as well as the value of each pixel for a single projection (shown in Figure 4.1). Each pixel has a width of 1 kpc. The data points are detections and upper and lower limits, respectively, of the COS Halos data set. The color of the data point indicates whether the galaxy is considered star-forming (with sSFR $> 10^{-11}$ yr^{-1}) or passive as in Werk et al. (2013). At $z = 0.2$, the simulated galaxy has a stellar mass of $1.9 \times 10^{11} M_{\odot}$ and star formation rate (SFR) of 6.22 $M_{\odot}/yr$, making it a star-forming galaxy by this classification as expected. This stellar mass is typical of a COS Halos galaxy but this SFR leads to a rate at $z = 0$ that is high compared to the actual Milky Way (noted by Fernández et al. 2012; Joung et al. 2012). However, in the COS Halos sample, five galaxies have this SFR or higher. These points show no special trends in the column densities (Werk et al. 2013) so the comparison done here is valid.

These plots highlight both the average trends of the halo gas as well as the structures seen in the column density maps of Figure 4.1. In general, the median column densities remain roughly constant with impact parameter. However, filamentary structures and satellite galaxies (the peak seen around 40 kpc) provide the possibility of a quasar sightline measuring higher-than-average column densities. Furthermore, the distribution of the pixel values does vary somewhat with the projection angle. In particular, a face-on projection reduces the

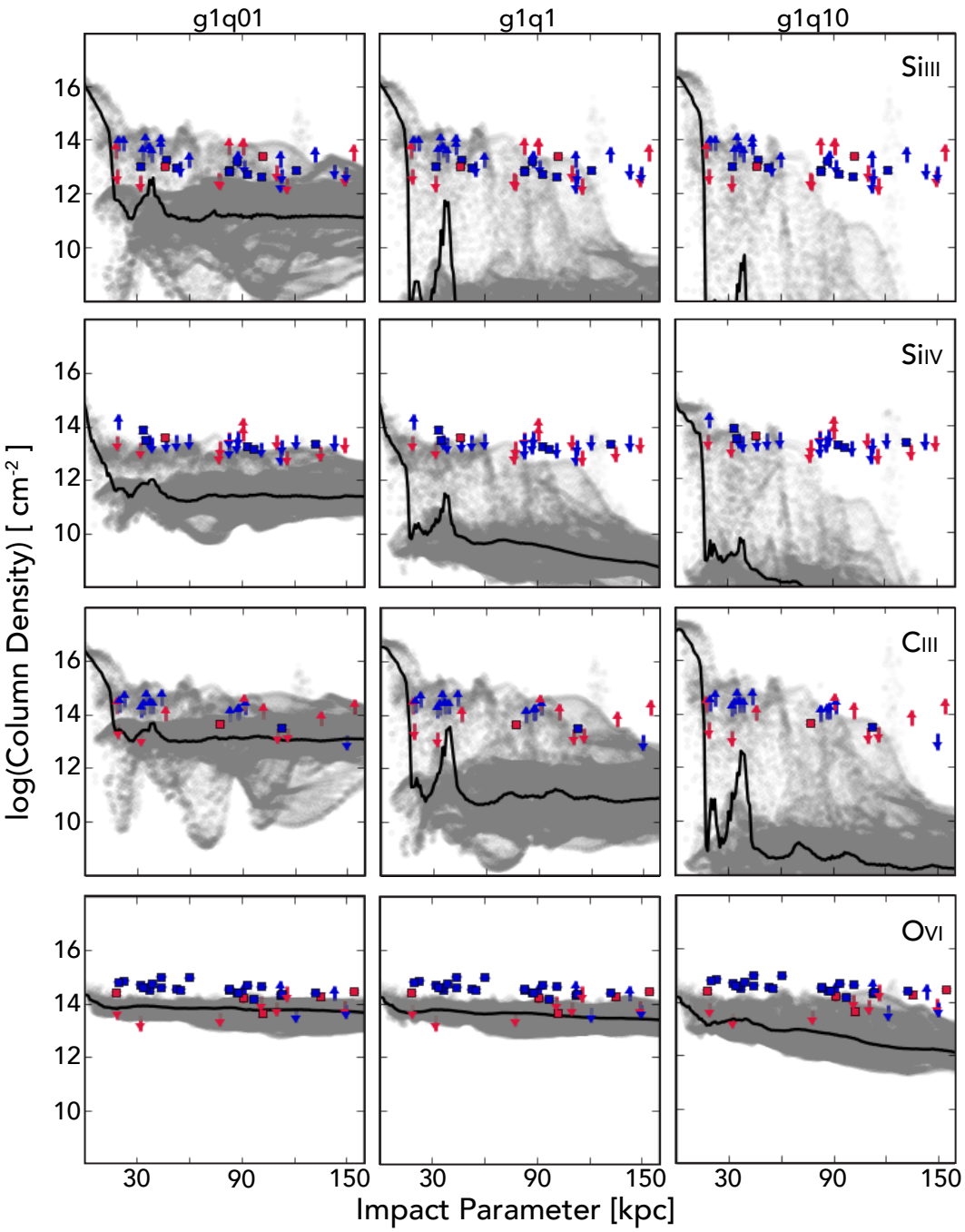

Figure 4.2: Radial profiles of four different ions with gray points showing the values of individual pixels and the black line showing the median. Overplotted are column densities from the COS Halos survey, colored as either star-forming (blue) or passive (red). The fiducial UV background (HM05) fails to reproduce the observed column densities except for the peaks from the remaining filamentary structure and satellite galaxies. Lowering the background to 0.01 times the normal quasar intensity provides a better match to SiIV and CIII though some tension remains. OVI appears more collisionally ionized such that the changes are less marked but no background successfully reproduces the high OVI absorption seen in star-forming galaxies.

scatter in the inner radii as the disk dominates the gas distribution. However, the average values are generally unaffected. Throughout the paper, we plot a mostly edge-on projection which allows for a better evaluation of how gas extends perpendicularly from the disk while lessening the influence of the disk itself.

It is apparent that for this simulation, this model is not a good fit to most of the data. The higher-density filamentary structures bring many of the CIII measurements into alignment with the data but the small covering fraction of these filaments makes it unlikely that they constitute a large fraction of the COS Halo absorber population. The SiIV data is composed of many upper limits which means that the low predicted values may be more in line with the simulation. However, the detections are still mostly too high to match the simulation at the larger impact parameters.

The OVI measurements, on the other hand, are composed mostly of detections. Our inability to match the OVI prediction for the star-forming galaxy model highlights a true disagreement. The observed galaxies with similarly high star formation rates as our simulated galaxy have properties similar to the other star-forming galaxies while the simulation is more in agreement with the passive population. Taken together, this suggests that the details of the hot phase of the CGM are not being properly reproduced.

Nevertheless, it is encouraging that the simulated gas shows a roughly flat radial profile like the data, as this was not guaranteed a priori. Figure 4.10 shows the radial profiles of the density, temperature, and metallicity at z=0.2 in orange. The density decreases much faster than temperature beyond the disk (excepting peaks that represent satellite galaxies) while the metallicity actually begins to rise beyond 50 kpc. The combination of warm/hot temperatures, falling density, and increasing metallicity combine to produce the roughly flat column densities seen here in Figure 4.2. Yet, the points are not as tightly clustered as the data and are roughly two orders of magnitude too low.

It is tempting to simply increase the metallicity of the gas to increase the column densities, but it is not clear that this would lessen the discrepancies with the observations. The metallicity and temperature of the gas are intimately linked. Increasing the metallicity of the gas may lower the temperature such that the simulation remains in disagreement with some of the data. For example, SiIII and SiIV which prefer colder temperatures, would most likely benefit from added metallicity but OVI which prefers hotter temperatures may not. Furthermore, keeping the density and temperature fixed, the metallicity would need to be raised by approximately two orders of magnitude to bring better agreement with the data, assuming the fiducial HM05 EUVB. This would put much of the CGM at solar metallicity or above, in contrast to most expectations and the measurements of Werk et al. (2014).

Instead, these discrepancies are an indication that the simulation that is tuned to reproduce bulk stellar properties of galaxies over time fails to do the same for these multiphase CGM gas properties. However, this is not the first simulation to have such issues. Hummels et al. (2013) also analyze an `enzo` simulation with a similar thermal feedback prescription but at lower resolution and report the same difficulties. Likewise, the SPH simulation of Ford et al. (2015) also fails to reproduce the OVI densities even though they implement a non-thermal wind prescription for their feedback. One success is that of Salem et al. (2015), whose implementation of cosmic ray feedback successfully match the data for all ions. A discussion of these different methods is found in Section 4.5.

Thus, the typical solution that is invoked and explored in these works and many others is a modification to the stellar feedback prescription, changing the density, temperature and metallicity of the simulated CGM (e.g. OWLS, EAGLE, FIRE, described in Schaye et al. 2010, 2015; Hopkins et al. 2014, respectively). This range of parameterizations can have an uncertain impact on the gas quantities such that new feedback solutions require the simulation to be re-run to capture the changes. We explore the role of feedback further in

Section 4.5.

However, the EUVB is also important in setting the ionization state of the gas and is not well constrained. Variations of the Haardt & Madau (1996) background (e.g. HM96, HM01, HM05, HM12) are implemented in most simulations and CLOUDY. While these are the best models to date, there is still significant uncertainty in the exact strength and shape of the EUVB. To this end, we chose to explore the impact of this uncertainty by varying the intensity of the galaxy and quasar components of the HM05 background and examining the effects on the resulting column densities. In the following analysis, two bracketing cases of the quasar intensity are presented to examine the reasonable range of effects on the predicted column densities. At one end, the quasar intensity is 100 times less intense than standard (g1q01) and at the other, the quasar intensity is ten times more intense (g1q10). These properties are summarized in Table 4.1 for easy reference. We performed the same analysis for a range of quasar intensities spanning these two cases and the trends seen across the three values presented here are consistent with these results. Furthermore, these two cases bracket current estimates of the photoionization rate with high-redshift Lyman α forest studies preferring higher backgrounds (Kollmeier et al. 2014; Shull et al. 2015) and with low-redshift Hα upper limits preferring lower backgrounds (Adams et al. 2011). Further discussion of the EUVB and its uncertainty can be found in Appendix 4.A. In addition, the galaxy intensity was varied in a similar way but with little to no effect on the predicted column densities as it provides less of the ionizing flux.

Table 4.1: EUVB Model Summary

Name	Galaxy	Quasar
g1q01	1.0	0.01
g1q1	1.0	1.0
g1q10	1.0	10.0

The first and last columns of Figure 4.2 once again show the radial profiles of the column densities of our simulated galaxy but with these altered EUVBs. With g1q01 in the first column, it appears that lowering the quasar intensity to 0.01 times its normal value provides a much better fit to the low-ion data, SiIII, SiIV, and CIII. The majority of the pixels are now in better agreement with the data which is consistent with the idea that this softer spectrum is no longer over-ionizing the gas. Raising the quasar intensity as seen in the last column with the g1q10 models results in a much larger disagreement between the simulation and the data, which is thus consistent with the picture of over-ionization. Together, this suggests that photoionization is the dominant process in producing these low ions. OVI, on the other hand, is mostly unaffected, suggesting that the gas is predominantly collisionally ionized. Most of the halo volume is at about the same density and temperature, accounting for the small spread in OVI column density values. The scatter that is introduced is actually toward lower column densities with larger quasar intensity, consistent with the recombination rate of the lower-density gas not being able to counterbalance the increased photoionization. This demonstrates that producing the correct amount of OVI is not a simple matter of increasing the photoionization of the CGM.

Observationally, there is support for the approach of varying the EUVB. Crighton et al. (2015) allowed the power-law slope of the Haardt & Madau (2012, , HM12) background between 1 and 10 Rydbergs to vary and found that half the components in their absorption spectra preferred an altered slope. One component agrees with the findings here, preferring a softer background, but the others are better fit by a slightly harder spectrum. If variations of the EUVB are necessary to explain absorption components within the same sightline, it is reasonable to expect that the EUVB would vary amongst the many galaxies that compose the COS Halos sample. Examining how this variation changes simulated predictions given otherwise identical physical conditions can thus provide insight into how to interpret such

measurements.

On the other hand, the preference of this simulation for a weaker EUVB background is in fact in contrast both with these column density component measurements as well as the known limitation of the HM12 background failing to reproduce the column density distribution of Lyman α forest absorbers, known as the photon underproduction crisis (Kollmeier et al. 2014; Shull et al. 2015). Solving this crisis calls for an increase in the photoionization rate of the HM12 background. However, the HM05 model used here is more consistent with the findings of Kollmeier et al. (2014) while it is less consistent with the $\log(N_{\rm HI}) > 14.0$ distribution plotted in Shull et al. (2015). This uncertainty in the low-redshift EUVB supports our decision to vary its intensity though in light of the ongoing efforts in feedback and subgrid physics, we acknowledge that this is likely not enough to bring full agreement between the simulation and observations. If a different feedback method allowed for the gas in the simulation to be cooler at late times, the EUVB would not have to be so low to produce the necessary amount of low ions such as SiIV and CIII.

Overall, we find that column densities predicted by the simulation using the standard HM05 background do not provide the best match to recent observations. Instead, the simulation prefers a softer, reduced quasar intensity to produce the necessary large amount of low-ionization gas. This demonstrates that simulation predictions are sensitive to the assumed EUVB and that this assumption should be considered in conjunction with efforts to vary feedback methods, but that this preference of a reduced EUVB, in tension with certain observations, cannot solve the issue entirely.

4.3.3 Comparing to Derived Gas Properties

Just as CLOUDY can be used to predict column densities from simulated physical gas properties, measured column densities can be used to place constraints on the physical properties

of the gas that is producing the absorption. Here we compare the observationally derived gas density and temperature of Werk et al. (2014) to those of the simulation.

We choose to compare the modeled temperature and density from the data directly to the simulation as opposed to computing mock spectra from the simulation and comparing to the data directly. Both require CLOUDY modeling and assumptions about the EUVB, abundance patterns and ionization equilibrium and in this way, we do not need to re-analyze the spectra of the COS Halos team. Furthermore, the simulation densities and temperatures are weighted by the column density of the ion of interest, reflecting the preferential detection of higher column density features used in the modeling.

For each of the column density radial profiles shown in Figure 4.2, the hydrogen number density, $n_{\rm H}$, and temperature used in computing the column densities were projected along the same axis, weighted by the ion number density of interest within the g1q1 model. Figure 4.3 shows the resulting $n_{\rm H}$ and temperature for the four ions being discussed (SiIII, SiIV, CIII, OVI). The 2D histogram is colored to show the average column density of the lines of sight contributing to each bin.

The plotted points are derived from the modeling of the column density observations by Werk et al. (2014). The reported values of the ionization parameter, log(U), are directly converted to $n_{\rm H}$, assuming the ionizing flux of HM05. For the temperature, CLOUDY models were generated using the adopted value of $\rm N_H$ and each permutation of the maximum and minimum values of log(U) and metallicity. For sightlines where there was an upper limit for the metallicity, a lower boundary of [Fe/H] $= -6$ was assumed. In this way, each absorber has four data points associated with it, the combinations of the maximum and minimum values for $\log(U)$ and metallicity, representing the range of acceptable values from the data. CLOUDY then reports the best equilibrium temperature of such a gas cloud, plotted here. This was done for the fiducial model, g1q1, which best matches the EUVB background used

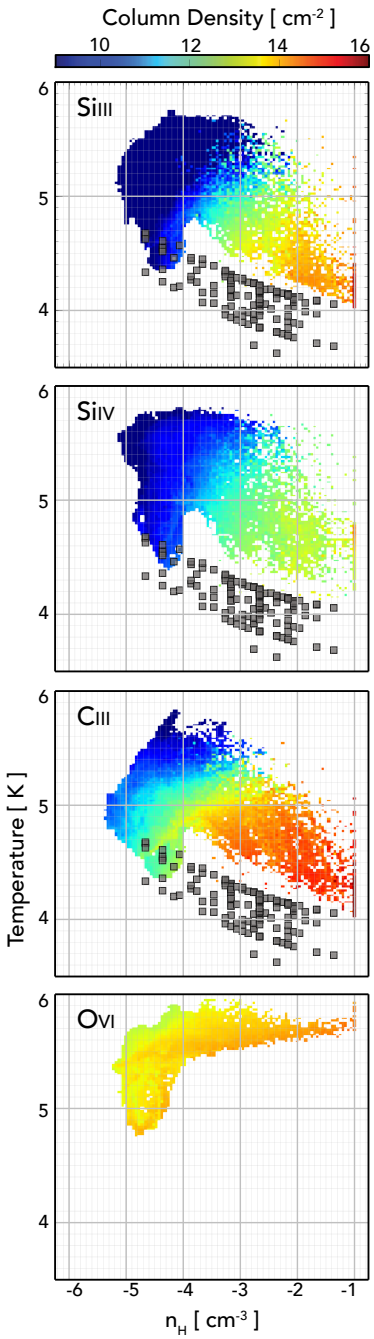

Figure 4.3: Hydrogen number density ($n_{\rm H}$) and temperature, weighted by the given ion number density along the line of sight within the g1q1 model. Colors correspond to the average column density of lines of sight contributing to each bin. Plotted squares are the values implied by the modeling of Werk et al. (2014). The simulation and observations span the same range of densities while the simulation temperatures are universally higher. This also shows the OVI clearly in a different phase medium, while data points are not included as the ion is explicitly not fit by Werk et al. (2014).

to derive the parameters in Werk et al. (2014).

This plot more than any other shows that OVI is in a different phase from the other low-ionization species. It is found exclusively in the hottest gas and the fact that the column densities are uniform across the entire density range reflects the conditions necessary for its longer-lived existence instead of cooling immediately. Data points are not shown for the modeled COS Halos data as OVI is explicitly left out of the CLOUDY modeling of Werk et al. (2014), who are focused on cooler gas ($T < 10^5$ K).

More surprising is the discrepancy between the properties of the low ions in the simulation and the observations. For CIII, SiIII, and SiIV, the majority of the simulated points have $\log(n_{\rm H}) < -4$ but span a large range in temperature. Conversely, the observational points have a clear relation where the temperature decreases with increasing density. This trend is perhaps reproduced in CIII in the simulation but at higher temperatures.

These plots show that gas with a measurable column density is found at low temperatures and high densities. Yet almost all of the gas in the simulation is at a higher temperature than those implied by Werk et al. (2014). None of the gas within a radius of 100 kpc reaches this low of a temperature. Part of this may be due to observational selection; the majority of the simulated gas is at low density, below the detection threshold (see the second column of Figure 4.8). Alternatively, there may be physical differences between the simulated gas and the modeled observations that can explain the discrepancy in the column densities. However, we have shown that this may also be alleviated by altering the assumed EUVB.

In short, although the simulated galaxy has column densities that can be brought into rough agreement with the data, the physical conditions of the gas producing such values are inconsistent with those derived from the data. However, the differences between these two approaches should be noted. CLOUDY, by design, constructs a cloud with uniform density and temperature in local ionization equilibrium. With only the EUVB fixed, it tends toward

lower temperatures and produces a relationship between density and temperature seen as a track in the data plotted in Figure 4.3. The simulation, on the other hand, is run with the intent of retaining the large-scale and complex structure of the CGM gas, with ionization fractions computed for individual cells using a fixed temperature and density. This work has shown that it is possible for this cosmological CGM to produce column densities in the range of those predicted by the idealized clouds intrinsic to CLOUDY, even with largely varying gas properties, if only the assumed EUVB is altered.

4.4 Emission

While the previous section demonstrates the power of absorption-line studies, it also highlights some of their limitations. Absorption-line measurements are extremely sensitive probes of low column density gas, but it is challenging to understand which physical structures in the halo we are probing with these data. Also, the limited number of sightlines per galaxy hinders any attempt at understanding the spatial extent or scale of the structures detected. If instead it was possible to image the entire galaxy in emission, such maps may begin to reveal coherent structures or asymmetries in a gaseous halo that could help place stronger limits on gas accretion and outflows from the galaxy.

Although the simulation fails to accurately predict the column density distribution of CGM gas, we feel that they have sufficient fidelity to obtain new estimates of CGM emission and to determine whether the emission signal is within reach of new observational capabilities. In particular, our analysis of CGM emission from a high-resolution simulation of a galaxy at low redshift is distinct from most other recent studies that probe the overall, diffuse emission-line cooling from CGM halos at lower resolution. This work provides a benchmark for simulations of this type for future comparisons with different theoretical prescriptions

and observations. In this section, we present a complementary set of emission maps and show how they vary with photoionizing background and redshift. We highlight the ways in which these maps provide a distinct and unique view of the morphology and evolution of the CGM. We also explore how emission varies with $n_{\rm H}$ and temperature in the context of the absorption discussed in the previous section. We also determine the detectability of such gas, thereby informing target selection and instrument design for upcoming missions.

4.4.1 Emission Maps

Figure 4.4 shows the emission maps of four of the brightest lines at $z = 0.2$, the same redshift as Figure 4.1 and with the same resolution. Throughout this section, we consider CIV in place of SiIII as it emits more brightly and is an intermediate ion between CIII and OVI, except within roughly the innermost 25 kpc (a slightly smaller radius than that seen by van de Voort & Schaye (2013)). In general, SiIII follows the same trends as SiIV, which is shown. Furthermore, we do not present Lyman α emission (although it likely produces the strongest signal) because resonant scattering is known to change the extent and shape of the emission (e.g. Lake et al. 2015; Dijkstra & Kramer 2012; Zheng et al. 2011) and the required radiative transfer calculation for Lyman α and other lines is beyond the scope of this paper and deferred for future work. We assume that the impact of scattering for other emission lines is negligible.

Comparing Figures 4.1 and 4.4, it is visually apparent that emission and absorption trace the same high-density structures. However, the emission surface brightness spans many more orders of magnitude, making the relevant range much bigger than that of the column density measurements. A similarly large range was reported in earlier work by Bertone & Schaye (2012). Because much of the emission is expected to come from collisional excitation of the gas, the n^2 dependence of this process causes the large spread in values seen here and makes

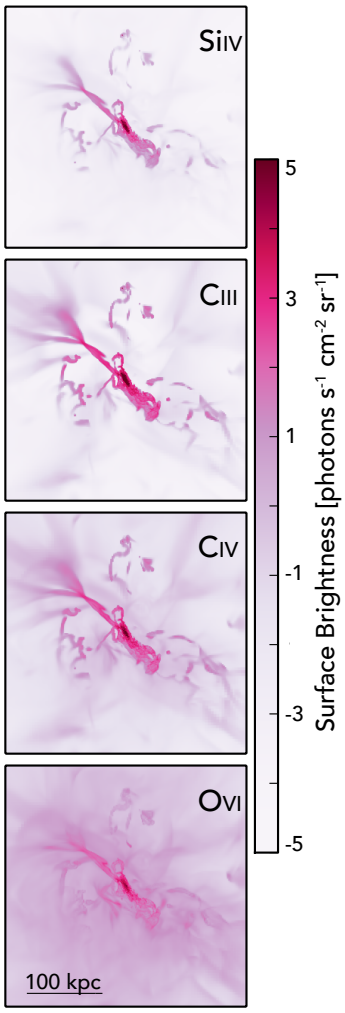

Figure 4.4: Emission maps of SiIV, CIII, CIV and OVI respectively at $z = 0.2$ with a resolution of 1 kpc. As in Figure 4.1, OVI has the largest covering factor while the other ions more closely follow the underlying, cold gas structures. However, the surface brightness spans a wider range of values, demonstrating how sensitive the emission is to the density and temperature of the gas.

the higher-density structures the brightest features and easiest to detect. Most of the gas far from the disk is at low emission levels that are undetectable, as discussed below. This suggests that even further from the galaxy, detections of the even lower-density intergalactic medium will remain out of reach.

Furthermore, as with the column densities, the low ions (SiIV, CIII) trace the filaments where the density is higher and, just as importantly, the temperature is lower. (The same is true for the not-shown SiIII line, which is very similar to SiIV). CIII is the strongest emitting line, consistent with previous work that has considered the line (van de Voort & Schaye 2013; Bertone et al. 2013; Bertone & Schaye 2012). As the peak of the emissivity curve for a given ion moves to higher temperatures, the emission becomes more prevalent for the majority of the diffuse halo which roughly has a temperature of $10^{5.5}$ K. For example, this is the peak temperature of OVI emissivity and as such, this line supplies strong emission throughout the entirety of the halo. Beyond 10^6 K, however, the OVI emission will again become less volume filling as most of the CGM is not hotter than this. Such biasing of SiIV to higher-density regions and OVI to less dense regions was also reported by van de Voort & Schaye (2013) and Bertone & Schaye (2012) and appears to be a fundamental prediction of any simulation containing a warm/hot CGM halo.

4.4.2 Photoionizing Background

The results above assume the single, fiducial HM05 ionizing background. It was shown in the previous section that varying the intensity of this background can bring the simulation more in line with the absorption observations, but what effect does this have on the predicted emission? Figure 4.5 shows the same radial profiles as Figure 4.2 but for the surface brightness values of each projected pixel. A comparison of these two plots shows that the median values of the emission are affected by the change in EUVB in mostly the same way

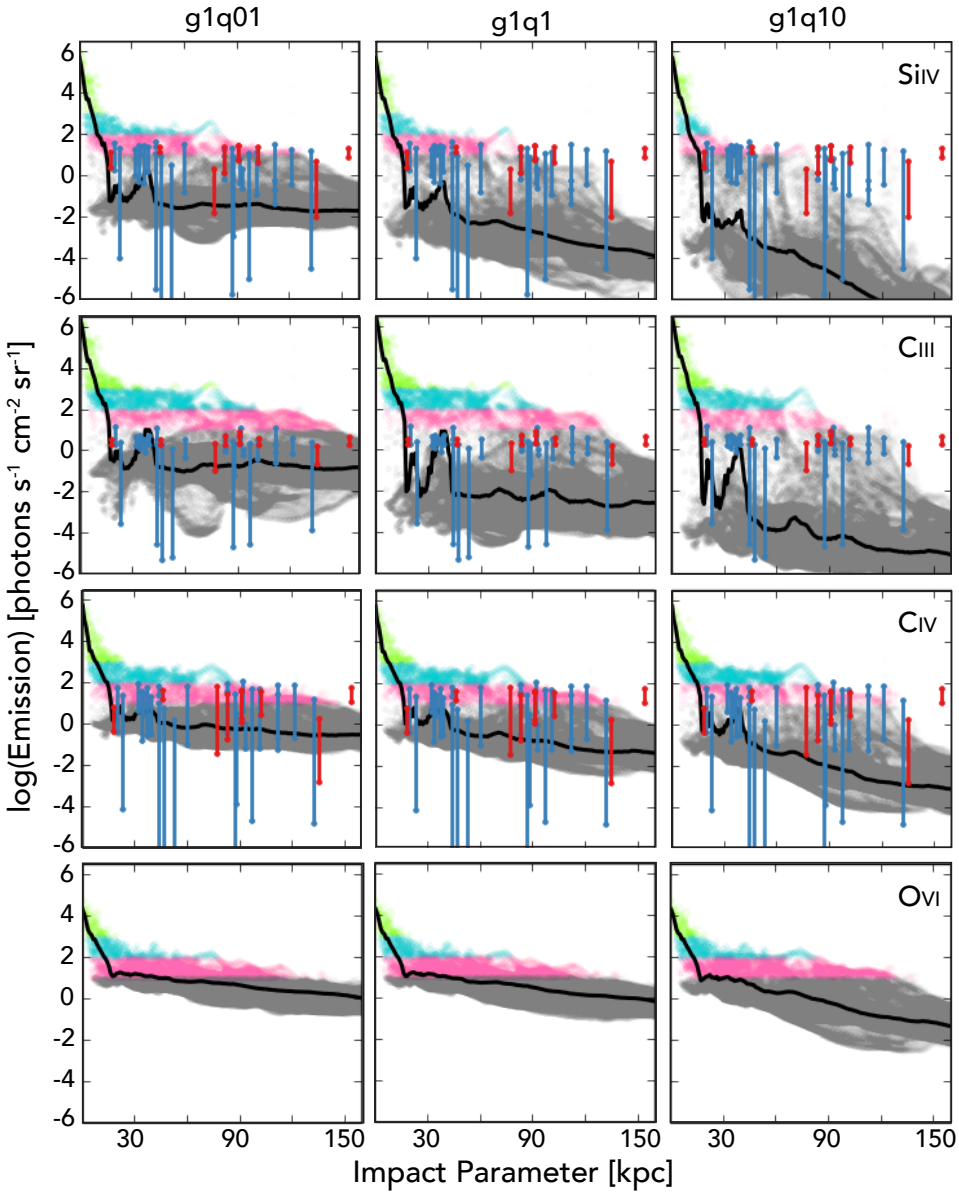

Figure 4.5: Radial profiles of SiIV, CIII, CIV and OVI emission at $z = 0.2$ for the three EUVB backgrounds considered. Here the simulated points are colored by their possibility of detection with green being definite, blue being probable, and pink being possible (see Section 4.4.4.1). The black line represents the median value. The median emission values are affected by the change in EUVB in the same way as the column densities (see Figure 4.2). However, the extent and number of the brightest pixels with the highest detection probabilities are mostly unchanged by varying the EUVB. Finally, overplotted are emission values associated with the density and temperature reported in Werk et al. (2014) for their absorbers. The large range for many of the points is a result of upper limits placed on the metallicity in the data. Although the column densities were not in agreement, the emission values are in fact generally lower than what is predicted by the simulation.

as the column densities. To further quantify this notion, Table 4.2 shows the median value of the radial profiles of both the column density and surface brightness predictions at 100 kpc and $z = 0.2$ for the three EUVBs considered in both sections. For SiIV and CIII, the median values of the column density increase by almost two orders of magnitude in the g1q01 model relative to the fiducial model and the same is true for the emission. The OVI is more unaffected in both absorption and emission. When considering g1q10 relative to g1q1, both the column density and surface brightness medians decrease by the same orders of magnitude for SiIV and CIII, and the OVI by 0.6 orders of magnitude. The ionizing background now over-ionizes the low-density gas as before, leading to larger changes in both absorption and emission of all ions, including OVI.

However, these median levels of emission are below the detection limits of upcoming surveys for all the models and thus the EUVB does not have a strong effect on what will realistically be possible to detect. In Figure 4.5, the points are colored by rough detection probability cuts: green points are certain to be detected, blue points are likely to be detected and pink points are possible to detect. This coloring shows that the pixels with the highest surface brightnesses extend about equally far for all of the EUVBs. Instead, their distribution and number depend mostly on the density and temperature of the gas. Because a 2D image would capture all of these pixels, the number and brightness of these emission peaks can perhaps provide a more unambiguous look at these underlying gas properties. Such surface brightness effects are discussed in more detail in Section 4.4.4.1.

More importantly, however, the pixels with the highest surface brightness have the highest possibility of detection and extend about equally far for all of the EUVBs. Their distribution and number depend mostly on the density and temperature of the gas. Because a 2D image would capture all of these pixels, the number and brightness of these emission peaks can perhaps provide a more unambiguous look at these underlying gas properties.

Table 4.2: Median Values of z=0.2 Radial Profiles at 100 kpc

ABSORPTION

	g1q01	g1q1	g1q10
SiIV	11.46	9.45	7.00
CIII	13.18	11.22	8.76
OVI	13.75	13.55	12.66

log(Column Density) [cm^{-2}]

EMISSION

	g1q01	g1q1	g1q10
SiIV	-1.41	-2.84	-5.24
CIII	-0.47	-1.96	-4.23
OVI	0.50	0.33	-0.46

log(Surface Brightness) [photons s^{-1} cm^{-2} sr^{-1}]

This variation of the emission radial profile with EUVB is opposed to previous studies which found no variation in their simulated emission profiles when the assumed background was increased by a factor of 10, although neither explores lowering the EUVB (Sravan et al. 2015; van de Voort & Schaye 2013). Also, both average over a large number of halos over a range of masses, which may smooth some of the changes seen here, particularly as we are presenting the median. However, creating the same radial profiles as Figure 4.5 but for $z = 1$, we also found little to no variation in the profiles. Yet the fiducial background is higher at $z = 1$ than at $z = 0.2$ and encompasses the regions covered by the g1q1 and g1q10 models at $z = 0.2$. This suggests that the gas state is more dominated by collisional ionization at $z = 1$, which is supported by the higher density of the gas at early times (see Section 4.4.3 and Figure 4.8 for more details).

We point out that the extremely low SB values predicted here are purely theoretical predictions from the gas itself. They do not include the EUVB photons as well as possible

photon pumping and scattering from the host galaxy continuum. The UV continuum of a star-forming galaxy typical of the COS Halos sample will be on the order of 500 photons s^{-1} cm^{-2} sr^{-1}, although this is dependent on the uncertain escape fraction of the ionizing photons (see Figure 13 of Werk et al. 2014, for a plotted, typical galaxy SED). With only a fraction of this flux contributing to the pumping or scattering of a specific line of interest, the floor set by these processes will be above the theoretical limit shown here but below any upcoming detectable limit. Furthermore, this will mostly affect the volume closer to the star-forming disk and not alter our predictions for the more distant CGM.

In addition to the projected simulation pixels, "observational" data have been generated from the physical parameters inferred from the CLOUDY modeling of Werk et al. (2014). For each line of sight, the adopted $N =_{\rm H}$ was paired with each combination of the maximum and minimum values of the metallicity and ionization parameter to compute the emission from such a cloud using CLOUDY. Then the maximum and minimum computed values of each sightline are plotted as connected points. The large acceptable range for a high faction of the sightlines is due to the degeneracy of the ionization parameter (which for this model is a proxy for $n_{\rm H}$) and the metallicity. As we previously noted, the measured column densities are not in agreement with the simulated values. However, the emission predicted from the column density data using the method described above, bracket nearly all of the simulated emission values of SiIII, SiIV, and CIII. Data points are not shown for OVI since Werk et al. (2014) explicitly model gas cooler than the gas seen in the simulation ($T < 10^5$ K).

The complex ionization structure in the CGM halo means that regions of strong absorption do not always produce significant associated emission, particularly for OVI which is known to have a low column. In part, this is because absorption-line measurements are typically probing gas in the ground state, allowing ionic absorption of incoming quasar photons. Emission, on the other hand, is generated as higher ions cool through the metal line of

interest or through collisional excitation and cooling of lower ion gas; these processes tend to be more transitory in nature. We suggest here that the CIII emission predictions may be the most reliable as the column density distribution is best reproduced by the simulation for both the fiducial EUVB and the modified, weaker EUVB. The column density of OVI is known to be underproduced and the temperature of the hot halo generating the OVI is contested amongst the simulations (discussed further in Section 4.5). However, we expect the overall trends seen here with OVI being found in the hotter, volume-filling gas to remain valid. CIV is likely intermediary, but the lack of data in the COS Halos sample limits our conclusions.

Overall, the density structures revealed in the column density maps are also present in the emission but the emission values span a much larger dynamic range. This dynamic range reflects the emission's biasing toward higher density and thus higher signal regions. However, this biasing and its unique dependence on density, temperature and metallicity can provide complementary constraints on these properties of the gas when combined with column density measurements. Another advantage of emission observations is that varying the ionizing background does not have a strong effect on the brightest emitting pixels as it does on the median column density that could be detected. Because the emission trends and detection possibilities do not vary with the EUVB, in the following sections, we present results using the fiducial background.

4.4.3 Redshift Evolution of the Emission

Our simulations can also be used to predict the physical distribution of CGM emission over a a large range of redshift, and imaging the CGM can be used to better understand what is driving the emission at each redshift. In particular, the nature of the CGM may change dramatically from $z = 1$ to $z = 0$ as the SFR declines on average and as galaxies in this

mass range potentially transition from "cold mode" to "hot mode" accretion.

Figure 4.6 shows the evolution of four emission lines for our simulated galaxy using the fiducial background. The proper physical size of the box is constant in each panel as well as the resolution of 1 physical kpc. Furthermore, in order to study the intrinsic evolution of the emission separate from the cosmic expansion, these plots show the true surface brightness of the object without accounting for the cosmological $(1+z)^4$ dimming - i.e. we set $z = 0$. In this way, the brightness of the emission is directly related to the underlying density, temperature and metallicity and their evolution alone. We discuss the importance and effects of this dimming in the following section.

It is easy to see that as the redshift increases, the emission becomes brighter and extends further and more spherically from the disk. This is most striking for the low ions which emit at an appreciable level almost out to the virial radius at $z = 1$ while they are limited to high-density features at $z = 0$. However, the extended emission sphere surrounding the disk at $z = 1$ in all four ions considered disappears by $z = 0$, leaving only the filamentary structure behind. This increase in the bias of the emission towards high-density regions at later times as compared to emission at $z = 3$ was noted by van de Voort & Schaye (2013), and we point out that this is true even when comparing $z = 1$ to the present day.

These changes in the emission values are more easily seen when quantified as a covering fraction. Figure 4.7 shows the evolution of the fraction of pixels with an intrinsic emission above two different surface brightness limits (10 and 100 photons s^{-1} cm^{-2} sr^{-1}) for the four ions of interest within a square image that is 320 proper kpc per side with a resolution of 1 proper kpc. Disk pixels have been removed to emphasize the CGM. As redshift increases, the increasing brightness seen in Figure 4.6 leads to higher covering fractions for the emission. For both limits, the fraction doubles between $z = 0$ and $z = 1$ for all the ions. OVI has the largest covering fraction at the lowest level considered except at $z = 1$. CIII and CIV

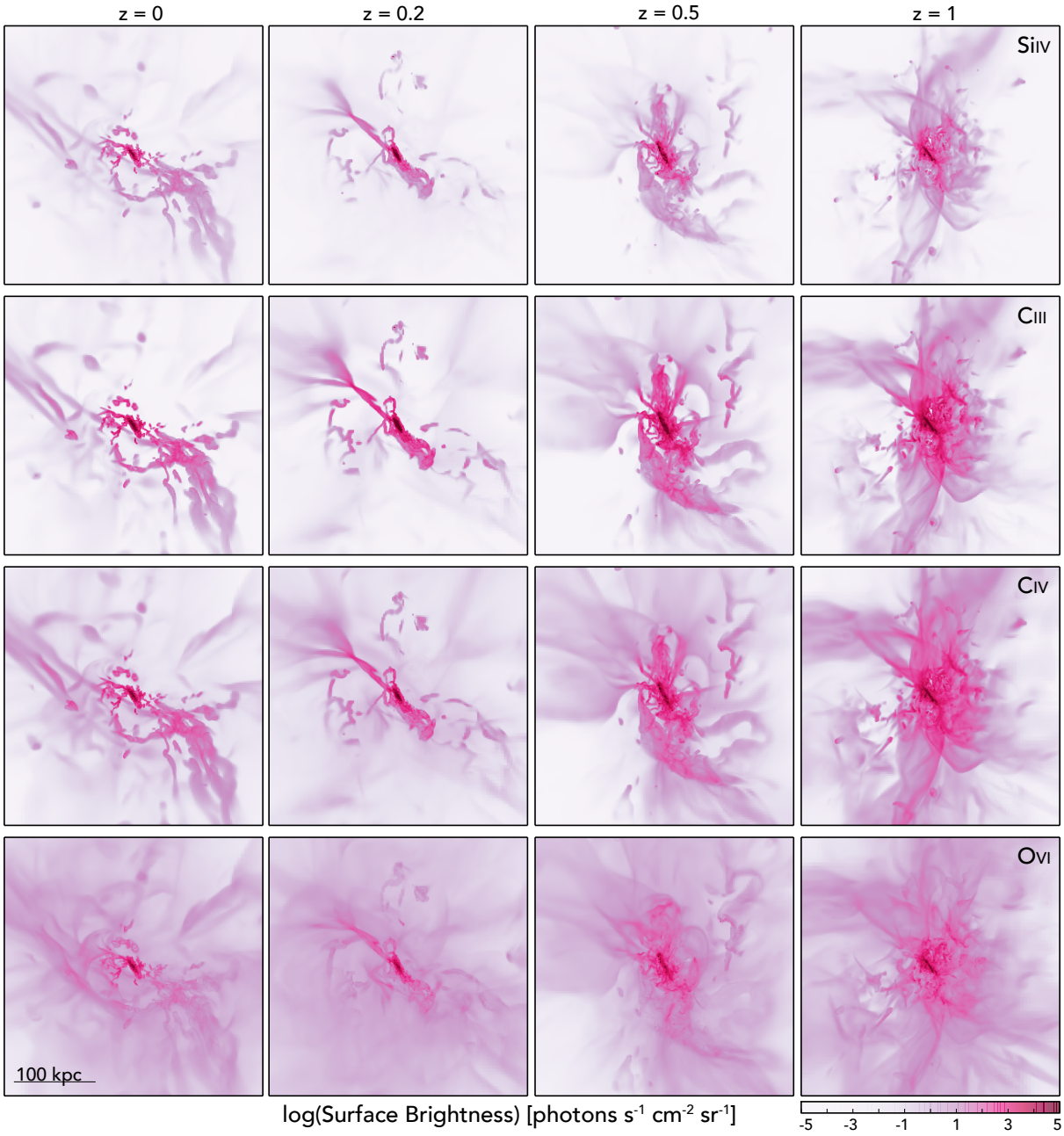

Figure 4.6: Emission maps for SiIV, CIII, CIV, and OVI at $z = 0, 0.2, 0.5, 1.0$ with a resolution of 1 physical kpc and with a fiducial HM05 background showing that the intrinsic brightness increases with redshift (that is, the brightness without accounting for the $(1+z)^4$ dimming - i.e. as if $z = 0$ for the distance). The emission becomes more filamentary with lower redshift as the increasing gas temperature and decreasing average density shift the brightest emission to these remaining high-density regions.

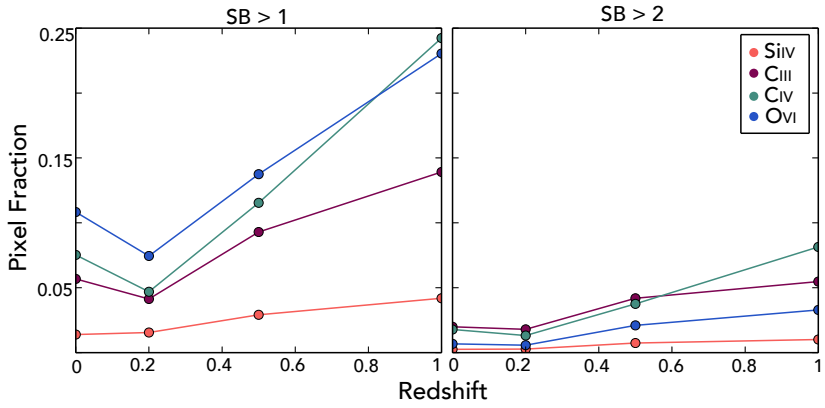

Figure 4.7: Covering fraction for the four lines of interest at two different surface brightness cutoffs: 10 and 10^2 photons s^{-1} cm^{-2} sr^{-1} respectively. This excludes the galactic disk. In general, the emission increases with redshift for all lines. At the lower level, OVI has the highest covering fraction at all redshifts but the highest one. At the higher surface brightness level, CIII is the dominant ion except at $z = 1$ where CIV increases rapidly. This shows the overall increasing emission with increasing redshift, the high covering fraction of low-SB OVI, and that the strongest emission is coming from ions with mid-ionization energies. (Here again the $(1+z)^4$ dimming is not accounted for, i.e., as if $z = 0$ but this has no effect on the trends.)

have similar covering fractions for all the limits and are the dominant lines at the higher SB cutoff, seen in the right panel of Figure 4.7. Most interestingly, by $z = 1$, CIV has the largest covering fraction, overtaking CIII and OVI. Even at the lowest surface brightness limit that we consider, the covering fraction is never higher than 0.25 for any ion as early as $z = 1$, highlighting the difficulty of emission detections.

To better understand these changes in the surface brightness maps, Figure 4.8 shows the density temperature diagram of the galaxy weighted by the emissivity of multiple ions for four different redshifts ($z = 0, 0.2, 0.5, 1.0$). For each of the ions, there is a clear trend toward lower densities and higher temperatures on average with decreasing redshift. The decrease in density causes a lower overall surface brightness across the majority of the halo. Simultaneously, the higher temperatures move the bulk of the gas away from the peak of the emissivity curve of the lower ions. In this way, the emission from most of the volume is

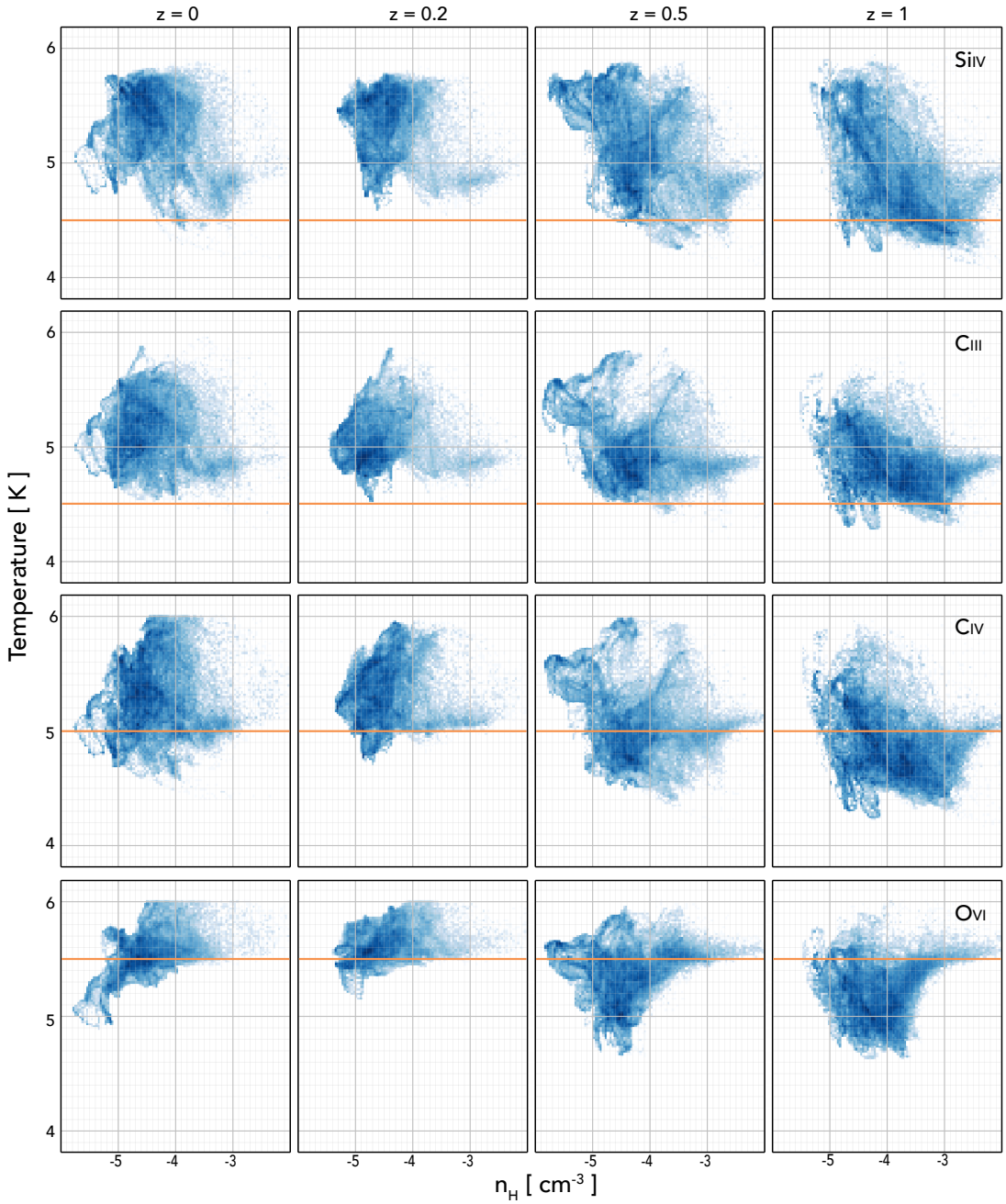

Figure 4.8: Evolution with redshift of the hydrogen number density ($n_{\rm H}$) versus temperature, weighted by the emissivity of a given line. The orange lines show the temperature of the peak of the emissivity curve for that ion. For all ions, the trend is for the gas to move to lower densities and higher temperatures as the galaxy evolves from $z = 1$ to $z = 0$. This change in the gas represents the decreasing role of the filaments feeding the galaxy as well as the cumulative effect of SN-driven outflows.

reduced, leaving only the higher-density and lower-temperature filaments with an appreciable signal. Once again, OVI defies these trends as the higher temperatures at late times are more in line with its emissivity peak, accounting for its continued higher surface brightness throughout the area shown in Figure 4.6.

The question then becomes: what is causing these systematic changes in the density and temperature of the CGM? While this is difficult to answer definitively, there are two dominant effects within the simulation: accretion and supernova feedback. The first effect arises from filaments feeding the galaxy, as seen in the density projections in the left column of Figure 4.9, showing the density evolution of the galaxy and its CGM. At $z = 1$, there are three well-defined filaments penetrating the galactic halo down to the disk. As the redshift decreases, the galaxy mass increases, and cosmic expansion lowers the overall average density of the IGM, these features become broader and do not penetrate into the halo as deeply although they do supply additional gas along with stripped satellite material (Joung et al. 2012; Fernández et al. 2012). Instead, the gas density profile becomes more spherical and more extended as the galaxy evolves.

What's surprising is that this change in CGM morphology is not reflected in the structure of the brighter emission. The fractured filaments exist as surface brightness peaks in the $z = 1$ projection but the bright emission halo is more spherical whereas the brighter emission at $z = 0$ is almost entirely contained in the remains of the filaments with no discernible symmetry.

The explanation resides in the corresponding temperature projections, shown in the middle column of Figure 4.9. At $z = 1$, the halo has a complex temperature structure, with colder, denser gas contained in cold, infalling gas and satellites. By $z = 0$, this is replaced with a spherical hot halo, mimicking the density profile. Even the filaments are bringing in predominantly warm/hot gas (Joung et al. 2012). The weakening of the filaments, the

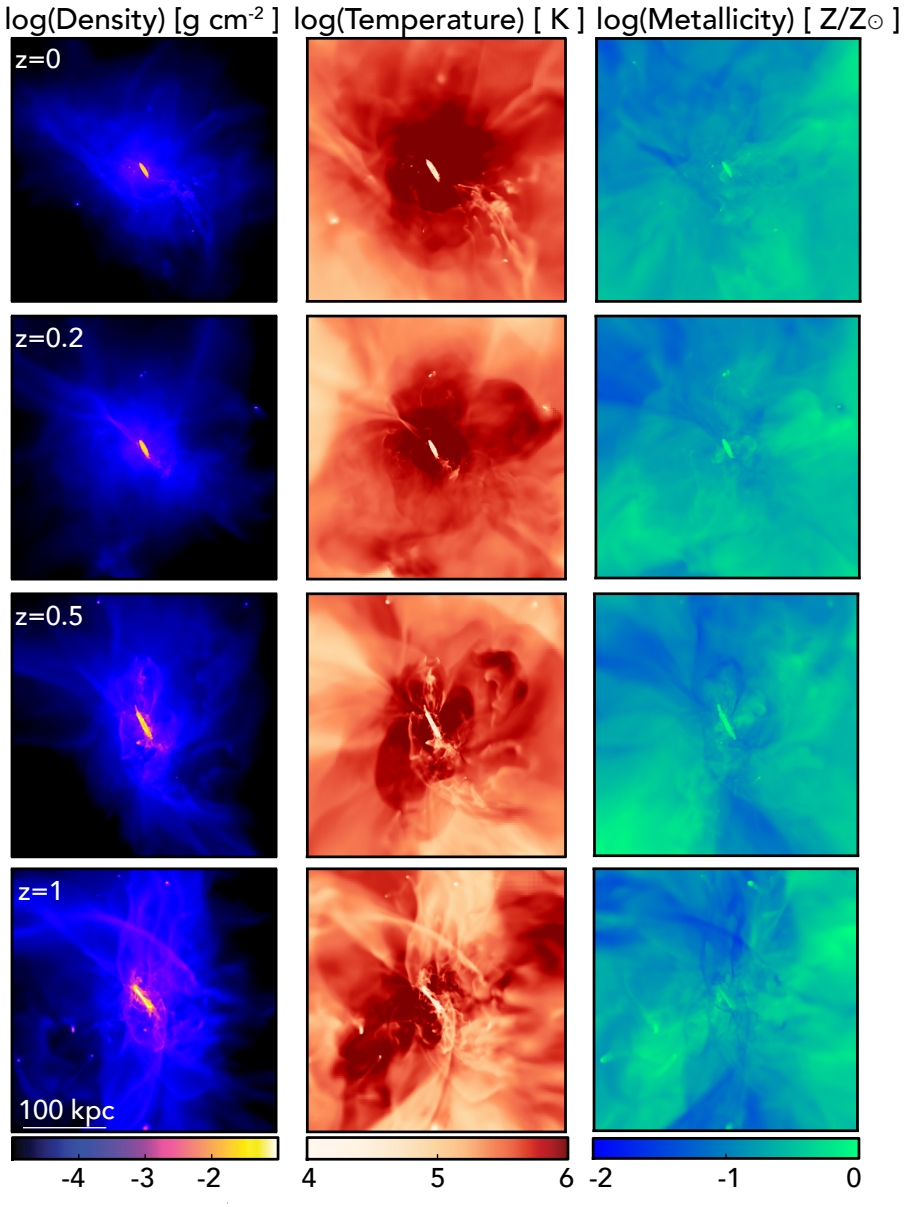

Figure 4.9: Projections of the density (left) and the density-weighted temperature (middle) and metallicity (right). The combined evolution of these quantities is what drives the changes predicted for the emission. Filaments are easily seen feeding the galaxy at $z = 1$ in the density and as low-metallicity regions and have weakened by $z = 0$. The temperatures become higher and more uniform by $z = 0$.

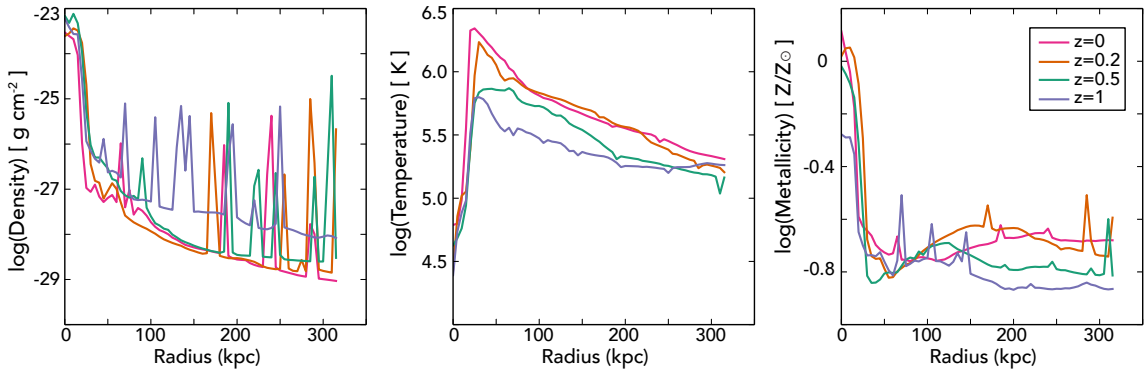

Figure 4.10: Radial profiles of density, temperature, and metallicity at a series of redshifts. The spherical averages of these quantities are plotted. They quantitatively demonstrate the trends driving the evolution of the emission - the average density lowers with time while the temperature increases. Spikes in the profiles correspond to substructure in the halo of the main galaxy.

slowing of their supply of cold gas, and their replacement with a more uniformly hot halo of lower-density gas results in the loss of the large emission halos of $z = 1$. By $z = 0$, only the remaining cold, dense features are capable of producing a significant signal. Figure 4.10 shows the radial profiles of the relevant quantities at various redshifts, which quantitatively demonstrates these trends.

In addition to this change in accretion mode, supernova-driven winds are also effective at creating low-density, high-temperature pressurized bubbles in their wake as they expand through the halo. At high redshift, it has been suggested that galactic outflows are the dominant process powering the time-varying simulated emission (Sravan et al. 2015). Looking again at the temperature projections of Figure 4.9, higher-temperature regions extend perpendicular to the disk. Furthermore, multiple spherical plumes can be seen expanding away from the disk. These features are less visible in the density but still seen. This suggests that outside the filament regions, SN-driven outflows play a large role in shaping the density and temperature distribution of the halo. In particular, because the SN energy is injected as

thermal feedback in this simulation, the temperature of the gas is efficiently raised to $10^{5.5}$K on average, much higher than the peak emissivity of low ion lines, such as CIII and CIV.

In conclusion, at later times, the emission in the metal lines studied here is more structured, tracing the remaining high-density structures, in contrast to the majority of the gas which becomes more spherically distributed and more uniformly hot. This emission may be an effective way to probe continued galactic accretion at low redshift. Additionally, the propensity for the gas to become hotter and more diffuse translates to a decrease in the magnitude and extent of the low-ion emission. Galactic winds coupled with a transition to hot mode accretion no longer resupplying cold gas likely explain the shift to low-density, high-temperature gas at late times.

4.4.4 Implications for Detection

Finally, with an emission signal this faint, understanding how these theoretical predictions relate to what can actually be detected is important for both furthering interpretations of future measurements as well as enabling fair comparisons of theory and observations. In this section, we examine how realistic surface brightness and angular resolution limitations can limit the conclusions that can be drawn about a galaxy's CGM.

4.4.4.1 Surface Brightness Limits

Recent work in CCD technology now allow us to reach extremely high quantum efficiencies in the UV (Hamden et al. 2012) leading to achieving unprecedentedly low surface brightness limits in the UV. In this section, we look to see how this translates into reaching levels where UV emission from the CGM of nearby galaxies can finally be detected.

We consider three regimes of detection possibility for the emission. Pixels with a surface brightness (SB) greater than 10^3 photons s^{-1} cm^{-2} sr^{-1} are certain to be detected by the

specifications of any upcoming instrument and are colored green in the following plots. Those with $10^2 < \mathrm{SB} < 10^3$ photons s^{-1} cm^{-2} sr^{-1} have a high probability of being detected and are plotted in blue. Finally, pixels with $10 < \mathrm{SB} < 10^2$ photons s^{-1} cm^{-2} sr^{-1} have a possibility of being detected and are shown in pink. Exact confidence levels will vary for a given instrument and observing strategy but these are appropriate rules of thumb.

Figure 4.11 again shows the surface brightness maps of Figure 4.6 but now colored to show these detection probabilities. Unlike the theoretical projections, these maps take into consideration the $(1 + z)^4$ dimming of the surface brightness due to the expansion of the universe. The brightest, easiest-to-detect emission (green) always comes from the galactic disk. Some pixels reach this brightness level into the filaments, especially in CIII, but only at the lower redshifts.

Much more promising for CGM studies is the extent of the blue pixels, indicating regions that are likely to be detected. For the brightest ions (CIII, CIV,), these regions extend into a large portion of the filaments at $z = 0$, out to as far as 100 kpc. The mid-level emission is less extended for the high ion, OVI, reaching a radius of only 50 kpc (similar to that found in previous work by Furlanetto et al. 2004; van de Voort & Schaye 2013). Thus, although Figure 4.11 shows that the extent of the emission decreases with redshift, the detectable emission is still an appreciable distance from the main galactic disk. At all redshifts it should be possible to detect emission from CGM gas beyond the galactic (star-forming) disk.

Finally, the lowest surface brightness limits naturally reveal the most extended structure and emphasize the importance of pushing the limits of future instrumentation. However, in considering a range of redshift, the combination of the surface-brightness dimming and the fixed surface brightness limits shapes the observable covering fraction. The radial profiles of Figure 4.5 suggest how this is possible, where the colors of the simulated points correspond to the same limits as the projections of Figure 4.11. At $z = 0.2$, most of the points lie below

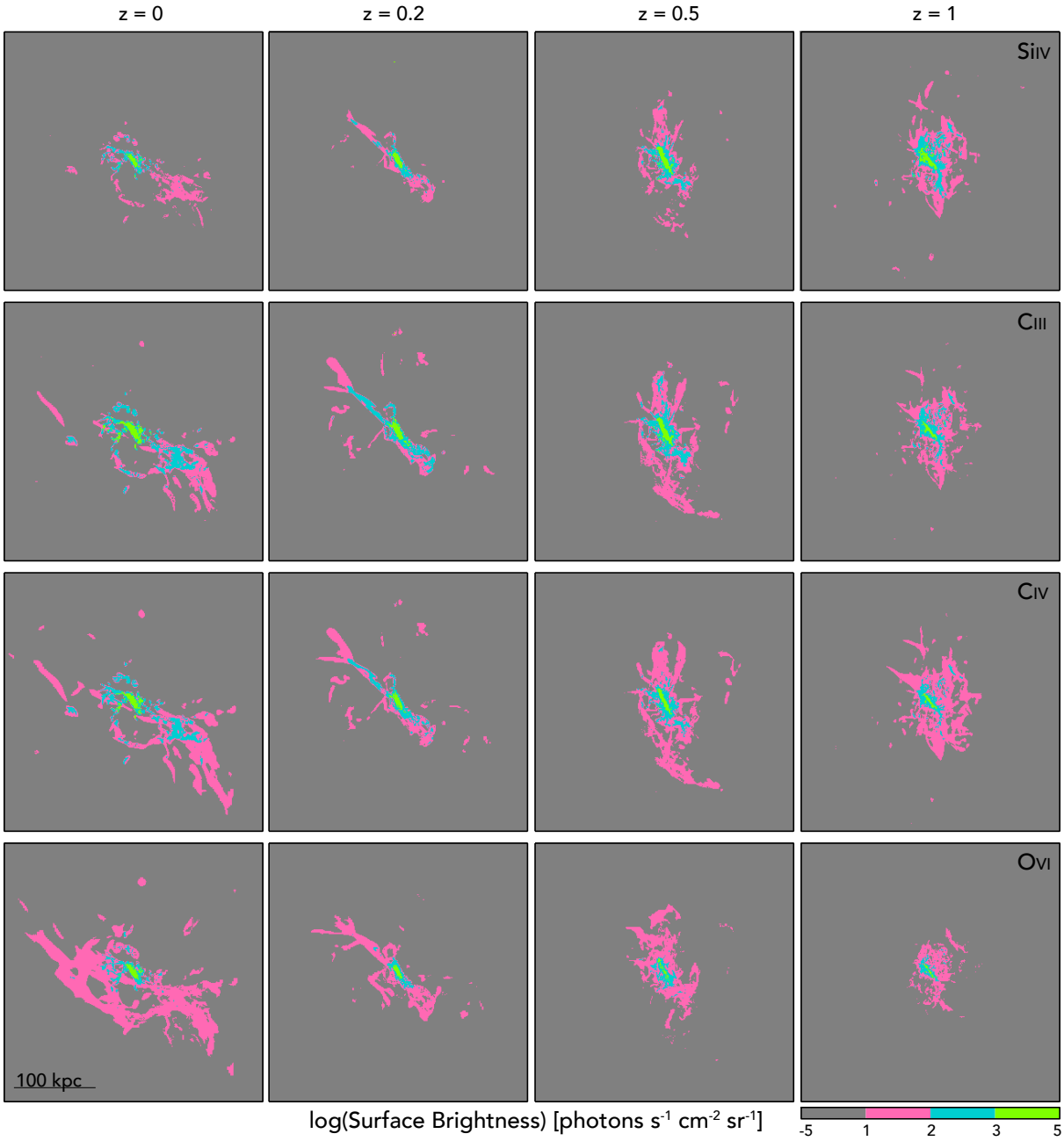

Figure 4.11: Surface brightness maps for three different ions at $z = 0, 0.2, 0.5, 1$. Each map takes into account the surface brightness dimming due to the given redshift. Like in the theoretical predictions of Figure 4.6, the emission becomes more filamentary with time. However, because of the intrinsic brightening of the gas, the extent of the emission varies little between $z = 0.5$ and $z = 1$. OVI is affected the most because it emits primarily at the lowest detectable range at $z = 0$ which is then dimmed from detection.

any reasonable detection limit and the fraction at the lowest detection limit (pink) is greater than at the higher limits (blue, green) at all but the smallest radii. This trend is true at all redshifts. For OVI in particular, much of the emission is intrinsically emitted at the lowest limit considered here because it is mostly generated by the low-density, volume-filling gas. At $z = 1$, most of this dim emission then falls below observational levels once the cosmological dimming is considered. In this way, the extent of possible OVI detections drops from 130 kpc at $z = 0$ to 60 kpc at $z = 1$.

For the low ions, the effect is less pronounced because they emit most brightly and significantly in the relatively overdense filaments and this emission in fact increases with increasing redshift as seen in Figure 4.6 (demonstrated also in Bertone et al. 2013). The surface brightness dimming is thus offset by the inherent increased emissivity, seen as an increased theoretical covering fraction in Figure 4.7. Thus, the decrease in detection extent is less steep yet still pronounced for CIII (150 kpc to 100 kpc) and CIV (150 kpc to 90 kpc). Furthermore, most of this decrease is in place by $z = 0.5$ and little change in the observable properties of the gas happens between $z = 0.5$ and $z = 1$. Work at higher redshifts indicates that these extents are decreasing slightly in physical scales but that they remain at the same fraction of the halo's virial radius (van de Voort & Schaye 2013; Sravan et al. 2015).

Thus, in order to make a clear detection of the CGM, it is necessary to reach a detection limit of at least 100 photons s^{-1} cm^{-2} sr^{-1} to begin to probe extended emission in dense filamentary regions. Pushing down to 10 photons s^{-1} cm^{-2} sr^{-1} provides the possibility of detecting emission from the diffuse, hot volume-filling phase of the CGM. Furthermore, observations close to $z = 0$ increase the chances of detecting this phase as it is the first to drop out of range due to surface brightness dimming. However, between $z = 0.5$ and $z = 1$, the extent of the emission is relatively unchanged at these detection limits, enabling measurements across redshift that could trace the evolution of the CGM.

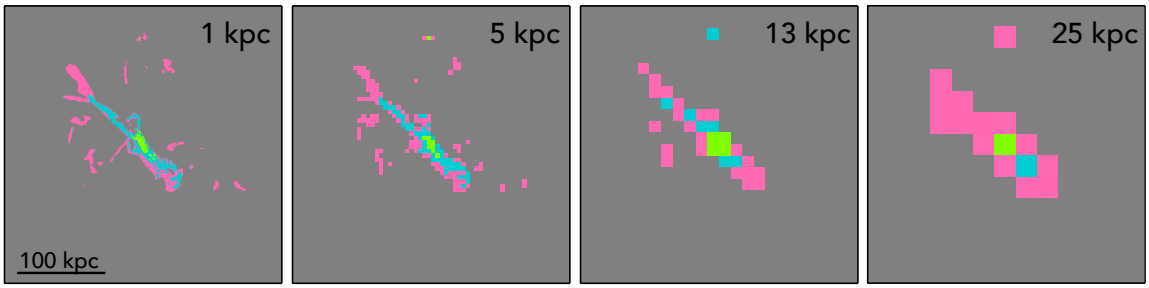

Figure 4.12: CIII emission at $z = 0.2$ for four different resolutions - the fiducial 1 kpc, 5 kpc, 13kpc, and 25 kpc proper corresponding to angular resolutions of 0.3", 1.5", 4" and 7.6" respectively. The medium resolutions reproduce many of the features of the highest resolution and would allow for a more confident detection of filamentary CGM emission features. At the lowest resolution, it is possible to detect an elongation of the emission and the distances would make it identifiable as CGM material but filaments are less conclusive.

4.4.4.2 Resolution Limitations

In addition to the surface brightness limits, the resolution of the image affects the types of conclusions that can be drawn from the observations. For all of the previous plots, the resolution of the projected grid has been set to 1 kpc physical such that the angular resolution varies with redshift. At this resolution, it is possible to see the filaments and streams feeding the galaxy. How does this change if the physical resolution is varied?

Figure 4.12 shows the CIII emission for the galaxy at $z = 0.2$, with four different resolutions: the fiducial 1 kpc, 5 kpc, and 25 kpc. This corresponds to angular resolutions of 0.3", 1.5", 4" and 7.6" respectively. At the moderate resolution of 13 kpc, it is still possible to discern the filamentary features extending from the disk. At the lowest resolution, however, the CGM emission resembles an extended halo around the galaxy. Because of its physical extent, one can still associate this emission with the CGM, but valuable information about the spatial distribution of the gas has been lost. The low resolution also makes it difficult to track the evolution of the CGM. At most, an elongation aligned with the disk could be seen developing, corresponding to the filaments feeding the disk, but internal clumpy structures

and features perpendicular to the disk are masked.

One optimistic consequence of these predictions derives from the fact that at higher redshift, the physical angular diameter of an object is almost unchanging due to cosmological expansion. Given the relatively constant physical extent of the emission, the resolution of any observation will not change much for galaxies between $z = 0.5$ and $z = 1$. In this range, the 25 kpc physical resolution corresponds to roughly 3"-4" and the 5 kpc resolution to 0.6"-0.8". Thus, by ensuring that the resolution is at least 4", it should be possible to confirm emission from the CGM for $0.5 < z < 1$ and begin to resolve its structure at lower redshifts. At $z = 0.2$, basic filamentary structure and stripped material should be distinguishable with this angular resolution (see the 13 kpc panel of Figure 4.12). Within the next year, the balloon-borne FIREBall-2 will launch with this resolution and is expected to make a positive detection. A small, UV emission line explorer is currently being designed to have a comparable resolution but also to cover a much larger range in wavelength, providing complementary coverage to FIREBall-2. Finally, further in the future, a 12 m class, UV/optical space telescope named the High-Definition Space Telescope (HDST) has been designed with the specification of 0.01" angular resolution between 100-500 nm. As shown in Figure 4.12, this unprecedented resolution would allow for an evaluation of the predominance of filamentary accretion for the first time, as well as structures created by galactic outflows.

4.5 Discussion

It is only recently that comparing the CGM of simulations to data has become possible and that emission-line predictions from the simulations are relevant for upcoming observations. We are entering a new realm of detailed CGM studies for which it is necessary to understand

The report describing this proposed telescope can be found at http://www.hdstvision.org/

the limitations of current simulations and to evaluate which conclusions we expect to remain robust.

In this paper, we have examined a single simulation of a Milky Way-like galaxy using one form of purely thermal supernova feedback in an `enzo` adaptive mesh refinement (AMR) simulation. Like Hummels et al. (2013) who uses a similar prescription, we find that the simulation has difficulty in producing the necessary column densities for all the ions but especially OVI. Hummels et al. (2013) found that implementing stronger feedback brought better agreement while we've found that lowering the assumed EUVB can be equally effective. On the contrary, the most common way to implement supernova feedback in SPH simulations is to give either a constant or physically scaled velocity kick to a series of wind particles that carry away the SN energy in kinetic form. One such simulation by Ford et al. (2015) found better agreement with the low-ions although they still fail to reproduce the OVI observations. This implies that the direct, thermal methods prevalent in AMR cause the gas to reach higher temperatures as opposed to the wind velocity approach of SPH simulations, which shock heat differently. Furthermore, the simple thermal feedback assumed in this simulation also leads to the well-known overcooling problem. The HI distribution of the galaxy is known to be too centrally concentrated at z=0 (Fernández et al. 2012) and too many stars are formed (Joung et al. 2012).

However, new methods are emerging that incorporate additional components of the SN feedback. For example, Liang et al. (2015) included prescriptions for supernova pressure and momentum in addition to a thermal heating model in a series of RAMSES AMR simulations. Their fiducial model was also not a good fit to low-z data and again, increasing the feedback and lowering the star formation efficiency led to greater agreement. Building on the wind velocity method, AREPO and Illustris in particular include an implementation of AGN feedback with quasar and radio modes. Suresh et al. (2015b) found that including the radio

mode in particular is responsible for enriching the CGM in the simulations and reproduces the bimodality of star-forming and passive galaxies seen in OVI data. However, they still see a stronger mass dependence on the OVI distribution than what is observed and the radio mode feedback in Illustris is known to be too extreme, removing too much gas from the center of massive galaxies (Suresh et al. 2015b; Genel et al. 2014). Oppenheimer et al. (2016) found that AGN feedback in their EAGLE SPH simulations does not have a large effect on the OVI column densities and that the lower values for passive galaxies are instead driven by their higher virial temperature. Additionally, the inclusion of non-equilibrium chemistry in their simulations also does not resolve the almost universal issue of producing too little OVI for star-forming galaxies and passive galaxies alike. Finally, Salem et al. (2015) found that implementing a two-fluid cosmic ray method resulted in a cosmic ray-driven wind that gradually accelerated the gas, allowing for a larger range of gas temperatures as well as a higher metallicity beyond 100 kpc. Both contribute to higher column densities for all of the ions considered in this paper. In particular, the simulation reproduced the OVI measurements of the COS Halos survey for star-forming galaxies.

In short, reproducing both the stellar properties and the CGM properties of a given galaxy at low redshift is a major theoretical challenge and an important test of modern simulation methods. The majority have difficulties in capturing the multiphase medium required to produce such high levels of low and high ions in the data. Likely, a combination of these advanced feedback prescriptions will be necessary to remedy this. Thus, low-z CGM absorption measurements are a powerful new way to constrain such prescriptions and further motivate the emission observations we are predicting in this work. Emission predictions can provide complementary constraints on these feedback processes. Understanding the role and effect of purely thermal supernova feedback in work such as this will allow us to estimate its importance in future work with more complex schemes.

In addition to the uncertainty in the feedback scheme, the resolution of the simulation potentially limits the conclusions that can be drawn from comparisons with the column density data. Werk et al. (2014) found low number densities for the cool clouds causing the absorption in the COS Halos data, corresponding to cloud sizes of 0.1-2000 pc, the larger of which can be resolved by current zoom-in simulations. However, Crighton et al. (2015) detected the presence of eight smaller (<100-500 pc), higher-density clouds in an QSO spectrum with a z=2.5 foreground galaxy. If these scales are the norm, simulations may not resolve these clouds which exist beyond the high-density disk and which potentially contain a large fraction of the cool CGM gas. These resolution concerns and the possible existence of dense clouds relate back to the feedback mechanisms required to accurately reproduce the multiphase medium. Dense clumps will have cool, self-shielding cores that could explain the observations of low ions while the shells around them and the diffuse volume-filling gas could be responsible for the intermediate to high ions. Instead, lower-resolution simulations may produce a mid-range, average temperature that does not precisely reflect the state of the gas. Further studies of the cooling of the gas in idealized simulations where the resolution can be much higher could tell us more about how cool gas forms and persists within the volume-filling hot phase of the galactic halo. In addition, if dense small clouds do exist, they should appear as bright points in emission studies as opposed to lower-density clouds since the emission scales as the square of the density, offering a chance to probe the number and density of the emitting clouds if the angular resolution is high enough.

Finally, this is ultimately a simulation of a single Milky Way-like galaxy. The conclusions drawn here about the filamentary structure of the gas especially at low redshift might be specific to this particular galaxy. More than just changing the viewing angle is necessary for understanding the dependence of our predictions on the physical properties of the gas. Our exact expectations could change if the galaxy forms fewer stars; if the filaments are

broader than expected here; if the environment of the galaxy increases the metallicity of the gas - to name a few examples. The cosmological study of emission sources by Frank et al. (2012) suggests that an appreciable number of sources will be detectable at the redshifts considered in this paper such that we can begin to measure how the emission varies with these physical parameters. Thus, it is only by conducting both future observational surveys and a larger range of cosmological simulations that we can begin to address the variance in emission signatures of the CGM.

Even with these limitations of the simulation, we expect the trends seen in our conclusions to be robust. Varying the EUVB can produce variations in the simulated column densities at low redshift and in future work this can be further explored in addition to alternative forms of feedback. Furthermore, there is seemingly a tension between the density and temperature of gas within simulations of this type and those modeled from the COS Halos measurements. The coexistence of large amounts of SiIV, CIII and OVI and our failure to reproduce all three simultaneously indicate that there is a *more* complex temperature structure than what's seen here. Because of this, details of the extent and shape of the emission may vary in future work but the dominance of the CIII, CIV, and OVI lines has remained thus far and should persist. Similarly, low ions tracing higher-density structures while high ions are more volume filling is a clear prediction of any warm/hot gaseous halo. In addition, altering feedback methods to capture a larger range of temperatures could lead to further structure in the emission at low redshift. Less clear is how numerous and how thin these features might become. In this way, the resolution of future observations could be the limiting factor in imaging the CGM structures, possibly even more so than surface brightness limits. However, the general conclusions of this paper regarding the required surface brightness limits and resolution limits should continue to reflect simulations of this type.

4.6 Summary and Conclusions

Observing the predicted gas halos of nearby galaxies has long been a goal of observations, but the need to study this gas in the space ultraviolet, coupled with the diffuse nature of the gas in question, has made this challenging. Now, studies of the CGM at low redshift are entering an unprecedented age of sensitivity. Measurements can begin to constrain theoretical prescriptions in simulations as well as discriminate between them. In this work, we vary the EUVB in a high-resolution cosmological simulation of a Milky Way-like galaxy and examine its role in determining how the simulated column densities compare to recent data. We then predict the emission signal expected from such gas for upcoming instrumentation, as well as how it varies with redshift and the physical properties of the gas itself.

Our main conclusions can be listed as follows:

1. Looking at column density maps at $z = 0.2$, the largest values for the column densities of all the ions studied here are found in high-density filamentary structures. The low ions (HI, CIII, SiIV) are found almost exclusively in these structures, while OVI is found throughout the halo as its higher ionization energy allows it to exist in the volume-filling hot gas.

2. Varying the quasar component of the standard EUVB can significantly change the predicted column densities of the simulation. In particular, lowering this component by a factor of 100 brings the simulation values into much better agreement with the low-ion data of the COS Halos sample. The simulated OVI column densities remain too low at all impact parameters compared to the observed values for star-forming galaxies, even with the strongest EUVB.

3. Comparing the gas temperature and density in the simulation to that found through

CLOUDY modeling of the COS Halos data shows that the simulation predicts higher temperatures than the data modeling. This demonstrates that it is possible to produce similar column densities from different gas distributions.

4. Examining the redshift evolution of the emission reveals that the emission becomes more structured at later times, tracing the remaining high-density, low-temperature features. This is in contrast to the majority of the gas that shifts to lower densities and higher temperatures from $z = 1$ to $z = 0$ due to the weakening of cold gas filaments and the progression of supernova-driven winds.

5. A surface brightness limit of 100 photons s^{-1} cm^{-2} sr^{-1} should enable a clear detection of emission from the CGM with, CIII emission extending as far as 100 kpc and OVI as far as 50 kpc at $z = 0.2$. The predicted extent stays roughly constant for $0.5 < z < 1.0$ as the cosmological surface brightness dimming is balanced by an increasing intrinsic emissivity.

6. An angular resolution of 4" is necessary to begin to resolve the spatial distribution of the CGM out to $z = 1$, and sub-arcsecond resolution is needed to resolve beyond a general elongation from the disk. At $z = 0.2$, these same observations require an angular resolution of 7.6" (for elongation) and 1.5" (for features) respectively.

These conclusions focus on results from the combination of predicted UV absorption and emission line data from a simulated Milky Way-like galaxy, offering a physical explanation for the trends seen in observations for the existence and extent of multiple ions. Other studies have focused on varying feedback prescriptions to bring simulations into better agreement with recent data. However, this can also be reversed as simulation predictions can be extended to create true mock observations that can enable better interpretations of future

data. To make more accurate predictions for observations, future work will have to include a number of details excluded here.

First, the low surface brightness of the emission in question means that the UV background can overpower the CGM signal. Including a model of the background signal and incorporating its subtraction will provide a better understanding of which CGM structures can be detected with confidence. Second, the continuum emission from the galaxy can also dominate the CGM emission-line signal close to the disk, especially at moderate to low resolution. The disk-halo interface is where the SN winds are being launched; understanding this transition is particularly important. Finally, the velocity structure of the gas has not been considered here, which can change the line profiles of the emission. Joung et al. (2012) examined the flow of gas into and out of the galaxy, finding that the majority of the accretion at low redshift was in the form of warm/hot gas. Associating emission with these flows is left for future work but will become crucial as integral field units that provide both spatial and spectral information are becoming commonplace. This kinematic information will provide the best observational evidence for both inflows and outflows of gas from galaxies.

Acknowledgments

We are grateful to M. Ryan Joung for generously sharing his simulation output and guidance. L.C. would also like to thank Yuan Li, Cameron Hummels, Munier Salem, and Bruno Milliard for helpful discussions. L.C. and D.S. acknowledge support from NASA grant NNX12AF29G. L.C. would also like to acknowledge support from the Chateaubriand Fellowship.

4.A Uncertainty in the Extragalactic Ultraviolet Background

The extragalactic ultraviolet background (EUVB) is an important component of any photoionization model implemented for both observations and simulations. However, the EUVB is historically not well constrained. Variations of the Haardt & Madau (1996) background (e.g. HM96, HM01, HM05, HM12) are implemented in the majority of hydrodynamical simulations and in CLOUDY. Yet simulations attempting to match measurement of the low-redshift Lyman α forest find that the most recent HM12 model does not reproduce the observed column density distribution of absorbers. The simulations of Kollmeier et al. (2014) require a photoionization rate a factor of five higher than the HM12 model, while those of Shull et al. (2015) suggest a factor of 2-3 increase. However, unlike the previous work, Shull et al. (2015) find that the HM12 model does in fact reproduce the distribution of absorbers with $\log(N_{\rm HI}) > 14.0$ and that no single model reproduces the entire distribution. Both of these values are more consistent with HM96 and in line with our high EUVB model, g1q10. Finally, at lower redshifts, constraints are even harder to place on the EUVB (Cooray 2016). In contrast to both of these high-redshift studies, Adams et al. (2011) placed upper limits on the photoionization rate at $z = 0$ from the non-detection of Hα in UGC 1281 at roughly the values in the HM12 model and in UGC 7321 at roughly 10 times lower - corresponding to 10 and 100 times lower than the HM05 model assumed throughout this paper. This is in the range of our low model, g1q01. In this way, the models used here bracket the range of possible photoionization rates as they are known today. These theoretical and observational inconsistencies highlight the uncertainty in the shape and intensity of the EUVB.

In addition, these models depend on the escape fraction of ionizing photons from their

host galaxy, a quantity that is expected to be low but has been argued to be anywhere from 0.01 to 0.3, depending on the galaxy mass and redshift (Dove et al. 2000; Wise & Cen 2009; Benson et al. 2013; Roy et al. 2015) (see introduction of Wise et al. 2014b, for an in-depth discussion). Both of the above Lyman α studies agree that the likely source of the discrepancy is the prescription for the escape fraction which leads to a galactic contribution to the EUVB that is too low at low redshift.

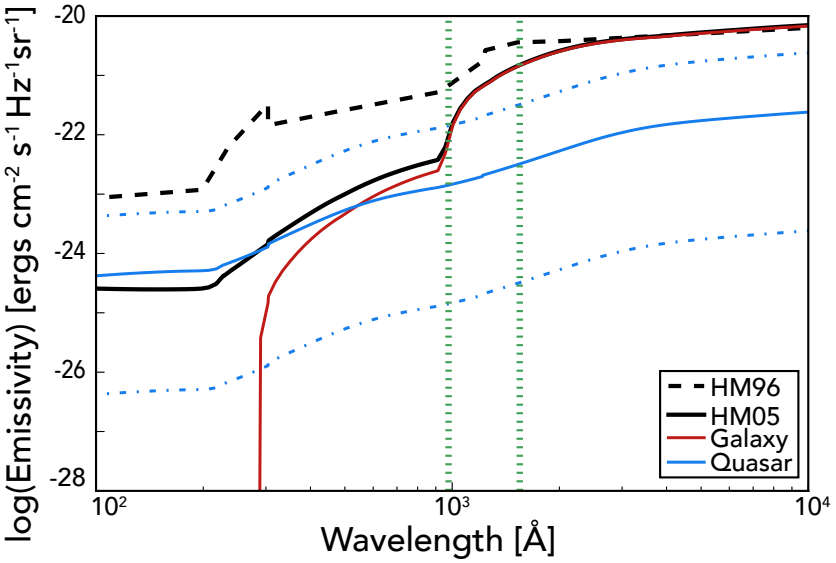

Figure 4.13: Relevant EUVB backgrounds for this work: HM96 (assumed in the simulation) and HM05 (fiducial for CLOUDY modeling). The galaxy (red) and quasar (blue) components of HM05 are also plotted. The blue dashed lines represent the two quasar backgrounds assumed throughout the paper (100 times less intense and 10 times more intense, respectively). The green vertical lines bracket the wavelengths of the emission examined in the paper.

Figure 4.13 shows the EUVB relevant for this work. HM96 is the background assumed within the simulation and used for the chemical network that determined the cooling rate at each time step. HM05 is the background assumed and varied for all of the CLOUDY modeling discussed in the paper. Figure 4.13 also shows how the HM05 background is broken into its components: the galactic (red) and the quasar (blue). Throughout the paper, this background is modified to either g1q01 (a quasar intensity 100 times smaller than fiducial)

or g1q10 (a quasar intensity 10 times larger than fiducial). These models are plotted as blue dot-dashed lines.

One concern is that the model assumed for the simulation (HM96) is not the same as the one assumed in the CLOUDY modeling done in this paper (HM05). At longer wavelengths, the HM96 and HM05 backgrounds are similar; however, the HM96 background is closer to the modified g1q10 background than to the fiducial HM05 at shorter wavelengths, where the quasar component dominates. This suggests that the range of backgrounds being explored is reasonable. Furthermore, the only way the simulation directly depends on the EUVB is in the calculation of the heating and cooling. The heating will be dominated by physical processes such as supernova feedback. As for the cooling, for $T > 10^4$K, which is the case for all CGM gas considered, CLOUDY modeling shows that the cooling function assumed in the simulation varies somewhat with the ionization fraction at the low metallicities found in the CGM but is dominated by the overall metallicity. Thus, pairing the simulated density and temperature with the varying EUVB in the CLOUDY modeling is not unreasonable.

The green vertical lines bracket the wavelength range of the emission lines considered here. They fall within the galaxy-dominated part of the spectrum. However, the quasar component contributes much more of the ionizing intensity and thus is more important in shaping the expected ion fractions for the column density and emission predictions. Werk et al. (2014) examine how differences between HM01 and HM12 affect their measurements and find that repeating the analysis with HM12 lowers the gas ionization parameters by 0.1-0.4 dex, which must be accounted for in either the HI column density or the metallicity. The simulated column densities show larger variations with changes in EUVB because the density and temperature are fixed and only the ionizing intensity is changing. In the less constrained CLOUDY modeling, flexibility within setting the interdependent quantities of ionization parameter and metallicity can reduce the effect of the EUVB. The value of the

simulation is that these gas properties are determined by the larger cosmological context instead of modeling an isolated cloud.

Finally, in addition to the uncertainty in the EUVB, ionizing photons from local stellar sources are expected to be the dominant source of photoionization in local star-forming regions within the disk, but again, the escape fraction of these photons into the halo is entirely uncertain. Similarly, star formation in the halo has been shown to change the extent and shape of a galaxy's Lyman α emission but this triggered emission results in a greater predicted UV flux than what is currently measured (Lake et al. 2015). Because of these uncertainties and because we are focused on emission from gas farther from the star-forming disk, including this ionization source is reserved for future work.

4.B Investigating the Effects of Resolution

Because the column density and surface brightness calculations depend so sensitively on the density, temperature, and metallicity of the gas, understanding how the resolution of the simulation affects these quantities is necessary to evaluate their robustness. On one hand, over-cooling can lead to large, artificially dense clumps and is known to leave a too centrally concentrated disk. On the other hand, observational evidence suggests that absorbing clouds can be small, high-density structures that would be under-resolved in the simulation (Crighton et al. 2015).

The ideal solution would be to re-run the simulation at lower resolution and compare its output to the simulation analyzed here. Unfortunately, because of the length of time that has passed between this analysis and the original, high-resolution run, the exact initial conditions of this simulation cannot be reproduced. However, we can attempt to address this issue by re-binning the high-resolution output to lower resolutions. Figure 4.14 shows

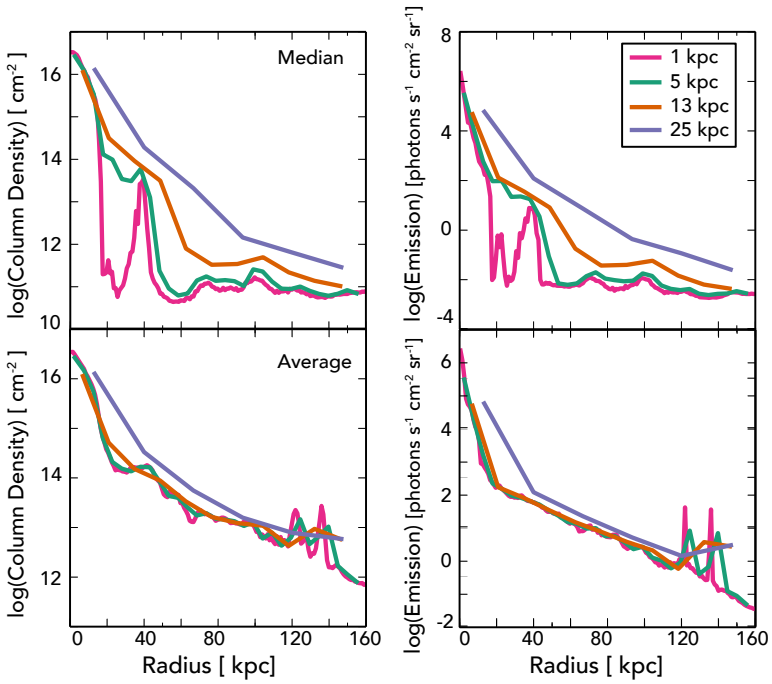

Figure 4.14: Median and average column density and emission profiles of CIII at $z = 0.2$, binned for four different resolutions. 1 kpc is the resolution assumed throughout the paper and is roughly the underlying simulation resolution beyond the disk in the CGM. As the resolution increases, the median profile decreases as the gas structure is refined. At the very center of the disk and in the outer halo, the median profile of the simulation appears to be converging below 5 kpc. The exception is the disk-halo interface at roughly 20 kpc. It is only at the highest resolution is the sharp transition from disk to halo captured. The average converges more quickly.

the median and average profiles of the column density and emission of CIII at $z = 0.2$ for the volume considered in the above analysis. The average profiles of these quantities have converged except at the lowest resolution. On the other hand, at lower resolutions, the median profiles of the column density and the emission are both too high, corresponding to higher average density and fewer low-density regions. However, by a resolution of 5 kpc, the simulation seems to have converged on a median profile for the inner disk as well as the outer parts of the halo. The remaining region, around 20 kpc, corresponds to the edge of the disk-halo interface. It's only at the highest resolution that this interface is properly

resolved. At 5 kpc, this boundary is still blurred, not allowing for the sharp transition from high-density, cold gas to low-density, warm gas.

These profiles suggest that further resolving the outer halo should not greatly change the median predictions for the column density and emission. While higher-density clumps are mostly likely still not being resolved even with the maximum resolution, Figure 4.14 suggests that these regions are small compared to the volume and will not significantly alter the median profiles of either quantity.

Chapter 5

Conclusion

The halos of Milky Way-like galaxies - both gaseous and stellar as well as the satellite galaxies they contain - provide new, unique opportunities to test fundamental processes in galaxy formation. Stellar abundances of stars in the dead (i.e. stellar halo) and surviving satellite dwarf galaxies of the Milky Way give us a direct look at how star formation proceeding in small halos in the early universe. At the other end of cosmic time, absorption and emission studies of the circumgalactic medium allow us to probe the physical conditions in the gaseous halo of Milky Way-like galaxies at low redshift. Moreover, cosmological simulations have now advanced to the point where meaningful constraints can be placed on the processes they are modeling with this new data. To this end, this thesis looked to take advantage of these advancements to place the current findings of simulations into an observational context. In this section, the key results of this thesis are summarized and future directions for this work are discussed.

5.1 Summary of Results

In Chapter 2, the early chemical environment of the progenitors of a Milky Way-like galaxy was investigated in order to better understand discrepancies in stellar abundances amongst stellar halo stars and those in the surviving Local Group dwarf galaxies. Combining a semi-analytic model for supernova-driven winds and a cosmological N-body simulation, we found that the progenitor halos of the surviving satellite dwarf galaxies of a Milky Way-like system sit on the outskirts of halos that eventually merge to form the main halo at $z = 0$. This suggests that the dwarf galaxy progenitors are naturally less cross-polluted by neighboring halos than their main halo progenitor counterparts. In particular, main halo progenitors were found to typically have as many as 10 SN bubble overlaps as opposed to dwarf progenitors which were much more likely to remain chemically isolated. Furthermore, those dwarf galaxies that did experience cross-pollution were likely to eventually merge with its cross-polluting neighbor, masking the effects in the $z = 0$ stellar abundances. This implies that cross-pollution may have a distinct effect on satellite galaxies that are eventually disrupted and accreted into the stellar halo, potentially helping to explain the measured differences in the abundances of stellar halo and dwarf galaxy stars.

In Chapter 3, we expand upon our study of the early chemical environment of small, star-forming halos with the goal of exploring the efficacy of analytic models and to place that simulation within the observation context of the ultrafaint dwarf galaxies. In particular, this work was motivated by recent observations of the UFDs that suggested both continuous, self-enriching star formation and bursty star formation with large spreads in metallicities. We find that the semi-analytic model used in Chapter 2 roughly agrees with the extent of metal enrichment from star-forming halos in the a state-of-the-art cosmological simulation. However, the commonly held assumption of homogeneous mixing does not reproduce the

large spreads in metallicities that are seen in short bursts of star formation in certain halos. Furthermore, the star formation histories of galaxies in the simulation do not prefer a single scenario derived from the data; they can be bursty, continuous or both. The metallicity distribution functions associated with these galaxies are too metal rich and too peaked when compared with the UFDs but spreads in metallicity are generated within as little as a few 100 Myrs. These properties do not appear to be tied to halo mass, chemical environment or mergers but instead to be a natural consequence of the hydrodynamics.

In Chapter 4, we move to a study of the gaseous halo of a Milky Way-like galaxy at low redshift in order to better understand the the sources of absorption line studies and to make predictions of the expected emission targeted by upcoming observational surveys. In general, low-ions (e.g. HI, CIII, SiIV) are found in high-density, low-temperature, filamentary structures while the high-ion OVI is found throughout the diffuse, higher-temperature halo. Yet the standard form of the simulation fails to reproduce the recent column density data of the COS-Halos team. However, lowering the EUVB, an uncertain yet crucial assumption of ionization modeling, does bring the simulation into better agreement with the low-ion data. Furthermore, it appears that the gas is uniformly too hot in the simulation when compared to physical properties derived from the data and that a more multiphase medium may be the key to better agreement between the simulation and observations. With this observational context in hand, we then made predictions for the evolution of the emission associated with this galaxy. Within the simulation, the emission becomes more structured at later times as the halo gas shifts to lower densities and higher temperatures by $z = 0$. Finally, we predict that this emission can possibly be detected out to 100 kpc with moderately low surface brightness limits and reasonable angular resolution in line with upcoming instrumentation and well within reach of any future space-based optical/UV telescope.

5.2 Future Work

5.2.1 Stellar Abundances and Early Star Formation

The simulation shows that complicated SFHs with spreads in metallicities can be generated on short enough timescales to explain observations of Local Group dwarf galaxies. However, the conclusions we can draw are limited by the nature of the simulation. Is the lack of agreement between the simulated and observed MDFs a product of the specific volume being studied, some more general issue with the underlying baryonic implementations (especially given similar discrepancies seen in Simpson et al. (2013)) or a combination of the two? A natural next step would be to examine multiple early environments to examine the effects of cosmic variance on our conclusions as well as to run the simulation to $z = 0$ to ensure that the comparisons we are making to the ultrafaint dwarf galaxies are exactly valid. However, the computational costs of these approaches are still currently prohibitive.

In the more immediate future, it is possible to begin to model the full chemical abundances produced by stars in the simulation instead of relying on a single metallicity field. Work has been done at low redshift (Oppenheimer et al. 2016) and at lower resolution (Zolotov et al. 2010) to incorporate the tracking of individual elements. In addition, the star formation histories and metallicities naturally generated in the simulation can be combined with 1D chemical evolution models. Such models can use the particle masses and creation times to correctly sample the IMF and generate the associated abundance ratios. Including this additional chemical component may provide a way of distinguishing the different SFH types seen identified in this work as well as providing further insight into the source of the discrepancies with the MDFs.

5.2.2 Circumgalactic Medium in Absorption and Emission

It is now almost ubiquitous that our current versions of galaxy simulations have an inability to reproduce the column density radial profiles of COS-Halos, a clear sign that feedback methods either need to be modified or expanded to include new processes. However, instead of immediately changing parameters or creating new feedback methods, a deeper investigation of the physics of the CGM may provide clues on how to proceed. In particular, the resolution of the CGM in most simulations may be larger than the individual components that shape the absorption spectra. To this end, small, idealized simulations with particularly high resolution may allow for a study of how the gas may be heated, mix, cool, and clump in a halo environment. Such boxes can then be connected to simulations that zoom in on a specific galaxy and then to the even larger environment of a full, cosmological sample of galaxies. This approach coupled with new tools for generating realistic mock spectra from simulations will allow for a more thorough comparison of the simulations to the data.

Similarly, emission predictions represent a complementary tool for studying the physical properties of the CGM. The techniques presented here can easily be extended to other simulations, such as those of Salem et al. (2015) whose good agreement with the COS-Halos data is an exception to the trend discussed above. In addition, the work in this thesis focused on metal-line emission but Lyman α is expected to be the brightest source of emission for all galaxies. Modeling the distribution of Lyman α, however, required the use of radiative transfer codes that are hard to apply to AMR simulations. However, future collaborations are focused on developing a model for such emission from the Milky Way galaxy discussed in this thesis. Finally, in the near future, FIREBall-2 will fly and the data provide an exciting opportunity to directly compare the predictions of this work to observations and lay the groundwork for future space-based optical/UV missions.

5.2.3 Remaining Open Questions

As indicated by the abundance of future work, a number of open questions remain following the conclusion of this thesis. In particular, we can ask the following questions:

- Is physics on the smallest scales (i.e. cooling and condensation, turbulent mixing, non-equilibrium ionization) and the need for higher resolution driving the simulations' inability to match the COS Halo data? And how can we connect these small scales back to the larger, cosmological simulations?

- How will the generation of realistic spectra from simulations affect how we interpret comparisons with absorption line data moving forward?

- How do the emission properties of Milky Way-like galaxies vary with different forms of feedback? How does Lyman α emission compare with the metal-line emission in these same situations once radiative transfer is accounted for?

- How will the emission predictions compare with future observations, the some of the most exciting being the upcoming FIREBall-2 data?

- Will generating stellar abundances for the dwarf galaxies in simulations reveal new clues as to how to better match the star formation histories and metallicity distribution functions of the simulated dwarf galaxies to those observed?

This list is not exhaustive but is an example of the exciting prospects that remain in the field. Answering these questions will help us take our next steps forward in our understanding of the formation and evolution of galaxies.

Bibliography

Adams, J. J., Uson, J. M., Hill, G. J., & MacQueen, P. J. 2011, ApJ, 728, 107

Agertz, O., Kravtsov, A. V., Leitner, S. N., & Gnedin, N. Y. 2013, ApJ, 770, 25

Agertz, O., Teyssier, R., & Moore, B. 2011, MNRAS, 410, 1391

Aguirre, A., Hernquist, L., Schaye, J., et al. 2001, ApJ, 561, 521

Andrews, B. H., Weinberg, D. H., Schönrich, R., & Johnson, J. A. 2016, ArXiv e-prints, arXiv:1604.08613

Arrigoni Battaia, F., Yang, Y., Hennawi, J. F., et al. 2015, ApJ, 804, 26

Avila-Vergara, N., Carigi, L., Hidalgo, S. L., & Durazo, R. 2016, MNRAS, 457, 4012

Barai, P., Viel, M., Borgani, S., et al. 2013, MNRAS, 430, 3213

Bell, E. F., Zucker, D. B., Belokurov, V., et al. 2008, ApJ, 680, 295

Belokurov, V., Zucker, D. B., Evans, N. W., et al. 2006, ApJ, 642, L137

Benson, A., Venkatesan, A., & Shull, J. M. 2013, ApJ, 770, 76

Benson, A. J., Frenk, C. S., Lacey, C. G., Baugh, C. M., & Cole, S. 2002, MNRAS, 333, 177

Bertone, S., Aguirre, A., & Schaye, J. 2013, MNRAS, 430, 3292

Bertone, S., & Schaye, J. 2012, MNRAS, 419, 780

Binney, J., & Merrifield, M. 1998, Galactic Astronomy

Bland-Hawthorn, J., Sutherland, R., & Webster, D. 2015, ApJ, 807, 154

Booth, C. M., Agertz, O., Kravtsov, A. V., & Gnedin, N. Y. 2013, ApJ, 777, L16

Booth, C. M., & Schaye, J. 2009, MNRAS, 398, 53

Bordoloi, R., Tumlinson, J., Werk, J. K., et al. 2014, ApJ, 796, 136

Borthakur, S., Heckman, T., Tumlinson, J., et al. 2015, ApJ, 813, 46

Bovill, M. S., & Ricotti, M. 2009, ApJ, 693, 1859

Bowen, D. V., Pettini, M., & Blades, J. C. 2002, ApJ, 580, 169

Boylan-Kolchin, M., Weisz, D. R., Bullock, J. S., & Cooper, M. C. 2016, ArXiv e-prints, arXiv:1603.02679

Bridge, C. R., Blain, A., Borys, C. J. K., et al. 2013, ApJ, 769, 91

Brook, C. B., Governato, F., Roškar, R., et al. 2011, MNRAS, 415, 1051

Brooks, A. M., Governato, F., Quinn, T., Brook, C. B., & Wadsley, J. 2009, ApJ, 694, 396

Brown, T. M., Tumlinson, J., Geha, M., et al. 2012, ApJ, 753, L21

—. 2014, ApJ, 796, 91

Brüns, C., Kerp, J., Staveley-Smith, L., et al. 2005, A&A, 432, 45

Bryan, G. L., Norman, M. L., O'Shea, B. W., et al. 2014, ApJS, 211, 19

Bullock, J. S., & Johnston, K. V. 2005, ApJ, 635, 931

Bullock, J. S., Kravtsov, A. V., & Weinberg, D. H. 2000, ApJ, 539, 517

Busha, M. T., Alvarez, M. A., Wechsler, R. H., Abel, T., & Strigari, L. E. 2010a, ApJ, 710, 408

—. 2010b, ApJ, 710, 408

Cen, R., Nagamine, K., & Ostriker, J. P. 2005, ApJ, 635, 86

Ceverino, D., Klypin, A., Klimek, E. S., et al. 2014, MNRAS, 442, 1545

Chabrier, G. 2003, PASP, 115, 763

Chau, A., Mayer, L., & Governato, F. 2016, ArXiv e-prints, arXiv:1605.01063

Chen, H.-W., Helsby, J. E., Gauthier, J.-R., et al. 2010, ApJ, 714, 1521

Choi, J.-H., & Nagamine, K. 2009, MNRAS, 393, 1595

Clark, P. C., Glover, S. C. O., Bonnell, I. A., & Klessen, R. S. 2009, ArXiv e-prints, arXiv:0904.3302

Cooray, A. 2016, ArXiv e-prints, arXiv:1602.03512

Corlies, L., Johnston, K. V., Tumlinson, J., & Bryan, G. 2013, ApJ, 773, 105

Crain, R. A., McCarthy, I. G., Frenk, C. S., Theuns, T., & Schaye, J. 2010, MNRAS, 407, 1403

Crighton, N. H. M., Hennawi, J. F., Simcoe, R. A., et al. 2015, MNRAS, 446, 18

Crosby, B. D., O'Shea, B. W., Beers, T. C., & Tumlinson, J. 2016, ApJ, 820, 71

Davé, R., Katz, N., Oppenheimer, B. D., Kollmeier, J. A., & Weinberg, D. H. 2013, MNRAS, 434, 2645

Davé, R., Oppenheimer, B. D., & Finlator, K. 2011, MNRAS, 415, 11

de Jong, J. T. A., Rix, H.-W., Martin, N. F., et al. 2008, AJ, 135, 1361

Dekel, A., & Silk, J. 1986, ApJ, 303, 39

Diemand, J., Kuhlen, M., & Madau, P. 2006, ApJ, 649, 1

Diemand, J., Madau, P., & Moore, B. 2005a, MNRAS, 364, 367

—. 2005b, MNRAS, 364, 367

Dijkstra, M., & Kramer, R. 2012, MNRAS, 424, 1672

Dove, J. B., Shull, J. M., & Ferrara, A. 2000, ApJ, 531, 846

Drlica-Wagner, A., Bechtol, K., Rykoff, E. S., et al. 2015, ApJ, 813, 109

Eggen, O. J., Lynden-Bell, D., & Sandage, A. R. 1962, ApJ, 136, 748

Fang, T., Mckee, C. F., Canizares, C. R., & Wolfire, M. 2006, ApJ, 644, 174

Ferland, G. J., Korista, K. T., Verner, D. A., et al. 1998, PASP, 110, 761

Fernández, X., Joung, M. R., & Putman, M. E. 2012, ApJ, 749, 181

Font, A. S., Johnston, K. V., Bullock, J. S., & Robertson, B. E. 2006a, ApJ, 638, 585

—. 2006b, ApJ, 638, 585

Ford, A. B., Oppenheimer, B. D., Davé, R., et al. 2013, MNRAS, 432, 89

Ford, A. B., Werk, J. K., Dave, R., et al. 2015, ArXiv e-prints, arXiv:1503.02084

Frank, S., Rasera, Y., Vibert, D., et al. 2012, MNRAS, 420, 1731

Frebel, A. 2010, Astronomische Nachrichten, 331, 474

Frebel, A., & Bromm, V. 2012, ApJ, 759, 115

Frebel, A., & Norris, J. E. 2015, ARA&A, 53, 631

Frebel, A., Simon, J. D., Geha, M., & Willman, B. 2010, ApJ, 708, 560

Fukugita, M., & Peebles, P. J. E. 2006, ApJ, 639, 590

Fumagalli, M., Prochaska, J. X., Kasen, D., et al. 2011, MNRAS, 418, 1796

Furlanetto, S. R., & Loeb, A. 2003, ApJ, 588, 18

Furlanetto, S. R., Schaye, J., Springel, V., & Hernquist, L. 2004, ApJ, 606, 221

Gawiser, E., Francke, H., Lai, K., et al. 2007, ApJ, 671, 278

Geha, M., Blanton, M. R., Yan, R., & Tinker, J. L. 2012, ApJ, 757, 85

Genel, S., Vogelsberger, M., Springel, V., et al. 2014, MNRAS, 445, 175

Gómez, F. A., Coleman-Smith, C. E., O'Shea, B. W., Tumlinson, J., & Wolpert, R. L. 2012, ApJ, 760, 112

Górski, K. M., Hivon, E., Banday, A. J., et al. 2005, ApJ, 622, 759

Governato, F., Willman, B., Mayer, L., et al. 2007, MNRAS, 374, 1479

Grcevich, J., & Putman, M. E. 2009, ApJ, 696, 385

Greif, T. H., Johnson, J. L., Bromm, V., & Klessen, R. S. 2007, ApJ, 670, 1

Guo, Q., White, S., Li, C., & Boylan-Kolchin, M. 2010, MNRAS, 404, 1111

Haardt, F., & Madau, P. 1996, ApJ, 461, 20

Haardt, F., & Madau, P. 2001, in Clusters of Galaxies and the High Redshift Universe Observed in X-rays, ed. D. M. Neumann & J. T. V. Tran, 64

—. 2012, ApJ, 746, 125

Hamden, E. T., Greer, F., Schiminovich, D., Nikzad, S., & Martin, D. C. 2012, in Society of Photo-Optical Instrumentation Engineers (SPIE) Conference Series, Vol. 8453, Society of Photo-Optical Instrumentation Engineers (SPIE) Conference Series, 9

Heger, A., & Woosley, S. E. 2002, ApJ, 567, 532

Helmi, A. 2008, A&A Rev., 15, 145

Hirschmann, M., Naab, T., Davé, R., et al. 2013, MNRAS, 436, 2929

Hopkins, P. F., Kereš, D., Oñorbe, J., et al. 2014, MNRAS, 445, 581

Hopkins, P. F., Quataert, E., & Murray, N. 2012, MNRAS, 421, 3522

Hummels, C. B., & Bryan, G. L. 2012, ApJ, 749, 140

Hummels, C. B., Bryan, G. L., Smith, B. D., & Turk, M. J. 2013, MNRAS, 430, 1548

Ibata, R. A., Gilmore, G., & Irwin, M. J. 1994, Nature, 370, 194

Joung, M. R., Putman, M. E., Bryan, G. L., Fernández, X., & Peek, J. E. G. 2012, ApJ, 759, 137

Karlsson, T. 2005, A&A, 439, 93

Kereš, D., Katz, N., Fardal, M., Davé, R., & Weinberg, D. H. 2009, MNRAS, 395, 160

Kereš, D., Katz, N., Weinberg, D. H., & Davé, R. 2005, MNRAS, 363, 2

Kirby, E. N., Cohen, J. G., Guhathakurta, P., et al. 2013, ApJ, 779, 102

Kirby, E. N., Cohen, J. G., Smith, G. H., et al. 2011a, ApJ, 727, 79

—. 2011b, ApJ, 727, 79

Kirby, E. N., Martin, C. L., & Finlator, K. 2011c, ApJ, 742, L25

Kirby, E. N., Simon, J. D., Geha, M., Guhathakurta, P., & Frebel, A. 2008, ApJ, 685, L43

Kollmeier, J. A., Weinberg, D. H., Oppenheimer, B. D., et al. 2014, ApJ, 789, L32

Koposov, S., Belokurov, V., Evans, N. W., et al. 2008, ApJ, 686, 279

Kroupa, P. 2001, MNRAS, 322, 231

Lake, E., Zheng, Z., Cen, R., et al. 2015, ApJ, 806, 46

Lanfranchi, G. A., Matteucci, F., & Cescutti, G. 2008, A&A, 481, 635

Leaman, R. 2012, AJ, 144, 183

Lee, D. M., Johnston, K. V., Tumlinson, J., Sen, B., & Simon, J. D. 2013, ApJ, 774, 103

Liang, C. J., Kravtsov, A. V., & Agertz, O. 2015, ArXiv e-prints, arXiv:1507.07002

Lunnan, R., Vogelsberger, M., Frebel, A., et al. 2012, ApJ, 746, 109

Majewski, S. R., Munn, J. A., & Hawley, S. L. 1996, ApJ, 459, L73

Majewski, S. R., Skrutskie, M. F., Weinberg, M. D., & Ostheimer, J. C. 2003, ApJ, 599, 1082

Marasco, A., Debattista, V. P., Fraternali, F., et al. 2015, MNRAS, 451, 4223

Martin, D. C., Chang, D., Matuszewski, M., et al. 2014, ApJ, 786, 106

Martin, N. F., de Jong, J. T. A., & Rix, H.-W. 2008, ApJ, 684, 1075

Matsuda, Y., Yamada, T., Hayashino, T., et al. 2011, MNRAS, 410, L13

McConnachie, A. W. 2012, AJ, 144, 4

McConnachie, A. W., Irwin, M. J., Ibata, R. A., et al. 2009, Nature, 461, 66

McWilliam, A. 1997, ARA&A, 35, 503

Milliard, B., Martin, D. C., Schiminovich, D., et al. 2010, in Society of Photo-Optical Instrumentation Engineers (SPIE) Conference Series, Vol. 7732, Society of Photo-Optical Instrumentation Engineers (SPIE) Conference Series, 5

Nelson, D., Genel, S., Pillepich, A., et al. 2015a, ArXiv e-prints, arXiv:1503.02665

Nelson, D., Genel, S., Vogelsberger, M., et al. 2015b, MNRAS, 448, 59

Nelson, D., Vogelsberger, M., Genel, S., et al. 2013, MNRAS, 429, 3353

Nidever, D. L., Majewski, S. R., Butler Burton, W., & Nigra, L. 2010, ApJ, 723, 1618

Nomoto, K., Tominaga, N., Umeda, H., Kobayashi, C., & Maeda, K. 2006, Nuclear Physics A, 777, 424

Ocvirk, P., & Aubert, D. 2011, MNRAS, 417, L93

Oey, M. S. 2003, MNRAS, 339, 849

Okrochkov, M., & Tumlinson, J. 2010, ApJ, 716, L41

Oppenheimer, B. D., & Davé, R. 2008, MNRAS, 387, 577

Oppenheimer, B. D., & Schaye, J. 2013, MNRAS, 434, 1043

Oppenheimer, B. D., Crain, R. A., Schaye, J., et al. 2016, MNRAS, arXiv:1603.05984

Pearson, S., Besla, G., Putman, M. E., et al. 2016, MNRAS, 459, 1827

Piontek, F., & Steinmetz, M. 2011, MNRAS, 410, 2625

Press, W. H., & Schechter, P. 1974, ApJ, 193, 437

Prochaska, J. X., Weiner, B., Chen, H.-W., Mulchaey, J., & Cooksey, K. 2011, ApJ, 740, 91

Putman, M. E., Peek, J. E. G., & Joung, M. R. 2012, ARA&A, 50, 491

Putman, M. E., Gibson, B. K., Staveley-Smith, L., et al. 1998, Nature, 394, 752

Putman, M. E., de Heij, V., Staveley-Smith, L., et al. 2002, AJ, 123, 873

Ritter, J. S., Sluder, A., Safranek-Shrader, C., Milosavljević, M., & Bromm, V. 2015, MNRAS, 451, 1190

Robertson, B., Bullock, J. S., Font, A. S., Johnston, K. V., & Hernquist, L. 2005a, ApJ, 632, 872

—. 2005b, ApJ, 632, 872

Roederer, I. U., Cowan, J. J., Karakas, A. I., et al. 2010, ApJ, 724, 975

Romano, D., & Starkenburg, E. 2013, MNRAS, 434, 471

Roy, A., Nath, B. B., & Sharma, P. 2015, MNRAS, 451, 1939

Salem, M., & Bryan, G. L. 2014, MNRAS, 437, 3312

Salem, M., Bryan, G. L., & Corlies, L. 2015, ArXiv e-prints, arXiv:1511.05144

Salem, M., Bryan, G. L., & Hummels, C. 2014, ApJ, 797, L18

Salvadori, S., & Ferrara, A. 2009, MNRAS, 395, L6

Salvadori, S., Tolstoy, E., Ferrara, A., & Zaroubi, S. 2014, MNRAS, 437, L26

Sancisi, R., Fraternali, F., Oosterloo, T., & van der Hulst, T. 2008, A&A Rev., 15, 189

Saul, D. R., Peek, J. E. G., Grcevich, J., et al. 2012, ApJ, 758, 44

Sawala, T., Scannapieco, C., Maio, U., & White, S. 2010, MNRAS, 402, 1599

Scannapieco, C., Tissera, P. B., White, S. D. M., & Springel, V. 2005, MNRAS, 364, 552

—. 2006, MNRAS, 371, 1125

Scannapieco, E., Ferrara, A., & Madau, P. 2002, ApJ, 574, 590

Scannapieco, E., Schneider, R., & Ferrara, A. 2003, ApJ, 589, 35

Schaerer, D. 2002, A&A, 382, 28

Schaye, J., Dalla Vecchia, C., Booth, C. M., et al. 2010, MNRAS, 402, 1536

Schaye, J., Crain, R. A., Bower, R. G., et al. 2015, MNRAS, 446, 521

Searle, L., & Zinn, R. 1978, ApJ, 225, 357

Sheffield, A. A., Majewski, S. R., Johnston, K. V., et al. 2012, ApJ, 761, 161

Shull, J. M., Moloney, J., Danforth, C. W., & Tilton, E. M. 2015, ApJ, 811, 3

Sijacki, D., Springel, V., Di Matteo, T., & Hernquist, L. 2007, MNRAS, 380, 877

Simcoe, R. A., Sargent, W. L. W., & Rauch, M. 2004, ApJ, 606, 92

Simpson, C. M., Bryan, G. L., Hummels, C., & Ostriker, J. P. 2015, ApJ, 809, 69

Simpson, C. M., Bryan, G. L., Johnston, K. V., et al. 2013, MNRAS, 432, 1989

Smith, B., Sigurdsson, S., & Abel, T. 2008, MNRAS, 385, 1443

Smith, B. D., Hallman, E. J., Shull, J. M., & O'Shea, B. W. 2011, ApJ, 731, 6

Smith, B. D., Wise, J. H., O'Shea, B. W., Norman, M. L., & Khochfar, S. 2015, MNRAS, 452, 2822

Springel, V. 2005, MNRAS, 364, 1105

Sravan, N., Faucher-Giguere, C.-A., van de Voort, F., et al. 2015, ArXiv e-prints, arXiv:1510.06410

Steidel, C. C., Adelberger, K. L., Shapley, A. E., et al. 2000, ApJ, 532, 170

Steidel, C. C., Bogosavljević, M., Shapley, A. E., et al. 2011, ApJ, 736, 160

Steidel, C. C., Erb, D. K., Shapley, A. E., et al. 2010, ApJ, 717, 289

Stewart, K. R., Kaufmann, T., Bullock, J. S., et al. 2011, ApJ, 735, L1

Suresh, J., Bird, S., Vogelsberger, M., et al. 2015a, MNRAS, 448, 895

Suresh, J., Rubin, K. H. R., Kannan, R., et al. 2015b, ArXiv e-prints, arXiv:1511.00687

Swinbank, A. M., Vernet, J. D. R., Smail, I., et al. 2015, MNRAS, 449, 1298

Tegmark, M., Silk, J., & Evrard, A. 1993a, ApJ, 417, 54

—. 1993b, ApJ, 417, 54

Thom, C., & Chen, H.-W. 2008, ApJ, 683, 22

Tolstoy, E., Hill, V., & Tosi, M. 2009, ARA&A, 47, 371

Trujillo-Gomez, S., Klypin, A., Colín, P., et al. 2015, MNRAS, 446, 1140

Tumlinson, J. 2010a, ApJ, 708, 1398

—. 2010b, ApJ, 708, 1398

Tumlinson, J., Thom, C., Werk, J. K., et al. 2011, Science, 334, 948

—. 2013a, ApJ, 777, 59

—. 2013b, ApJ, 777, 59

Turk, M. J., Smith, B. D., Oishi, J. S., et al. 2011, ApJS, 192, 9

Turner, M. L., Schaye, J., Steidel, C. C., Rudie, G. C., & Strom, A. L. 2015, MNRAS, 450, 2067

Tyler, K., Quillen, A. C., LaPage, A., & Rieke, G. H. 2004, ApJ, 610, 213

van de Voort, F., & Schaye, J. 2013, MNRAS, 430, 2688

VandenBerg, D. A., Stetson, P. B., & Brown, T. M. 2015, ApJ, 805, 103

Vargas, L. C., Geha, M., Kirby, E. N., & Simon, J. D. 2013, ApJ, 767, 134

Venn, K. A., Irwin, M., Shetrone, M. D., et al. 2004, AJ, 128, 1177

Wadsley, J. W., Stadel, J., & Quinn, T. 2004, New A, 9, 137

Wakker, B. P., Kalberla, P. M. W., van Woerden, H., de Boer, K. S., & Putman, M. E. 2001, ApJS, 136, 537

Webster, D., Bland-Hawthorn, J., & Sutherland, R. 2015, ApJ, 799, L21

Webster, D., Frebel, A., & Bland-Hawthorn, J. 2016, ApJ, 818, 80

Wechsler, R. H., Bullock, J. S., Primack, J. R., Kravtsov, A. V., & Dekel, A. 2002, ApJ, 568, 52

Werk, J. K., Prochaska, J. X., Thom, C., et al. 2013, ApJS, 204, 17

Werk, J. K., Prochaska, J. X., Tumlinson, J., et al. 2014, ApJ, 792, 8

Westmeier, T., Braun, R., & Thilker, D. 2005, A&A, 436, 101

White, S. D. M., & Rees, M. J. 1978, MNRAS, 183, 341

Wiersma, R. P. C., Schaye, J., Dalla Vecchia, C., et al. 2010, MNRAS, 409, 132

Wise, J. H., & Abel, T. 2011, MNRAS, 414, 3458

Wise, J. H., Abel, T., Turk, M. J., Norman, M. L., & Smith, B. D. 2012a, MNRAS, 427, 311

Wise, J. H., & Cen, R. 2009, ApJ, 693, 984

Wise, J. H., Demchenko, V. G., Halicek, M. T., et al. 2014a, MNRAS, 442, 2560

—. 2014b, MNRAS, 442, 2560

Wise, J. H., Turk, M. J., Norman, M. L., & Abel, T. 2010, ArXiv e-prints, arXiv:1011.2632

—. 2012b, ApJ, 745, 50

Woosley, S. E., & Weaver, T. A. 1995, ApJS, 101, 181

Zheng, Z., Cen, R., Weinberg, D., Trac, H., & Miralda-Escudé, J. 2011, ApJ, 739, 62

Zolotov, A., Willman, B., Brooks, A. M., et al. 2010, ApJ, 721, 738